HIGH-PERFORMANCE INORGANIC-ORGANIC HYBRID PEROVSKITE SOLAR CELLS

YOU PENG

PhD

The Hong Kong Polytechnic University

2018

The Hong Kong Polytechnic University
Department of Applied Physics

High-Performance Inorganic-Organic Hybrid Perovskite Solar Cells

YOU Peng

A thesis submitted in partial fulfillment of the requirements for the degree of Doctor of Philosophy

August 2017

CERTIFICATE OF ORIGINALITY

I hereby declare that this thesis is my own work and that, to the best of my knowledge and belief, it reproduces no material previously published or written, nor material that has been accepted for the award of any other degree or diploma, except where due acknowledgement has been made in the text.

_____(Signed)

YOU Peng (Name of student)

Abstract

Inorganic-organic hybrid perovskite solar cells (PSCs) have experienced a rapid development in the past few years and turned over a new leaf in solar cell research due to their high power conversion efficiency (PCEs), easy fabrication and low cost. Since the first report of the material used in solar cells in 2009, the power conversion efficiency of PSCs has now reached 22.7%, approaching the efficiencies of single crystalline silicon solar cells. The semiconducting inorganic-organic hybrid perovskites have shown great potential for photovoltaic applications because of their excellent optoelectronic and charge transport properties.

In this thesis, the applications of CVD graphene as transparent electrodes in PSCs were firstly introduced. Semitransparent solar cells that can absorb light from both sides are promising for some special applications, such as building-integrated photovoltaics and tandem solar cells. However, the performance of semitransparent PSCs has been limited by the quality of transparent top electrodes. Semitransparent PSCs were fabricated by laminating stacked CVD graphene as top transparent electrodes on perovskite layers for the first time. The device performance was optimized by improving the conductivity of the graphene electrodes and the contact between the top graphene electrodes and the hole transport layer (HTL) on the perovskite films. The devices with double-layer graphene electrodes show the maximum PCEs of 12.02±0.32% and 11.65±0.35% from FTO and graphene side, respectively, which are relatively high compared with the reported semitransparent PSCs. This work indicates that CVD graphene is an ideal candidate for transparent electrodes of PSCs. Considering its excellent mechanical flexibility and convenient preparation, graphene electrodes are expected to be used in flexible PSCs by printing

or roll to roll process, which may find applications to complement the rigid inorganic solar cells currently dominated in the market. Therefore, graphene is an ideal transparent-electrode material that can be used in various types of solar cells.

Secondly, the utilization of ultrathin black phosphorus (BP) flakes as an effective interfacial layer between perovskite and HTL was studied. The interface between perovskite and HTL is crucial to the photovoltaic performance of PSCs. In this thesis, few-layer BP flakes were introduced as buffer layer at the perovskite/HTL interface. Most of the BP nanoflakes were found to be distributed at the perovskite grain boundary regions, demonstrating efficient charge transport and defect passivation effect. This structure offers better band alignment, improves the hole transport property and reduces the recombination loss at the interface, thus the PCEs were greatly enhanced by over 10%. This enables more reproducible device performances reaching a stabilized power output of ~19%. Besides, the device stability was also significantly improved due to the passivation effect of the BP flakes. This study opens up the avenue in using solution exfoliated thin BP flakes for interfacial engineering of photovoltaic devices.

Besides, we have also introduced the utilization of laser annealing as an alternative approach to the traditional thermal annealing process for the crystallization of perovskite films. A continuous-wave laser diode with controllable output power was attached on an X-Y moving system, and the downward laser beam can scan through the perovskite surface line by line under the control of the computer program. Interestingly, it was found that the laser scanning parameters, including the laser power, laser wavelengths and scanning speeds, were closely related with the crystallization and morphology of the perovskite films. After systematical optimization, high-quality perovskite films with better crystallinity, larger grain size and lower density of defects were successfully fabricated. As a result, a high open

circuit voltage of 1.15 V and a champion efficiency of 20.08% with small hysteresis was obtained with a 450-nm laser operating with an output power of 150 mW and scanning speed of 25 mm/min. The stability of devices fabricated with this laser-annealing approach was also greatly improved due to the improved crystallinity and morphology of the perovskite films. This preliminary work paves a way to prepare high-quality perovskite films with controllable morphology.

List of Publications

1. **P. You**, Z.K. Liu, Q.D. Tai, S.H. Liu, F. Yan, Efficient Semitransparent Perovskite Solar Cells with Graphene Electrodes, *Advanced Materials*, 27 (2015) 3632-3638.
2. Q.D. Tai, **P. You**, H.Q. Sang, Z.K. Liu, C.L. Hu, H.L.W. Chan, F. Yan, Efficient and Stable Perovskite Solar Cells Prepared in Ambient Air Irrespective of the Humidity, *Nature Communications*, 7 (2016) 11105.
3. Z.K. Liu, **P. You**, C. Xie, G.Q. Tang, F. Yan, Ultrathin and Flexible Perovskite Solar Cells with Graphene Transparent Electrodes, *Nano Energy*, 28 (2016) 151-157.
4. C. Xie, **P. You**, Z.K. Liu, L. Li, F. Yan, Ultrasensitive Broadband Phototransistors Based on Perovskite/Organic-Semiconductor Vertical Heterojunctions, *Light: Science & Applications*, 6 (2017) e17023.
5. S.H. Liu, **P. You**, J.H. Li, J. Li, C.S. Lee, B.S. Ong, C. Surya, F. Yan, Enhanced Efficiency of Polymer Solar Cells by Adding a High-Mobility Conjugated Polymer, *Energy & Environmental Science*, 8 (2015) 1463-1470.
6. Z.K. Liu, **P. You**, S.H. Liu, F. Yan, Neutral-Color Semitransparent Organic Solar Cells with All-Graphene Electrodes, *Acs Nano*, 9 (2015) 12026-12034.
7. S.H. Liu, R.B. Jiang, **P. You**, X.Z. Zhu, J.F. Wang, F. Yan, Au/Ag Core-Shell Nanocuboids for High-Efficiency Organic Solar Cells with Broadband Plasmonic Enhancement, *Energy & Environmental Science*, 9 (2016) 898-905.
8. S.H. Liu, S.H. Lin, **P. You**, C. Surya, S.P. Lau, F. Yan, Black Phosphorus Quantum Dots for Boosting Light Harvesting in Organic Photovoltaics, *Angewandte Chemie International Edition*, 56 (2017) 13717-13721.
9. S.Q. Luo, **P. You**, G.D. Cai, H. Zhou, F. Yan, W.A. Daoud, The Influence of

Chloride on Interdiffusion Method for Perovskite Solar Cells, *Materials Letters*, 169 (2016) 236-240.

10. M. Zhang, C.Z. Liao, C.H. Mak, **P. You**, C.L. Mak, F. Yan, Highly Sensitive Glucose Sensors Based on Enzyme-Modified Whole-Graphene Solution-Gated Transistors, *Scientific Reports*, 5 (2015) 8311.
11. D.C. Yang, C. Xie, J.H. Sun, H. Zhu, X.H. Xu, **P. You**, S.P. Lau, F. Yan, S.F. Yu, Amplified Spontaneous Emission from Organic-Inorganic Hybrid Lead Iodide Perovskite Single Crystals under Direct Multiphoton Excitation, *Advanced Optical Materials*, 4 (2016) 1053-1059.
12. W. Tang, J.Q. Zhao, Y.K. Huang, L. Ding, Q.F. Li, J.H. Li, **P. You**, F. Yan, X.J. Guo, Bias Stress Stability Improvement in Solution-Processed Low-Voltage Organic Field-Effect Transistors Using Relaxor Ferroelectric Polymer Gate Dielectric, *IEEE Electron Device Letters*, 38 (2017) 748-751.
13. D. Yang, C. Xie, X. Xu, **P. You**, F. Yan, S. F. Yu, Lasing Characteristics of $CH_3NH_3PbCl_3$ Single-Crystal Microcavities under Multiphoton Excitation, *Advanced Optical Materials*, (2017) 170092.
14. G.Q. Tang, **P. You**, Q.D. Tai, R.S. Wu, Feng Yan, Performance Enhancement of Perovskite Solar Cells Induced by Lead Acetate as an Additive, *Solar RRL* (2018) doi.org/10.1002/solr.201800066.
15. K.C. Tang, **P. You**, F. Yan, Highly Stable All-Inorganic Perovskite Solar Cells Processed at a Low Temperature, *Solar RRL* (2018) doi.org/10.1002/solr.201800075.

Acknowledgements

I would like to express my gratitude to many people for their support during my PhD study period in The Hong Kong Polytechnic University.

First, I would like to thank my supervisor, Prof. Yan Feng. He gave me the opportunity to study at PolyU and has always provided guidance and supported on my research in every aspect, and taught me the methods to conduct research, write the paper and collaborate with other members. He is always giving me valuable suggestions and encouragements when I face difficulties in my research. He has always patiently revised my papers, reports and shared his thoughts with me. I will always be grateful for the advice, discussion and knowledge he shared with me during my study period.

I feel grateful to the colleagues who supported me in my PhD study. I would like to thank Dr. Liu Zhike, Dr. Tai Qidong, Dr. Li Jinhua, Dr. Liu Shenghua, Dr. Li Guijun, for their guidance and support. I would like to appreciate my group mates: Dr. Lin Peng, Dr. Sun Zhenhua, Mr. Tang Guanqi, Mr. Wang Naixiang, Mr. Li Yuanzhe, Mr. Liao Caizhi, Dr. Zhang Meng, Dr. Xie Chao, Dr. Wang Meng, Dr. Wu Runsheng, Dr. Zou Xuming, Dr. Fu Ying, Mr. Yang Anneng, Mr. Cao Jiupeng, Adam, Leo, Sam, Dr. Tang Wei, Dr. Fan Xi, Dr. Li Fan, Mr. Xiong Can, Ms. Chen Lizhen, Dr. Lin Haifeng and Ms. Wang Tianyue, for their great discussion, advice and assistance in my experiments.

Additionally, my sincere gratitude is given to my friends in Hong Kong, Dr. Ren Zhiwei, Dr. Shen Qian, Dr. Luo Shiqiang, Dr. Chen Li, Dr. Bai Gongxun, Dr. Xu Xiaomin, Dr. Huang Chun, Dr. Lin Shenghuang, Dr. Lu Wei, Dr. Long Hui, Dr. Chen Qingming, Ms. Yang Chenxiao, Dr. Li Tenghao, Dr. Zhang Yongliang, Dr. Zhao

Yuda, Dr. Bao Zhiyong, Dr. Huang Xiaowen, Mr. Li Xing, Dr. Zhu Xuren, Mr. Carl Huang, Dr. Annie Ng. Thanks for their company and support in my life in Hong Kong.

Finally, I would like to give my special thanks to my parents and my sister for their deep love and unconditional support.

Table of Contents

List of Figures

List of Tables

Chapter 1 Introduction

1.1 Background

The rapid industrial development and population growth all over the world during the past decades have led to an explosion in the global demand for energy. However, the energy supply is still mainly relying on the fossil resources like oils and coals, which are known to be limited on the earth and are going to dry up in the near future. Therefore, the increasingly severe energy crisis has urged people to find clean and renewable alternatives to fossil fuels. The solar energy, in contrast, is a very clean and sustainable energy source that can offer inexhaustible supply of energy for human society. Thus, the main challenge now is how to harvest the solar energy in a more efficient way. Photovoltaics (PV), which directly converts solar energy into electric power, is a promising strategy to deal with the energy crisis we are facing now.

Since the first discovery of the PV effect by French scientist Edmund Becquerel in 1839, a variety of photovoltaic materials and PV cells have been invented and developed. **Figure 1.1** shows the current records of cell efficiencies as well as their development process, which is summarized by the National Renewable Energy Laboratory (NREL).[1] Silicon solar cells, which started with a power conversion efficiency (PCE) of 4.5% in 1954, has now surpassed 25% (single-junction, without concentrator). So far, the highest cell efficiency of single-junction structure was achieved by GaAs solar cells, approaching 29%.[1] Several thin film based solar cells, such as CdTe, $Cu(In,Ga)(Se,S)_2$ (CIGS) and organometal halide perovskite cells, have also exhibited promising efficiencies about 22%.[1] Besides, some new generation solar cells have also been studied but normally have low efficiencies: dye-sensitized

solar cells (11.9%), organic solar cells (11.5%), $Cu(Zn,Sn)(Se,S)_2$ (CZTS) solar cells (12.6%) and quantum dot solar cells (13.4%).[1] Although the record efficiencies of various solar cells have been continually increasing during the past decades, however, to date none of them has closely approached the theoretical Shockley and Queisser (S-Q) efficiency limit. There is a long way to go yet for the development of PV technologies.

In terms of practical applications, the wafer-based crystalline silicon (Si) solar modules, however, are still dominating the PV market nowadays due to their high efficiencies, robust long-term stability and the mature industrial manufacturing techniques. Solar modules based on Si materials constitute more than 90% of the market (polycrystalline Si ~ 65%, monocrystalline Si ~35%).[1] Si based solar modules have been proved to have high reliability and good long-term stability, with only small performance degradation after working for more than 20 years. However, the electricity price generated by PV systems now are still relatively higher than that of the normal consumer electricity, which seriously hindered the application proceedings of the PV technologies. In fact, the efficiency of solar modules is a very important factor for the cost reduction of solar systems. The higher PCE can directly translate into a reduced levelized cost of electricity. Thus, for a PV system which can operate well for over 25 years or even longer time, the installation cost will be much less important. Therefore, new photovoltaic materials with lower cost and higher efficiencies are urgently needed.

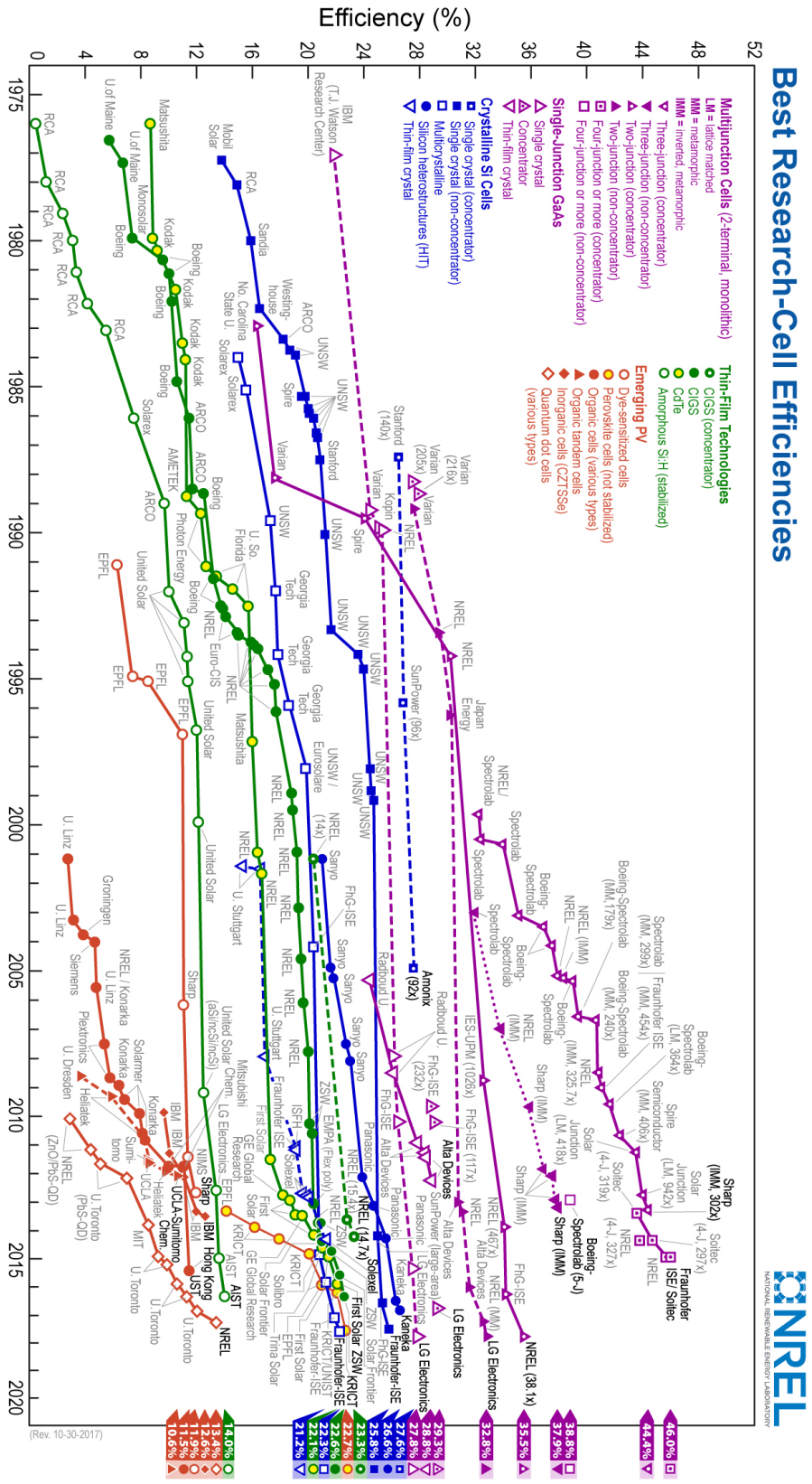

Figure 1.1 The best research-cell efficiencies of various photovoltaic cells. (The chart was created by the NREL)[1]

Inorganic-organic halide perovskite solar cells (PSCs) as one of the rapidly developed PV technologies during recent years, is a promising solution for the future PV generation due to the easy fabrication, low cost and high PCE. The photovoltaic application of this perovskite material was first carried out by Miyasaka and coworkers in 2009.[2] The currently investigated PSCs are dated back to the early invention of solid-state perovskite-sensitized solar cell by Park's group in 2012.[3] So far, the certified cell efficiency of PSCs has now reached 22.7%. However, there are still lots of unsolved questions about the perovskite materials and devices, which need deeper investigation by more researchers in the future.

1.2 Objectives of Research

It is noted that proper choose of electrodes, careful controlling of the crystallization process of the perovskite layer and the effective interfacial modification, are promising strategies to improve the photovoltaic performance of the perovskite solar cells. Therefore, in this thesis, semi-transparent perovskite solar cells with graphene electrodes were fabricated, and high efficiency solar cells with black phosphorous (BP) nano-flakes as interfacial layer as well as solar cells with laser-annealed high-quality perovskite films were introduced. All the solar cells in this thesis were fabricated by facile solution processes with normal structure (bottom electrode/electron transport layer (ETL)/perovskite/hole transport layer (HTL)/top electrode).

Semitransparent solar cells that can absorb light from both sides are promising for some special applications, such as building-integrated photovoltaics,

tandem cells and wearable electronics. However, the development of semitransparent PSCs has been hidered by the quality of transparent top electrodes. An ideal transparent electrode must have high transparency and conductivity, low fabrication cost, robust chemical stability, and excerlent charge collecting ability at the same time. Within the widely used conductive materials, including graphene, CNTs, conductive polymers, and metallic nanowires, graphene is probably the best choice as transparent electrodes, due to its low sheet resistance, high transparency and smooth surface. However, the applications of graphene transparent electrodes in PSCs have never been reported before, although graphene and derivatives have been introduced in PSCs as charge transport layers or buffer layers. Thus, in this thesis, one of the objectives is to adopt the highly transparent CVD graphene as top electrode material to replace the traditional Au electrode in order to realize semi-transparent perovskite solar cells with high transparency together high PCEs.

Interfacial buffer layers which lie between perovskites and charge transport layers often play important roles in energy level band alignment, charge transport, trap passivation and device stability. Materials of for interfacial applications in perovskite solar cells should have high charge mobilities and tunable band gaps. Two-dimensional black phosphorus (BP) with extraordinary electronic properties, such as high carrier mobilities and controllable bandgaps, has excellent potential for interfacial modification. Therefore, our second objective of the thesis is to introduce few-layer BP flakes as buffer layer at the perovskite/HTL interface. This structure is expected to give better band alignment, improve the hole transport property and reduce the recombination loss at the interface, and finally improve the device performance.

The grain size and crystallinity of perovskite films are the most critical factors influencing the performance of PSCs. However, the reported approaches to get

high-quality perovskite thin films are all based on thermal annealing processes at temperatures of around 100 °C, which limits the working area, geometric shape, material choice and mass production of PSCs. Hence, another objective of this thesis is to achieve controllable crystallization of perovskite films by the utilization of laser beam scanning on perovskite surfaces as an alternative approach to the traditional thermal annealing process. After systematical optimization of the laser scanning parameters, high-quality perovskite films of better crystallinity, larger grain size and lower defect density are expected to be obtained, leading to much higher PCEs.

Therefore, we attempted to modify the device structure of perovskite solar cells, including the utilization of transparent graphene as top electrodes, modification of the perovskite/HTL interface with solution processed ultra-thin BP flakes, and controllable fabrication of high-quality perovskite films by laser-annealing approach. These convenient and cost-effective techniques are expected to be useful in realizing high-efficiency perovskite solar cells as well as many other new generation thin film solar cells.

1.3 Outline of Thesis

The chapters of this thesis are listed as follows:

Chapter 1: Introduction. In this part, the background information and the development progress of PV technology are introduced, especially the PSCs. The objectives and outline of this thesis are presented.

Chapter 2: Overview of the Inorganic-organic Hybrid Perovskites for Solar Energy Conversion. In this chapter, a brief history of organic-inorganic hybrid perovskites for photovoltaic applications is reviewed. The basic fundamental properties and state-of-the-art deposition methods of hybrid perovskite materials are

summarized. The evolution process, working mechanisms and device architectures of perovskite solar cells are also described to give a better understanding of high-performance PSCs. Finally, some crucial challenges like long-term stability, I-V hysteresis and toxicity of raw materials are discussed, as well as an outlook towards the further improvement of PSCs.

Chapter 3: Efficient Semitransparent Perovskite Solar Cells with Graphene Electrodes. In this chapter, we have desgined the semitransparent perovskite solar cells by using the CVD graphene transparent electrodes for the first time. The device performance is optimized by improving the conductivity of the graphene electrodes and the contact between graphene and the perovskite active layers during the lamination process. The devices prepared at the optimum conditions show high power conversion efficiencies when they are illuminated from both sides due to the high transparency and conductivity of the graphene electrodes.

Chapter 4: Few-layer Black Phosphorous Flakes for Hole-conducting at Grain Boundaries of Organometal Halide Perovskite Films. In this chapter, the utilization of solution exfoliated BP flakes as an effective buffer layer at the perovskite/HTL interface is introduced. This structure offers better band alignment, improves the hole transport property and reduces the recombination loss at the interface, thus the PCEs were greatly enhanced by over 10%. This study paves a new way of using solution exfoliated thin BP flakes for interfacial engineering of photovoltaic devices.

Chapter 5: Controllable Crystallization of Organometal Halide Perovskite Films with Robotic Laser System. In this chapter, we introduced the utilization of laser beam scanning on perovskite surfaces as an alternative approach to the traditional thermal annealing process. It was noteworthy that the laser scanning parameters, including the laser wavelengths, laser scanning speeds and laser power, were closely related with the crystallization and morphology of the perovskite films. After

systematical optimization, high-quality perovskite films with better crystallinity, larger grain size and lower defect density were successfully fabricated. As a result, we achieved a high open circuit voltage of 1.15 V and a champion efficiency of 20.08% with small hysteresis and excellent long-term stability.

Chapter 6: Conclusions and Future Outlook.

Chapter 2 Overview of The Inorganic-organic Hybrid Perovskite Solar Cells

2.1 Introduction

Solar cells based on inorganic-organic hybrid perovskite materials, have attracted enormous attention during the past few years. Perovskite solar cell was selected as one of the major scientifc breakthroughs in 2013. Since the first report of the material used in solar cells in 2009,[2] the power conversion efficiencies (PCEs) of perovskite solar cells (PSCs) have now reached a certified value of 22.7%,[1, 4] with an unprecedented fast growth rate. PSCs have attained comparable photovoltaic performance to cadmium telluride (CdTe) and copper indium gallium diselenide (CIGS) solar cells (22.1% for CdTe, and 22.6% for CIGS), and is approaching that of monocrystalline silicon solar cells (25.3% for single-junction single crystal Si cells without concentrators).[1] The semiconducting inorganic-organic hybrid perovskites have shown great potential for photovoltaic applications, which are likely attributed to their excellent optoelectronic properties, ease of processing, and low fabrication costs.

The organic-inorganic hybrid perovskite materials possess several outstanding optoelectronic properties which make them ideal materials for photovoltaic applications. The bandgap of the mostly often used methylammonium lead iodide perovskite ($CH_3NH_3PbI_3$, abbreviated as $MAPbI_3$) is nearly ideal for light absorption and it can be continuously tuned from 1.17 eV to 2.3 eV through compositional engineering. The optical absorption coefficient of $MAPbI_3$ is higher than many other

photoactive materials such as Si, CdTe, and amorphous silicon, thus the film thickness of the active layer can be reduced to only several hundred nanometers. Compared with materials used in OPVs, the low exciton binding energy of the hybrid perovskites allows the spontaneous dissociation of excitons into free carriers upon light absorption. Moreover, the high electron and hole mobilities as well as the long carrier lifetimes result in the long diffusion lengths, thus electrons and holes can be successfully transported to the electrodes before recombination happens.

In addition to the outstanding optoelectronic properties, the processing of PSCs has shown excellent flexibility. High-quality perovskite films can be easily fabricated through either solution or vapor-phase deposition, which will be discussed in the following sections. A large number of research groups all over the world, especially those with experiences on OPVs and DSSCs, have been attracted to work on this hot research topic, because of its easy of processing. As a result, this research area has experienced a tremendous development during the past few years.

Besides, all the components of the hybrid perovskites are quite cheap materials including some organic compounds (e.g., methylammonium (MA) and formamidinium (FA)) and inorganic elements like lead and iodine. Thus the cost for raw materials of PSCs is dramatically decreased compared with other photovoltaic techonologies. Also, the processing cost of PSCs is quite low because of the facile fabrications conditions.

Despite demonstrations of high efficiencies, PSCs have also been suffering from some severe problems like long-term stability, I-V hysteresis and toxicity of raw materials (containing lead), which hindered its large-scale commercial applications. How to address these issues has turn out to be the main challenge for the future development. In this chapter, we first summarize briefly the fundamental properties of the hybrid perovskite materials. And the state-of-the-art deposition methods of the perovskite films are presented in the following part. We then review

the development process of organic-inorganic hybrid PSCs. The working mechanisms and device architectures of perovskite solar cells are also described to give a better understanding of high-performance PSCs. Finally, some crucial challenges like long-term stability, I-V hysteresis and toxicity of raw materials are discussed, as well as an outlook towards the further improvement of PSCs.

2.2 Fundamental Properties of Hybrid Perovskites

2.2.1 Crystal Structures

The organic-inorganic hybrid perovskites generally have a chemical formula of ABX_3 (where A is MA or FA, MA= $CH_3NH_3^+$, FA=$CH_3(NH_2)_2^+$; B represents Pb^{2+} or Sn^{2+}; X stands for Cl^-, Br^- or I^-). In a standard cubic crystal structure, the body-centred cation B has six nearest X anions, while the cation A located at vertex positions possesses twelve nearest X anions, as shown in **Figure 2.1a**. In order to maintain a stable crystal structure, it is generally accepted that the tolerance factor t (t=(r_A+r_X)/[$2^{1/2}$(r_B+r_X)], where r_A, r_B, r_X represent the effective ionic radii for A, B and X ions) should be in the range between 0.813 and 1.107.[5] Thus, for the compositional change of perovskites, the tolerance factor should be carefully considered according to the ion radius of the cations and anions. It is interesting that the hybrid perovskites undergo structural phase transitions upon temperature change because of the rotation of A-site cations at high temperatures.[5, 6] For example, $MAPbI_3$ perovskite with a stabilized orthorhombic structure at low temperatures, will have an orthorhombic to tetragonal phase transition at around 162 K. Further increase of the temperature to 327 K, another phase transition process (from tetragonal to cubic) will occur. The schematic crystal structures of these three phases are shown in **Figure 2.1**. A similar phase transition occurs at lower temperatures for $MAPbBr_3$ and $FAPbI_3$, which gives them better thermal stability. [5, 6]

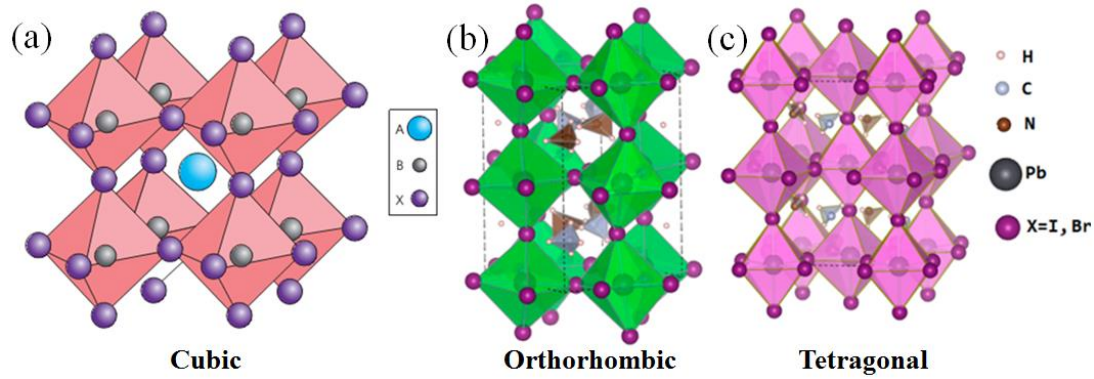

Figure 2.1 Schematic diagram of the crystal structures of organic-inorganic hybrid perovskites. Reprinted with permission from ref.[7, 8]

2.2.2 Optical Properties

The hybrid perovskite materials have been confirmed to be exceptionally good at absorbing photons. Being direct bandgap semiconductors, the hybrid perovskites possess extremely high absorption coefficients, with reported values in the order of 10^5 cm^{-1}.[9] Thus, a 400-nm thick perovskite film is generally thick enough to absorb most of the light, which greatly reduced the material costs.[10, 11] Compared with light absorbing materials used in organic solar cells, the exciton binding energy of organic-inorganic hybrid perovskites was demonstrated to be only 16 meV at low temperatures, and this value can further decrease to a few millielectronvolts at room temperature, which explains their outstanding device performance as being due to spontaneous free-charge separation upon light illumination.[12]

The colour of the hybrid halide perovskites is tunable through compositional engineering, covering the entire visible range and extending to the near infrared region. Seok and co-workers studies the chemically tuned organic-inorganic hybrid perovskite materials based on $MAPb(I_{1-x}Br_x)_3$ which show bandgap covering almost the whole visible light range, contributing to the realization of colourful solar cells.[13] Their work represents one step toward the realization of colorful solar cells with low-cost, high-efficiency and long-term stability. The color-tuned PSCs have been proved to be a promising solution for building integrated photovoltaics (BIPVs).

The hybrid perovskites also show strong photoluminescence (PL). The PL spectra are different for various organometal halide perovskite materials. In most reports at room temperature, the $MAPbI_3$ perovskite has a PL emission peak at around 775 nm, while $FAPbI_3$ has a peak at around 800 nm.[14, 15] Compared with lead-based perovskites, the tin-based perovskites, like $MASnI_3$, which has a smaller bandgap, shows a broader PL peak at ~ 980 nm.[16] The PL peaks of $(MA)_x(FA)_{1-x}PbI_3$ (x varies from 0 to 1) films can be continuously tuned by changing the molar ratio between MA and FA cations, ranging from 776 nm to 803 nm.[15] The gradual shift in PL emission shows the existence of a solid solution of FA and MA in the perovskite lattice.[15] Similarly, a gradual shift in PL peaks is also observed in $CH_3NH_3Pb(I_{1-x}Br_x)_3$ films (x = 0 ~ 1) by tuning the iodide-bromide ratio.[17]

2.2.3 Charge Transport Properties

One of the most important features of all the semiconducting materials is the charge transport property. The outstanding performance of organometal halide perovskites is partly attributed to their excellent charge transport properties. The small photocarrier effective masses, long carrier lifetimes, long diffusion lengths, high carrier mobilities, and low trap densities ensure that the carriers can be successfully transported across the entire perovskite film (normally several hundred nanometers) before recombination.[18-24]

Originally in 2013, the electron and hole diffusion lengths of solution processed $MAPbI_3$ perovskite films were calculated to be around 100 nm (the carrier lifetime is only several nanoseconds) based on the results of transient optical spectroscopy and time-resolved PL-quenching measurements.[21] This value of carrier diffusion length at that time was actually already much higher than that of the traditional low-temperature solution-processed light absorbers (typically ~ 10 nm).[21] It was also found that the diffusion lengths of $MAPbI_{3-x}Cl_x$ perovskites are larger than 1 μm,

which is higher than the triiodide perovskite absorbers in an order of magnitude.[20] Owing to the much longer carrier diffusion lengths of mixed halide perovskites than the light absorption depth (100 ~ 200 nm), the mesoporous TiO_2 structure is no longer necessary so that planar structure is adoptable.[20] The charge carrier mobilities of solution-processed organometal trihalide perovskite films are firstly estimated to be around 10 ~ 20 $cm^2V^{-1}s^{-1}$, which is rather high for solution-processed materials.[23, 24]

The successful growth of large organometal trihalide perovskite single crystals in 2015 greatly promoted our understanding about the bulk electrical properties of this material.[19, 22, 25] Huang's group reported that the diffusion length in the solution-grown $MAPbI_3$ single crystals can exceed 175 μm under 1 sun illumination, and is larger than 3 μm under weak light condition, which has far exceeded the diffusion length obtained in organometal perovskite thin films.[22] In addition, the carrier mobility they measured in $MAPbI_3$ single crystals was as high as 164 $cm^2V^{-1}s^{-1}$, and the trap density was calculated to be as low as 3.6×10^{10} cm^{-3}.[22] Cooke *et al.* even reported a record high mobility of 800 $cm^2V^{-1}s^{-1}$ on a single crystal lead halide perovskites through optical pump-multi-THz measurements.[25]

2.2.4 Compositional Engineering and Bandgap Tuning

The dominating perovskites ($MAPbI_3$) possess a bandgap around 1.5 eV, which is extremely close to the 'ideal' single-junction bandgap (1.1 eV ~ 1.4 eV).[13, 26, 27] Depending on the different kinds of halide included, the bandgap can be continuously tuned from ~ 1.5 eV (pure I) to ~ 3.2 eV (pure Cl).[13, 27, 28] Even smaller bandgaps can be achieved by adopting different organic cations or inorganic cations, covering the entire visible spectral range and expanding to the near infrared region.[10, 28]

The bandgap of $MAPbI_3$ perovskite was estimated to be ~ 1.5 eV from UPS,

UV-visible, and IPCE spectra. However, the ~ 1.5 eV bandgap is not enough to cover the whole visible and the near-infrared region, which is necessary to get ultra-high power conversion efficiency. Therefore, bandgap tuning is generally considered to be a good way to expand the absorption range of this material.

One approach to realize the bandgap tuning is to replacing MA with other organic cations (e.g., FA, 5-AVA) or inorganic cations (e.g., Cs, Rb), because changing the organic cations at A sites of AMX_3 perovskites can tune the bandgap by modifying the metal-halide-metal bond length and angle without affecting the valence band maximum.[29] Partial replacement of MA with FA is an effective way to extend the light absorption range and improve the thermal stability.[27] With the combination of FA, MA and Cesium (Cs), the resulting triple-cation perovskites are less sensitive to processing conditions, thermally more stable and show higher PCEs with better reproducibility.[30, 31] Besides, the bandgap of the hybrid perovskites can also be continuously tuned from 1.5 eV to 2.3 eV by using of mixed halides (I and Br).[13] The bromide element included can also improve the stability of the perovskite films in ambient conditions.

In addition to altering the organic cations and the halide anions, another approach for tuning the bandgap is the direct change or substitution of the metal cations. For instance, the bandgap of $MASn_xPb_{1-x}I_3$ perovskites can be tuned from 1.3 eV to 1.55 eV by changing the ratio of Pb and Sn.[32] Due to concerns about the toxicity of Pb, lead-free perovskites such as $MASnX_3$, have drawn increasing attention recently. Compared with the Pb-based perovskite, the relatively lower band gap of $MASnI_3$ (~ 1.3 eV) allows light absorption over a much broader range with an increased current density. However, both the efficiency and the stability of the Sn-based devices are still not comparable to that of the lead-based cells at this moment.

2.3 Synthesis of hybrid perovskite crystals

Much efforts have been devoted by researchers to obtain high quality organometal halide perovskite films for PV applications. However, the synthesis of high-quality large perovskite single crystals as well as a variety of nanostructures are still of great importance to the fundamental research about the physical properties of these materials and a better understanding of the crystal growth process.

2.3.1 Bulk Crystal Growth

The growth of organometal halide perovskite bulk crystals are generally similar to the traditional solution-based crystal-growth methods. In most cases, the oversaturated perovskite precursor solution with organic halide salts and inorganic lead halide salts, is slowly cooled to evaporate the solvents and form the hybrid perovskite single crystals. So far, many researchers have reported the successful synthesis of large hybrid perovskite single crystals up to centimeter scale.[19, 22, 33-35]

Bakr *et al.* reported a antisolvent vapor-assisted crystallization (AVC) process to grow high-quality, millimeter-sized $MAPbBr_3$ and $MAPbI_3$ single crystals with ultra-low trap densities ($10^9 \sim 10^{10}$ cm^{-3}) and high charge carrier diffusion lengths (> 10 μm).[19] In this method, the antisolvent dichloromethane (DCM) is slowly diffused into the perovskite solution to promote the growth perovskite crystals of high quality and controllable crystal size. This concept of antisolvent method has also been widely used to fabricate high-quality perovskite thin films through a fast-crystallization process. Bakr and co-workers also developed an inverse temperature crystallization (ITC) method to grow $MAPbBr_3$ and $MAPbI_3$ crystals at a rate much faster than the previously reported methods.[33] This method is based on the phenomenon that the solubility of $MAPbBr_3$ or $MAPbI_3$ in DMF drops dramatically with the increase of solution temperature from room temperature to

80ºC. This inverse solubility phenomenon was utilized to grow $MAPbX_3$ crystals rapidly from hot precursor solutions by carefully controlling the solution temperature and concentrations.

By using a top-seeded solution-growth (TSSG) method, Huang and co-workers grew large-sized $MAPbI_3$ single crystals (the largest size is around 10 mm) with electron-hole diffusion lengths larger than 175 μm under 1 sun illumination.[22] In this process, small $MAPbI_3$ crystals at the bottom of the solution in a container were used to help maintain a saturated solution while the cooler top half of the solution was supersaturated. Thus, a crystal seed put in the top region of the solution can grow into larger size by consumption of small crystals in the bottom. Recently, Liu *et al.* also developed a facile method to prepare inch-sized $MAPbX_3$ (X = Cl, Br, I) perovskite crystals (the largest one is 71 mm * 54 mm * 39 mm) based on a seed-induced heterogeneous nucleation mechanism.[34]

2.3.2 Nanocrystal Synthesis

In the early work on synthesis of hybrid perovskite nanocrystals, a mesoporous TiO_2 or Al_2O_3 films were normally used for the control the perovskite nanocrystals' growth.[36, 37] In these reports, the regular perovskite precursor solution for solar cell fabrication was used and no surfactant ligands were adopted, thus the crystal size was actually controlled by the pore size of these mesoporous scaffold.

Later, a series of hybrid perovskite nanostructures with different sizes and morphologies were synthesized through various solution processes without using of templates. Jin *et al.* successfully fabricated single crystalline nanowires, nanorods, nanobelts, and nanoplates of $MAPbI_3$ and $MAPbBr_3$ perovskites through a dissolution-recrystallization conversion from lead halide films coated on substrates to perovskites.[38] These perovskite nanocrystals show stronger room-temperature photoluminescence and longer carrier lifetimes than the bulk crystals and thin films.

Galian *et al*. reported the non-template synthesis of monodispersed 6nm-sized hybrid $MAPbBr_3$ perovskite nanoparticles for the first time.[39] The medium-sized chain alkyl ammonium bromide was used to react with $PbBr_2$ in the presence of oleic acid and octadecene. These nanoparticles can be dispersed and kept stable in a variety of solvents for more than three months. By using similar methods mentioned above, all-inorganic lead halide nanocrystals (e.g., $CsPbX_3$) can also be obtained from inexpensive commercial raw materials.[40] Through compositional modulations, the emission spectra are widely tunable from 410 nm to 700 nm, which makes them appealing for many optoelectronic applications.

In addition to the three-dimensional organic-inorganic hybrid perovskites, the two-dimensional counterparts are also fairly appealing for their special novel features and wide applications. Two-dimensional $MAPbX_3$ (X = Cl, Br or I) perovskite nanosheets with thickness of single unit cell were synthesized by Bao and co-workers using a hybrid method which combines the solution and vapor-phase processes.[41] The high-quality two-dimensional nanocrystals exhibit high photoluminescence with broad wavelength tunability. Yang's group reported the direct growth of atomically thin single-crystalline two-dimensional hybrid $(C_4H_9NH_3)_2PbBr_4$ perovskites from solution-phase growth.[42] Much larger organic cations are needed for the fabrication of this kind of layered two-dimensional perovskites.

2.4 Deposition Methods of Perovskite Films

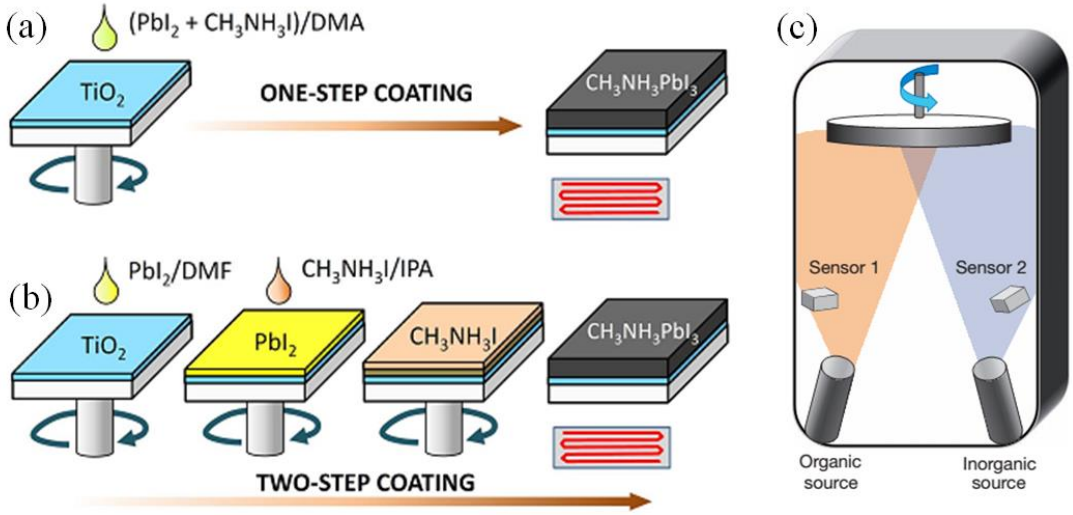

Figure 2.2 Schematic illustration of the one-step (a) and two-step (b) spin-coating procedures for the fabrication of perovskite films. Reprinted with permission from ref.[43] (c) Dual-source thermal evaporation system for depositing the perovskite absorbers. Reprinted with permission from ref.[44].

In order to prepare high-efficiency PSCs, the fabrication of high-quality perovskite films is the most important process. So far, a variety of deposition methods have been developed by researchers. The most widely adopted deposition methods for perovskite films can be categorized into three groups: one-step solution process, two-step solution process and vapor-phase deposition.

2.4.1 One-step Solution Process

For standard one-step solution method (as shown in **Figure 2.2a**), the perovskite raw materials including lead sources (PbI_2, $PbCl_2$, etc.) and organic sources (MAI, FAI, etc.) are firstly dissolved in appropriate solvents such as dimethyl formamide (DMF), GBL or DMSO, and the solution was then spin-coated on the substrate. A subsequent thermal annealing process (mostly around 100 ºC) for a proper period of time is needed in most cases for the complete crystallization of the

perovskite film.

One-step solution process was firstly used for the fabrication of $MAPbI_{3-x}Cl_x$ perovskite films from a mixed solution of $PbCl_2$ and MAI (with a 1:3 molar ratio) in DMF.[45] The annealing process of the $MAPbI_{3-x}Cl_x$ films is extremely sensitive to the temperature, and thus the film coverage and morphology is hard to control. In addition, the annealing atmosphere is just as important since the crystallization process is susceptible to the solvent atmosphere in the glovebox or moisture in air. Yang *et al.* have reported that the thermal annealing process for $MAPbI_{3-x}Cl_x$ film under proper humidity in air can effectively improve the film morphology and carrier lifetime.[46, 47]

In the case of $MAPbI_3$-based perovskites, it is also difficult to fabricate high-quality and uniform perovskite films through a simple one-step spin-coating process owing to the film shrinkage phenomenon, which is related to the simultaneous solvent evaporation and perovskite crystallization. Generally, two strategies are used to address this problem, i.e., slow-crystallization and fast-crystallization. Interestingly, it was demonstrated that some additives (such as HI[26, 48] and MACl[49]) can greatly improve the morphology and coverage of perovskite films by retarding the crystallization process. However, the slow-crystallization annealing process often takes a relatively long time, which will prolong the preparation period.

Recently, an anti-solvent rapid crystallization process has been widely adopted by researchers. Cheng *et al*. reported that the dripping of chlorobenzene during the one-step spin-coating process could induce fast crystallization, and thus very flat and uniform perovskite films with large grain size could be obtained.[50] The role of chlorobenzene is to rapidly reduce the solubility of the perovskites in the mixed solvents for the rapid precipitation and growth of perovskite grains. Soek's group also developed a novel solvent-engineering technique for high-performance PSCs.[27,

[51] The adoption of a mixed solvents of GBL and DMSO followed by toluene dripping could lead to quite uniform and dense perovskite layers through the formation of a PbI_2-MAI-DMSO intermediate phase. The solar cells prepared with this method exhibited a PCE of 16.2%, which was further improved to 17.9% by delicate compositional engineering. To date, this one-step anti-solvent fast crystallization process have already been widely adopted for fabricating PSCs with PCEs higher than 20%.[30, 31, 52]

2.4.2 Two-step Solution Process

For the two-step solution process in very early stages,[53] PbI_2 is normally desolved in DMF and spin-coated on the substrate to form a PbI_2 layer, and the as deposited film is kept at a low temperature (e.g., 70ºC) for a certain time. After drying, the film is immersed into a 2-propanol solution of MAI (e.g., 10 mg/ml) for appropriate time and is then rinsed in pure 2-propanol to wash away the residual MAI. Normally, a further thermal annealing process is also required for crystallization. Gratzel *et al.* firstly adopted this two-step solution process and successfully achieved a certified efficiency of 14.1%.[53]

Later, a thermal annealing-induced inter-diffusion method was developed by Huang's group to fabricate pin-hole free perovskite films.[54] As is illustrated in **Figure 2.2b**, the stacked PbI_2/MAI bilayer structure will convert to perovskites upon thermal annealing. A lot of groups later adopted this approach for the fabrication of PSCs with relatively high efficiencies.[55-58]

2.4.3 Vapor-phase Deposition

Thermal evaporation, which is often used to deposit metal electrodes, can also be adopted to fabricate perovskite films. **Figure 2.2c** shows a dual-source thermal evaporation system that was firstly used for the depositing of uniform flat perovskite

absorbers.[44] $PbCl_2$ and MAI (molar ratio, 4:1) were evaporated simultaneously from two separate ceramic crucibles in an evaporation chamber at 10^{-5} mbar. The crystallization started immediately after the evaporation judged according to the color change. Further thermal annealing was needed to get fully crystallized perovskite films. Compared with solution processed perovskite films, the vapor-deposited ones were extremely uniform, and the surfaces were quite flat without pin-holes or voids. The solar cells based on the vapor-deposited perovskite film demonstrated an efficiency higher than 15%. The deposition rates of the two precursor materials are crucial for the fabrication of high-quality perovskite films. However, it is often found difficult to precisely control the molar ratio of the two precursor materials. To solve this problem, a layer-by-layer growth method was developed to fabricate $MAPbI_{3-x}Cl_x$ films with desired thickness for high performance and stable PSCs.[59] Briefly, a thin layer of $PbCl_2$ (~ 50 nm thick) was evaporated on the substrate, and then dipped in the 2-propanol solution of MAI, so that it was transferred into perovskite. And this process was repeated for several times to get the desirable final thickness. PSCs fabricated through this approach showed PCEs up to 15%. However, the thermal deposition process requires high vacuum and expensive equipment, which is energy consuming and is incompatible with large-scale mass production. What's more, the growth condition and mechanisms of vapor deposition are relatively complicated, which hinders the large-scale application of this technique.

2.5 Efficiency Roadmap of Perovskite Solar Cells

From the best-research cell efficiencies chart made by the National Renewable Energy Laboratory (NREL),[1] it is obvious to see that the efficiency of PSCs has been growing at an unprecedented rate, which is much faster than that of all the other

types of solar cells. Some of the landmark efficiencies during its development process was exhibited in **Figure 2.3** based on published papers or certified efficiencies. [2, 3, 27, 30, 36, 45, 46, 51, 53, 55, 60] In the year of 2009, Miyasaka and co-workers reported the photovoltaic effect of the inorganic-organic lead halide perovskite materials for the first time.[2] The perovskite nanocrystalline particles ($MAPbBr_3$ and $MAPbI_3$) self-organized on TiO_2 surface were adopted as visible-light sensitizers in the dye-sensitized solar cells (DSSCs) with liquid electrolyte. A PCE of 3.8% on a $MAPbI_3$-based cell was obtained. The efficiency was actually much lower than that of the conventional DSSCs (~ 11%) at that time, and the perovskite compounds showed very poor stability in the liquid electrolytes. Two years later, Park *et al*. prepared a perovskite quantum-dot-sensitized solar cell with PCE of approximately 6.5% by using 2 ~ 3 nm sized $MAPbI_3$ nanocrystals.[36] However, the lifetime of the perovskite quantum-dot-sensitized solar cell was only about 10 minutes due to the easy dissolution of the perovskite nanocrystals in the liquid electrolyte. Thus, not much attention had been paid to the hybrid perovskite materials by researchers before the successful fabrication of the first all-solid-state mesoscopic solar cells with impressive PCE of 9.7% by Park's group in 2012.[3] The use of a solid hole transport material (spiro-MeOTAD) dramatically improved the efficiency as well as the device stability compared with the former electrolyte-based perovskite sensitized cells. This improvement led to a fast development of research about PSCs. Since then, PSCs have attracted more and more attention worldwide. Soon after, in the same year, Snaith and his co-workers pushed the efficiency of PSCs to 10.9% with dramatically improved V_{oc} (0.98 V) by coating a new mixed-halide perovskite ($MAPbI_2Cl$) on the surfaces of a mesostructured insulating Al_2O_3 scaffold, termed as "meso-superstructured solar cell" (MSSC).[45] This iodide-chloride mixed-halide perovskite was found to be more stable in air and possessed better electron diffusion property than the previously reported pure iodide

equivalent.

In 2013, Gratzel and Seok *et al*. introduced a layered sandwich-type device structure, comprising of a 3D-nanocomposites of mesoporous TiO_2 scaffold (infiltrated with perovskite material), a dense well-crystallized $MAPbI_3$ perovskite capping layer and a polymeric hole transport layer. By comparison of several different kinds of hole transport materials, they found that PTAA provided the maximum efficiency of 12.0% under standard AM 1.5 light illumination, with a substantially increased FF (72.7%). Later in 2013, Gratzel *et al*. obtained a PCE of 15.0% (with a certified PCE of 14.1%) with improved perovskite morphology through a sequential deposition route (also called two-step method),[53] which was widely adopted by other researchers ever after. This technique for the fabrication of perovskite material increased the reproducibility compared to the previously employed one-step route, and provided with opportunities for high-performance PSCs. A close PCE of 15.4% with an V_{oc} of 1.07 V was illustrated by Snaith and his co-workers by using a sequential vapour-deposited $MAPbI_{3-X}Cl_x$ perovskite layer.[44] It was proved that the mesostructured TiO_2 scaffold was not necessary and a simple planar heterojunction thin-film structure can also achieve high photovoltaic performance, although this device structure tend to show more significant hysteresis phenomenon in current-voltage (*I-V*) characteristics.

Soon afterwards, Seok's research team reported a certified PCE of 16.2% without *I-V* hysteresis by using $MAPb(I_{1-x}Br_x)_3$ as active material and PTAA as a hole transport layer.[51] A solvent-engineering technique was developed to obtain extremely dense and uniform perovskite films. Here, GBL and DMSO were mixed for the preparation the perovskite precursor solution. The better morphology was actually due to the formation of the intermediate phase PbI_2-MAI(Br)-DMSO film when non-dissolving solvent (such as toluene) was drop-casted during the spin-coating process. For this kind of bilayer architecture, the thickness ratio of the

continuous perovskite upper layer and the mp-TiO_2 layer (also infiltrated with perovskites) is the key factor for the brilliant performance. This was further increased to a confirmed PCE of 17.9% also by Soek's group in early 2014.[27] A mixed composition of $(FAPbI_3)_{1-x}(MAPbBr_3)_x$ was used as light absorber. According to their report, the incorporation of $MAPbBr_3$ into $FAPbI_3$ could stabilize the perovskite phase and improved the efficiency. Besides, Yang's group also reported a high PCE of 19.3% in a planar device geometry by means of a delicate interface engineering throughout the entire device.[46]

In late 2014, Seok and his colleagues reported an exciting PCE of 20.1%,[55] which was the first one that surpassed the 20% mark. The perovskite film was fabricated essentially through a two-step solution process. Unlike the conventional two-step method, the PbI_2 film was replaced by a PbI_2(DMSO) complex film, which will interact with FAI (MABr) in 2-propanol through an intramolecular exchange process (IEP). Negligible volume expansion occurred during the IEP process and high-quality perovskite film was obtained. High efficiency PSCs with average efficiency of over 19% can be obtained through this technique.

In late 2015, Saliba *et al*. reported a higher efficiency of 21.1% by employing a triple-cation perovskite composition (FA/MA/Cs),[30] which were thermally more stable, and more robust to the fabrication conditions. This provide a novel strategy for the further improvement of PSCs. In early 2016, a new record efficiency of 22.1% was developed by KRICT and UNIST. Details of this work were discussed in the paper published on Science in 2017.[4] It was dementrated that the introduction of additional iodide into the perovskite precursor solution can effectively decrease the concentration of deep-level defects in the perovskite film, yielding a certified PCE of 22.1%. Over 93% efficiency of this cell was maintained after 13 months of storage at ambient conditions. Further improvement of the PCEs of PSCs is on the way. The current record efficiency of PSCs is 22.7% as shown in the efficiency chart made by

NREL in Figure 1.1.

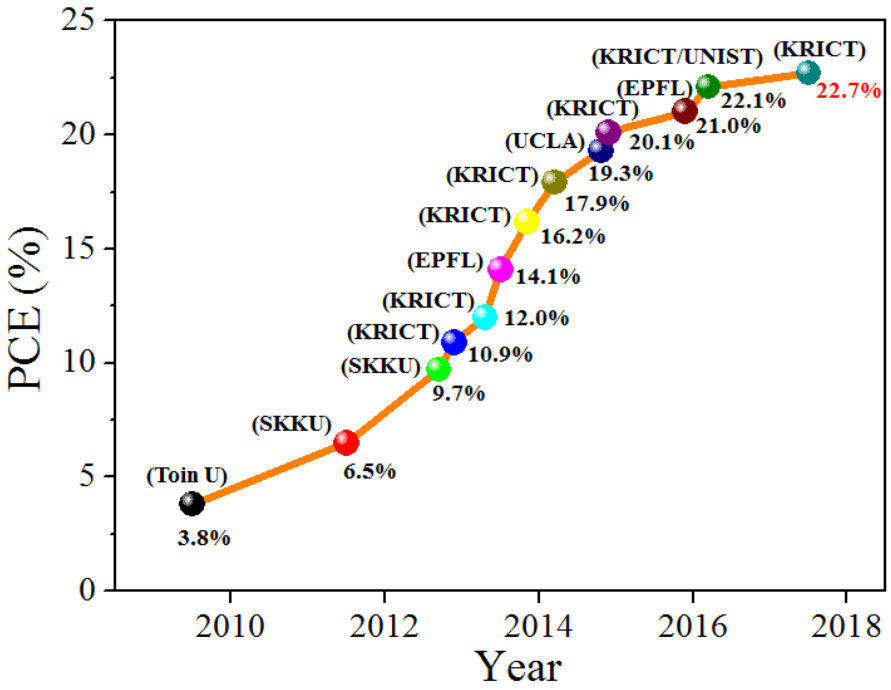

Figure 2.3 Efficiency roadmap for inorganic-organic hybrid PSCs.[2, 3, 27, 30, 36, 45, 46, 51, 53, 55, 60]

Table 2.1 Summary of the device information corresponding to efficiencies shown in Figure 1. (mp=mesoporous)

Device structure	J_{sc} (mA/cm^2)	V_{oc} (V)	FF	PCE (%)	Year	Ref.
mp-TiO_2/$MAPbI_3$/liquid electrolyte	11.0	0.61	0.57	3.8	2009	[2]
mp-TiO_2/$MAPbI_3$-QDs/liquid electrolyte	15.82	0.706	0.586	6.5	2011	[36]
mp-TiO_2/$MAPbI_3$/spiro-MeOTAD	17.0	0.888	0.62	9.7	2012	[3]
mp-Al_2O_3/$MAPbI_2Cl$/spiro-MeOTAD	17.8	0.98	0.63	10.9	2012	[45]
mp-TiO_2/$MAPbI_3$/PTAA	16.5	0.997	0.727	12.0	2013	[60]
mp-TiO_2/$MAPbI_3$/spiro-MeOTAD	20.0	0.993	0.73	15.0	2013	[53]
mp-TiO_2/$MAPb(I_{1-x}Br_x)_3$/PTAA	19.64	1.11	0.742	16.2	2013	[51]
mp-TiO_2/$(FAPbI_3)_{1-x}(MAPbBr_3)_x$/PTAA	21.84	1.114	0.736	17.9	2014	[27]
Y:TiO_2/$MAPbI_{3-x}Cl_x$/spiro-MeOTAD	22.75	1.13	0.75	19.3	2014	[46]
mp-TiO_2/$(FAPbI_3)_{1-x}(MAPbBr_3)_x$/PTAA	24.7	1.06	0.775	20.1	2015	[55]
mp-TiO_2/$Cs_x(MA_{0.17}FA_{0.83})_{(100-x)}Pb(I_{0.83}Br_{0.17})_3$ /spiro-MeOTAD	23.5	1.147	0.785	21.1	2015	[30]
mp-TiO_2/$(FAPbI_3)_{1-x}(MAPbBr_3)_x$/PTAA	25.0	1.1	0.803	22.1	2017	

2.6 Working Mechanisms and Device Architectures

The operation of a solar cell requires four basic processes, i.e., light absorption and generation of excitons, charge separation, charge transport and charge collection. For light absorbers with different optoelectronic properties, diverse device structures are selected. For example, an n-i-p (or p-i-n) structure is needed if the light absorbing material is an intrinsic semiconductor, while only a p-n structure is needed when the active material itself has a p-type (or n-type) property. Thus, the organic-inorganic hybrid perovskite materials are suitable for either p-i-n or p-n structures owing to their long-range balanced ambipolar charge transport nature.[21]

The original perovskite solar cells employed a mesoporous structure with a thick mesoporous layer (mp-Al_2O_3 or mp-TiO_2) as scaffold,[2, 3, 36, 45, 53] which was evolved from the typical DSSCs. In this structure, as shown in **Figure 2.4a**, the mesoporous scaffold is filled with perovskites and located between ETLs (mostly TiO_2) and HTLs layers. The mesoporous structure is proved to be able to increase the charge collection efficiency by decreasing the charge transport distance. In the very early stage, the thickness of the mesoporous layer was generally larger than 500 nm (or even several micro meters), in order to absorb enough sunlight. [2, 3, 36, 45, 53] However, because the dimensions of the pores can confine the crystal growth of perovskites, a certain part of the material exist in amorphous phases with poor crystallinity,[61] which will definitely deteriorate the device performance.

Interestingly, if the mesoporous layer thickness decreases to less than 300 nm, a dense perovskite capping layer with large grains will form on top of the porous layer,[27, 30, 51, 55] which is called a bilayer structure (shown in **Figure 2.4b**). The complete pore filling together with the superior crystallinity of the continuous perovskite capping layer can assure the high charge collection and transport efficiencies. As a result, PSCs based on the bilayer structure have demonstrated

much higher efficiencies than that of the traditional mesoporous structure.[27, 30, 51, 55] Actually, the state-of-the-art PSCs are usually based on this device configuration.[30, 31, 52, 55, 62]

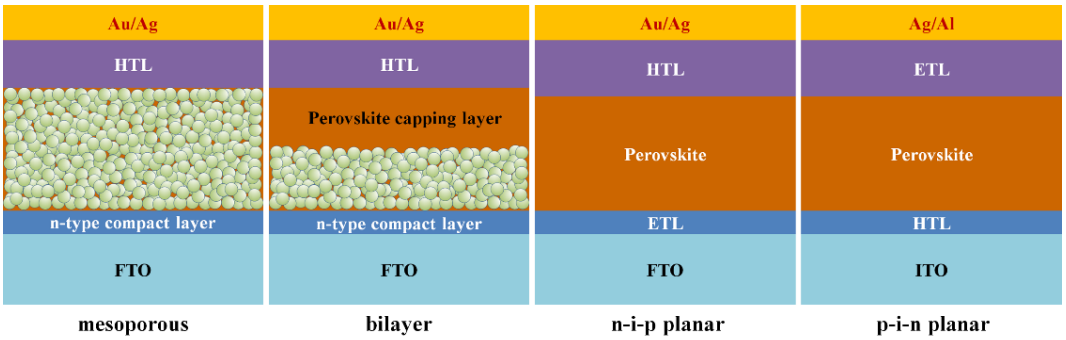

Figure 2.4 Schematic illustration of the mesoporous, bilayer, n-i-p planar and p-i-n planar device architectures of PSCs. HTL represents the hole transport layer; ETL represents the electron transport layer.

Further development of the device architectures brings out the n-i-p or p-i-n planar configurations (as shown in **Figure 2.4c** and **2.4d**), which are similar to organic solar cells (OPVs). In planar structures, the mesoporous layer is omitted, and the perovskite layer is sandwiched between the ETLs and HTLs, which simplifies the preparation process and is more compatible with low-temperature fabrication processes. To date, the best n-i-p planar devices have efficiencies around 19% with different electron transport layers (TiO_2, SnO_2 etc.).[46, 63, 64] Recently, the p-i-n planar devices have also demonstrated efficiencies higher than 18% due to the employments of advance film preparation methods.[48, 56, 57, 65, 66]

2.7 Key Challenges of Perovskite Solar Cells

Despite of their excellent PV performances, the hybrid perovskite solar cell is currently still a fragile new star in the photovoltaic community. There are a variety of challenging issues to be addressed before the commercial applications.

2.7.1 Long-term Stability

Compared with the enormous breakthrough in device efficiencies of PSCs, study on the long-term stability has been lagged far behind. However, the long-term stability is as important as the device efficiency before PSCs can be used in the market. High efficiencies are meaningless if the solar cells are unstable.

Some representative stabilities are listed in **Table 2.2**. In 2011, the perovskite quantum-dot-sensitized solar cell fabricated by Park's group (with PCE of 6.5%),[36] suffered an 80% degradation in just 10 minutes, because the liquid electrolyte tends to dissolve the perovskite quantum dot gradually. By 2012, the device stability was improved substantially from minutes to over 500 hours thanks to the employment of all-solid-state hole transport material (spiro-MeOTAD), which was a revolutionary step for long-term stability. Moreover, the PSC based on the two-step sequential process, developed by Gratzel *et al.*, could also maintain more than 80% of the original PCE after 500 hours.[53] In order to overcome the ultraviolet light instability of mesoporous TiO_2 film, Snaith and co-workers developed a TiO_2-free cells with Al_2O_3 scaffold, which delivered stable photocurrent for over 1000 hours under continuous full spectrum sunlight.[67] Similarly, a polymeric hole transport material PDPPDBTE was used by Park *et al*. to replace spiro-MeOTAD.[68] The stability of the PDPPDBTE cells were improved remarkably, and the initial efficiency showed almost no degradation after long-term aging test of 1000 h. The excerlent stability of the devices may be attributed to its hydrophobic properties, which prevented water penetration into the perovskite layer.

In 2014, Han and co-workers reported a novel hole-conductor-free mesoporous device structure with considerably high stability.[69] They employed a mesoporous TiO_2/ZrO_2/carbon triple-layer structure, filled with perovskite by drop-casting of the perovskite solution, so that no hole transport layer is required. The cell had a certified efficiency of ~ 13%, which was very stable for over 1008 hours in ambient

air under AM 1.5 simulated sunlight.

Besides, some recent work on device stability indicated that the use of inorganic charge transport layers was quite effective to maintain long-term stability.[70, 71] For example, Han *et al*. adopted two highly doped inorganic charge transport layers in the planar structure of FTO/NiMgLiO/$MAPbI_3$/PCBM/Ti(Nb)O_x/Ag.[70] The robust nature of these inorganic layers allowed for the long-term stability (maintaining over 90% of the initial efficiency after long light soaking for over 1000 hours). Yang *et al*. fabricated PSCs with inorganic NiO_x and ZnO nanoparticles as charge transport layers[71] About 90% of the original efficiency could be retained after 60 days of storage without encapsulation. The dense and robust ZnO layer, was not only capable of isolating the perovskite layer and the top metal electrode, but also may serve as an excellent diffusion barrier against moisture.

Some recent studies have reported that adding a quite small amount of inorganic cesium (Cs) into the perovskite recipes can produce efficient solar cells that are far more stable exposed in ambient air. Park and his colleagues reported that by partial substitution of FA with Cs in $FAPbI_3$ perovskite (i.e., $FA_{0.9}Cs_{0.1}PbI_3$), the photo and moisture stability as well as the PCEs of the PSCs were found to be substantially improved due to the enhanced interaction between FA and iodide and the reduced trap density.[72] Graetzel *et al.* reported PSCs with a mixture of MA, FA and Cesium cations that had an stabilized PCE of over 21% (18% after 250 hours under operational conditions).[30] It shows that the triple-cation perovskite compositions, are less depending on the fabrication conditions and thermally much more stable.

Table 2.2 The stability test of some representative PSCs.

Device structure	Initial PCE	Degradation percentage	Stability test condition	Test time (h)	Year	Ref.
mp-TiO_2/$MAPbI_3$-QDs/ liquid electrolyte/Pt	6.5%	~80%	Under continued irradiation	0.17	2011	[36]

mp-TiO_2/$MAPbI_3$/ spiro-MeOTAD/Au^k	~7%	Improved for about 14%	In air, RT, 100 mW/cm^2	500	2012	[3]
mp-TiO_2/$MAPbI_3$/ spiro-MeOTAD/Au^m	~9%	~20%	45 ºC, at maximum power point, 100 mW/cm^2	500	2013	[53]
mp-Al_2O_3/$MAPbI_3$/ spiro-MeOTAD/Au^m	~11%	~47%	40 ºC, at open-circuit condition, 76.5 mW/cm^2	1000	2013	[67]
mp-TiO_2/$MAPbI_3$/ PDPPDBTE/Au^k	~8.5%	Almost no degradation	In air, RT, H~20%	1000	2014	[68]
mp-TiO_2/ZrO_2/(5-AVA)$_x$$MA_{1-x}PbI_3$/C^k	~9.5%	Almost no degradation	In air, RT, 100 mW/cm^2	1008	2014	[69]
NiMgLiO/$MAPbI_3$/ PCBM/Ti(Nb)O_x/Ag^m	~14.6 % (large area)	~10%	In air, RT, at short-circuit condition, 100 mW/cm^2	1000	2015	[70]
NiO_x/$MAPbI_3$/ZnO/Al^k	~14.6 %	~10%	In air, RT, H = 30~50%	1440	2015	[71]

(^{m} Encapsulated, ^{k} without encapsulation, RT = room temperature, H = humidity).

Although some improvements have been achieved to the stability of PSCs, the lifetimes of the state-of-the-art PSCs are still far from the requirements of practical applications. Not only the intrinsic stability of organic-inorganic hybrid perovskite materials, but also the influence of charge transport layers and metal electrodes remain as the main research focus for long-term device stability. Only when stable perovskite material systems are well combined with optimized device architectures, PSCs with high PCEs and robust long-term stability can be achieved in the future.

2.7.2 Current-voltage Hysteresis

The current-voltage (*I-V*) hysteresis issue of the of PSCs was firstly reported by Snaith and his co-workers.[73] It refers to the large discrepancies among the *I-V* curves in different bias sweeping directions or scan rates.[74] The presence of *I-V* hysteresis hinders the determination of the accurate PCEs of perovskite solar cells

and the commercial application. Many researchers have devoted themselves to the study of the *I-V* hysteresis in PSCs. However, the origins of this phenomenon are still controversial. Now, some possible theories have been proposed to show the origins of *I-V* hysteresis, such as defect-trapping effect, ferroelectric effect and ion migration.[73, 75-78]

The perovskite films may have large defect density within or near the surface of the material.[73] These defects could act as charge traps in working devices. Huang *et al.* claimed that the trap states on the perovskite film surface and grain boundaries in the planar inverted solar cell is the origin of *I-V* hysteresis.[79] They found that the fullerenes coated on top of perovskite films can passivate the trap states and greatly reduce the *I-V* hysteresis, which seems to be a quite easy and effective way to reduce the *I-V* hysteresis.

Some researchers have proposed the ferroelectric effect as one possible origin for the *I-V* hysteresis.[73, 75, 78] It is believed that the inverse ferroelectric polarization field would reduce the net built-in electric field and interfere the charge separation. Miyasaka *et al.* demonstrated that the reverse bias poling (from -0.3 to -1.1 V) of $MAPbI_3$ perovskite layers before the *I-V* test will cause stronger hysteresis depending on the device structure.[78] It is believed the ferroelectric remnant polarization in the perovskite film can affect the photocurrent. Therefore, it is generally more obvious in PSCs with planar structure. However, a recent report by Wang and co-workers concluded that $MAPbI_3$ perovskite has no ferroelectric property at ambient conditions, according to polarization-electric field tests and observations by piezo-response force microscopy.[80]

Recently, ion migration has been considered as a more important reason for the *I-V* hysteresis behaviour. Huettner *et al.* investigated the iodine migration and the impact on hysteresis in planar PSCs ($FTO/TiO_2/MAPbI_{3-x}Cl_x$/Spiro-OMeTAD/Ag).[81] They indicated that the iodide

migration under applied bias voltage will shift down the work function of TiO_2 and shift up that of spiro-OMeTAD and lead to interfacial barriers, which is the origin of the hysteresis. Moehl *et al.* have investigated the origin of the hysteresis phenomenon with a combination of experimental and computational approaches.[76] The calculated activation energies for halide ion (or vacancy) migration match very well with the experimentally values involved in hysteresis, showing that the ion migration is the cause of the observed hysteresis behaviour in PSCs.

2.7.3 Toxicity of Raw Materials

Since most organic-inorganic hybrid PSCs are lead-based, there are lots of worries about the possible toxicity issues related with the lead content in terms of commercialization and real applications. It is believed that the organic-inorganic lead halide perovskites are likely to release into the outside environment after decomposition because they are not stable in environment with moisture or water, and. However, the amount of Pb diffusion to the environment was calculated to be far from catastrophic for the environment if the solar module fails to work. The reason is that the amount of lead halide perovskite material in the ultra-thin PSCs is quite small. Compared with other emission sources of Pb, such as fossil fuels and mines, the potential threat from PSCs is not as significant.

Due to the potential threat of the lead element in PSCs to the environment or human health, lead-free perovskites are considered a good solution for this problem. Another metal element tin (Sn), which is more environmental-friendly, has been proposed as an alternative to Pb. Actually, the lead-free $MASnBr_{3-x}I_x$ perovskite was already synthesized by Weber *et al.* early in the 1970s. Unfortunately, the PCEs of Sn-based PSCs (completely lead free) are much lower than the lead-based counterparts, with PCEs of only around 6%.[16, 82, 83] It is challenging to obtain high-quality full-covered Sn-based perovskite films because of the rapid

crystallization of Sn-based perovskite at room temperature. What's more, these Sn-based perovskites are not stable in ambient air since the Sn^{2+} in the films are prone to be oxidized into Sn^{4+} by oxygen in air, which is detrimental to device performance. More research is needed in order to find lead-free metal halide perovskites with higher photovoltaic performance and better stability.

2.8 Summary and Perspectives

In summary, the inorganic-organic metal halide PSCs have experienced a rapid development in the past decade and have revolutionized the prospects of next-generation photovoltaics. They turned a new leaf in solar cell research due to their high PCEs, easy processing and low material and fabrication costs. The organic-inorganic hybrid perovskites have shown great potential for a variety of optoelectronic applications not just for photovoltaic devices. In the past decade, a lot of efforts have been devoted to produce high quality perovskites and devices with great performances. Based on the fast development in the device performance of perovskite solar cells, further advancements will be promoted by some more fundamental investigations. It is of great importance to have a deeper understand about the fundamental properties related to the hybrid perovskite materials.

Despite of great developing speed, the inorganic-organic hybrid perovskite solar cells are still in its early stages of lab research. In order to meet the requirements of mass production in the future, the PSCs must have a substantially higher solar module performance with much lower manufacturing costs than the other existing solar technologies. Thus, there is still much room for improvement. Also, some challenging issues, like large-area module, reproducibility, long-term stability, I-V hysteresis and toxicity of lead, should be carefully addressed through much more research before their real application.

Chapter 3 Efficient Semitransparent Perovskite Solar Cells with Graphene Electrodes

3.1 Introduction

Solar cells based on methylammonium lead halide and mixed halides $CH_3NH_3PbX_3$ (X = Cl, Br, I) with the perovskite structure have attracted much attention in recent years due to their high PCEs, easy fabrication and low cost.[8, 84] The semiconducting perovskite materials have shown high light absorption coefficient, direct band gap, high carrier mobility, and long carrier diffusion length.[3, 20, 21] Since the first report of the material used in solar cells in 2009,[2] tremendous progress in the performance of perovskite solar cells has been achieved.[44-46, 51, 53] To date, the PCEs of perovskite solar cells have been reported to be over 22%,[4] approaching the efficiencies of commercialized Si solar cells, while their fabrication cost is expected to be much lower than that of the Si-based counterparts.

Recently, perovskite solar cells have been investigated for their potential in making transparent or semitransparent devices that can absorb light from both sides. Those devices are promising for some special applications such as photovoltaic curtains, building-integrated photovoltaics, wearable electronics and tandem

cells.[85-91] Eperon *et al* reported the neutral color semitransparent perovskite solar cells based on perovskite "islands", which do not fully cover the devices in microscale, and Au transparent electrodes.[85, 86] However, the PCEs of the devices (~6%) are much lower than that of a typical perovskite solar cell. Roldán-Carmona *et al* prepared semitransparent perovskite solar cells by thermal evaporating perovskite layers and thin Au electrodes and obtained the PCEs of ~7%.[87] It is notable that a thin Au film is not an ideal transparent electrode for a perovskite solar cell due to its low transparency and high cost. Recently, Bailie *et al* prepared semitransparent perovskite solar cells with transparent Ag nanowire electrodes and placed them on copper indium gallium diselenide and polycrystalline silicon to realize tandem solar cells.[91] However, Ag-based transparent electrodes are not very stable on perovskite solar cells due to the formation of Ag halide that degrades the device performance.[88] Bryant *et al* fabricated semitransparent devices with Ni mesh top electrodes and fluorine-doped tin oxide (FTO) bottom electrodes, which showed average PCEs of 13.3% when the devices were illuminated from FTO side and 9.8% from Ni mesh side.[89] Moreover, carbon nanotubes (CNTs) have been successfully used as top electrodes of semitransparent perovskite solar cells and showed the PCEs up to 9.9% and 5.6% when the devices were illuminated from FTO side and carbon nanotube side, respectively.[90] Therefore, transparent top electrodes are critical to the performance of semitransparent solar cells.

An ideal transparent electrode must have high transparency, low sheet resistance, robust chemical stability, low cost and effective charge collecting ability. Within the widely used conductive materials including graphene,[92-95] CNTs,[96, 97] conductive polymers,[98, 99] and metallic nanowires,[100, 101] graphene is probably one of the best candidates for transparent electrodes in solar cells due to its high transparency, high conductivity and smooth surface. In particular, graphene has shown many advantages over indium tin oxide (ITO), FTO and rare metals in terms of mechanical and chemical robustness, excellent electrical and optical properties, and potentially low cost.[93, 102] However, the applications of graphene transparent electrodes in perovskite solar cells have never been reported until now although graphene-based nanomaterials have been successfully used in perovskite solar cells as interlayers for effective charge transfer or collecting.[103, 104]

3.2 Devices Fabrication and Characterization

Device Design

Semitransparent perovskite solar cells with the structure of glass/FTO/TiO_2/$CH_3NH_3PbI_{3-x}Cl_x$/Spiro-OMeTAD/PEDOT:PSS/graphene/PMMA/PDMS were fabricated by a lamination process. Two parts of the devices (glass/FTO/TiO_2/$CH_3NH_3PbI_{3-x}Cl_x$/Spiro-OMeTAD and PEDOT:PSS/graphene/PMMA/PDMS) were fabricated separately and then laminated together under pressure.

Graphene Top Electrodes

Graphene was synthesized on copper foils by CVD method. The Raman spectrum of the synthesized graphene film confirms that the film is mainly single-layer graphene. Poly(methyl methacrylate) (PMMA) solution with the solvent of anisole (25 mg/ml) was spin-coated on the CVD graphene and resulted in a thin layer (100 nm) of PMMA. Then the sample was annealed at 90ºC for 30 min followed by the lamination of a thin layer of freestanding PDMS film (about 0.2 mm thick) on top of PMMA. After that, the sample was immersed in an iron chloride aqueous solution for several hours to etch the Cu foil. The graphene/PMMA/PDMS multilayer film was washed twice in distilled (DI) -water and was then transferred to a glass substrate with graphene side upward. After a O_2 plasma treatment on graphene for 10 s at low power mode, PEDOT:PSS (PH500) solution doped with 1% fluorosurfactant Zonyl-FS300 (Zonyl) together with different amount of D-sorbitol (0 wt% ~ 20 wt%) was spin-coated on graphene/PMMA/PDMS/glass substrate at 3000 rpm for 30 s. Finally, the graphene electrode with PEDOT:PSS film was annealed at 120ºC for 60 min in a glovebox.

To produce multilayer graphene electrodes, the graphene/PMMA film was stacked onto another graphene film on a Cu foil followed by etching the Cu foil in an iron chloride solution. The stacking process was repeated for several times to get the required number of graphene layers. In the end, PEDOT:PSS layer was coated on the multi-layer graphene/PMMA/PDMS film for lamination process.

Device Fabrication

The semitransparent devices were fabricated on fluorine-doped tin oxide (FTO)-coated glass with the sheet resistance of 14 Ω/□. Initially, FTO electrodes were patterned by etching FTO with 2 M HCl and zinc powder. Substrates were then cleaned sequentially in acetone, DI-water, and ethanol. After an O_2 plasma treatment,

a 20 nm thick ETL of compact TiO_2 was deposited by spin-coating an acidic solution of titanium isopropoxide in ethanol (350 μL titanium isopropoxide in 5 ml of ethanol with an addition of 50 μL HCl of 37 wt %) at 5000 rpm and annealed at 500ºC for 60 min.

The perovskite layers were then deposited on the TiO_2 layer by spin-coating a mixed precursor solution of methylammonium iodide and lead chlorine (3:1 molar ratio, final concentrations 0.88 M lead chloride and 2.64 M methylammonium iodide) in N, N-dimethylformamide (DMF). The films were annealed at 100ºC for 45 min in the glovebox. The hole-transporting layer was then deposited by spin-coating a layer of 2,2',7,7'-tetrakis-(N,N-di-p-methoxypheny lamine)-9,9-spirobifluorene (spiro-OMeTAD). The thickness of the spiro-OMeTAD layer was controlled by the concentration of spiro-OMeTAD in chlorobenzene. For the optimum fabrication condition, 70mg/ml spiro-OMeTAD solution in chlorobenzene with additives of 25ul/ml bis(trifluoro- methanesulfonyl)imide solution (520 mg/ml, dissolved in acetonitrile) and 36ul/ml 4-tert-butylpyridine was used. Spin-coating process was carried out in the glovebox at 5000 rpm and the sample is then placed in dry air (humidity<10%) overnight.

After the two parts of the devices were fabricated, the graphene electrodes were laminated on the spiro-OMeTAD surface to obtain final devices. Both parts were heated at 65ºC, and then a Teflon rod was rolled with proper pressure on the PDMS film to remove air bubbles at the interface between PEDOT:PSS and spiro-OMeTAD.

Measurement and Characterization

The sheet resistance of graphene film was characterized with a four-probe test system. The transmittance spectra of graphene films were measured by using a UV-Vis spectrophotometer (UV-2550, Shimadzu, Japan). The J-V characteristics of

the perovskite solar cells were measured by using a Keithley 2400 source meter under illumination of 100 mW/cm^2 (Newport 91160, 300W, solar simulator equipped with an AM 1.5 filter). The light intensity was calibrated with a standard silicon solar cell. The solar cells were scanned from forward bias to short-circuit at a scan rate of 0.038 V/s. The external quantum efficiencies (EQEs) of the devices were measured with a standard system equipped with a xenon lamp (Oriel 66902, 300 W), a Si detector (Oriel 76175_71580) for calibration, a monochrometor (Newport 66902), and a dual channel power meter (Newport 2931_C) in the wavelength region from 300nm to 800nm.

3.3 Results and Discussion

Figure 3.1a and **3.1b** show the device structure of a perovskite solar cell with a graphene top electrode and the corresponding energy band diagram,[46, 95] respectively. The device was fabricated on an etched FTO-coated glass substrate and had the active area of about 4mm×6mm, which is bigger than the areas of solar cells with graphene electrodes reported by other groups.[105] A compact TiO_2 layer was firstly spin-coated on the substrate as an electron transport layer (ETL), followed by the deposition of $CH_3NH_3PbI_{3-x}Cl_x$ perovskite layer (~350nm thick) with a one-step route.[45] Full-coverage perovskite film was achieved on the substrate at this condition (See **Figure 3.1c**). The X-ray diffraction (XRD) patterns also demonstrate the good crystallinity of the perovskite film (See **Figure 3.1d**). A layer of continuous (2,2',7,7'-tetrakis-(N,N-di-p-methoxyphenylamine)-9,9'-spirobifluorene) (spiro-OMeTAD) was then spin-coated on top of the perovskite film as a hole transport layer (HTL) as well as an electron blocking layer.

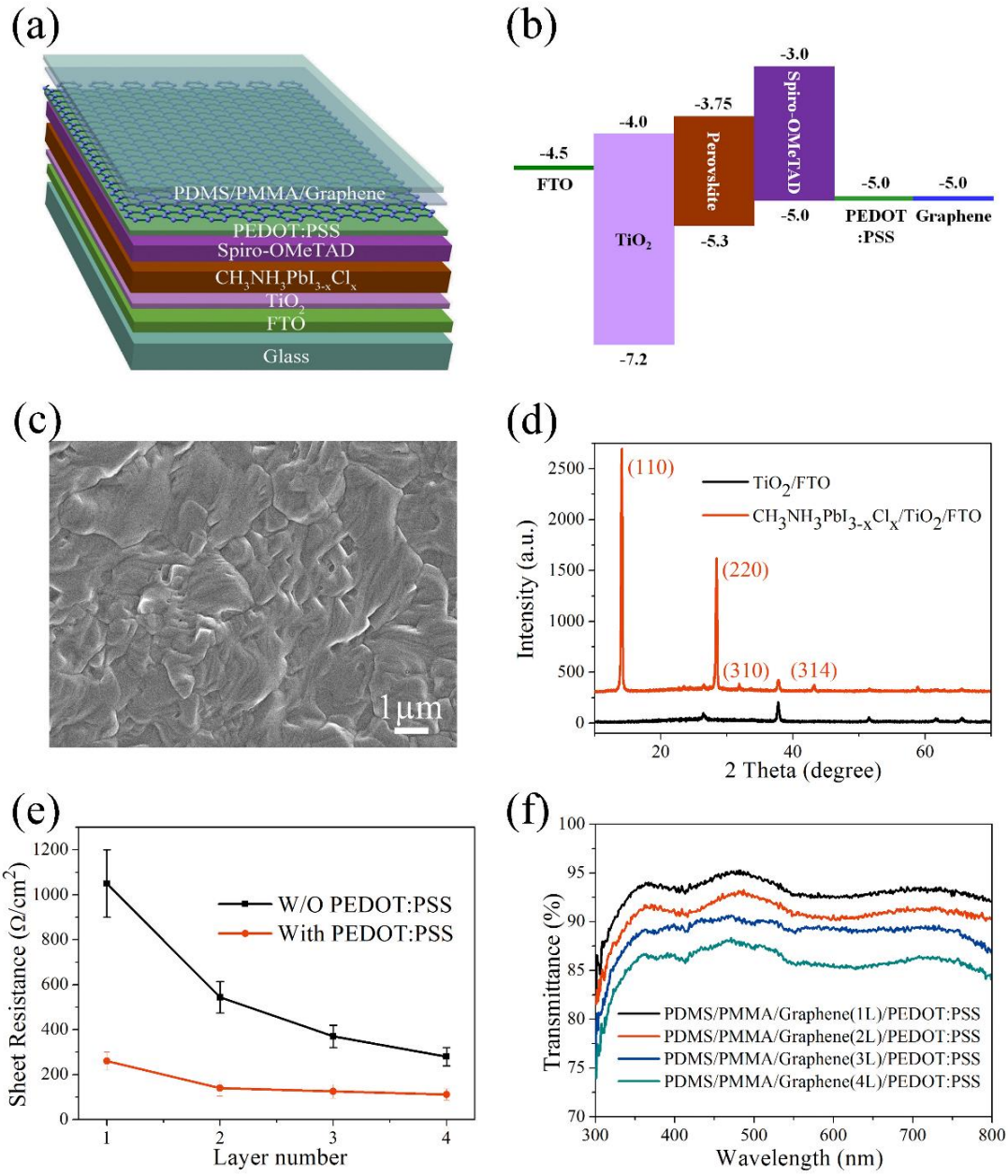

Figure 3.1 (a) Schematic diagram of a semitransparent perovskite solar cell. (b) Band structure of the device. (c) and (d) SEM image and X-Ray diffraction (XRD) pattern of a $CH_3NH_3PbI_{3-x}Cl_x$ perovskite film on a TiO_2/FTO/Glass substrate. (e) Sheet resistance of one to four layers of stacked graphene films before and after PEDOT:PSS doping. (f) UV-Vis transmittance spectra of PEDOT:PSS doped transparent graphene electrodes with one to four layers of stacked graphene.

In the preparation of graphene electrodes, single-layer CVD graphene grown on a copper foil was coated with a thin layer of poly(methylmethacrylate) (PMMA) and

transferred onto a substrate with the conventional approach.[95] Then a thin poly(dimethylsiloxane) (PDMS) film with a thickness of about 0.2 mm was attached to the PMMA film to act as a supporting layer that is mechanically strong and freestanding. The PDMS/PMMA/graphene film can be easily peeled off from the substrate by using tweezers and laminated onto a solar cell. An intrinsic single-layer graphene film normally has the sheet resistance of ~1050±150 Ω/□, which is too high for the application as transparent electrodes of solar cells. To improve the conductivity of the graphene film, a thin layer of poly(3,4-ethylenedioxythiophene):poly(styrene sulfonic acid) (PEDOT:PSS) film was spin-coated on the graphene surface. Here, 1 wt% of Zonyl FS-300 was introduced in the PEDOT:PSS aqueous solution as a surfactant to realize a much lower contact angle and uniform coating on the hydrophobic surface of graphene (See **Figure 3.2**). The Fermi level in PEDOT:PSS is about 5.0 eV, which is much higher than the Dirac point of graphene (4.6 eV).[95] So a thin layer of PEDOT:PSS can introduce more holes in the graphene film by electrostatic doping and dramatically improve the conductivity of the graphene film. On the other hand, the Fermi level in the doped graphene was found to be changed to ~5.0 eV as reported in our previous work.[95] As shown in **Figure 3.1e**, the sheet resistance was decreased to about 260±40 Ω/□ due to the doping effect of the PEDOT:PSS layer.

To obtain graphene electrodes with lower sheet resistance, multilayer graphene films were prepared by layer-by-layer stacking method.[105] Single and double layer graphene films transferred on flat silicon wafers were characterized under atomic force microscopy (AFM) and showed the thickness of 0.81 nm and 1.45nm, respectively (See **Figure 3.3**). As shown in **Figure 3.1e**, the sheet resistance of a graphene film decreases with increasing number of layers. A PEDOT:PSS layer coated on the surface can decrease the sheet resistance of multilayer graphene at any layer number while has little influence on the transmittance of the graphene because

of the high transparency of the thin PEDOT:PSS layer (thickness: ~20nm). It is notable that two-layer graphene doped with PEDOT:PSS has a sheet resistance of 140±35 Ω/□ and a transmittance higher than 90% in the visible region, as shown in Figure 1f. For more layers of graphene, the sheet resistance was further decreased while the transmittance was below 90%. Here, the sheet resistances were characterized in the dark. When the graphene films are used as electrodes of solar cells, their sheet resistances can be further decreased under light illumination due to the increased carrier densities in the graphene layers.[106]

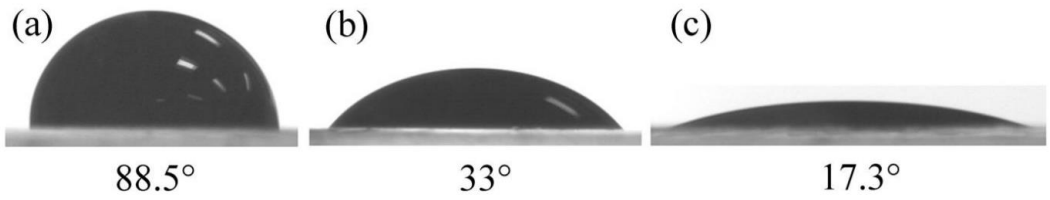

Figure 3.2 The contact angles of PEDOT:PSS aqueous solution on graphene films. (a) Pristine PEDOT:PSS solution. (b) PEDOT:PSS solution added with 1% Zonyl FS-300. (c) PEDOT:PSS with 1% Zonyl FS-300 on a graphene film treated by plasma for 10 seconds.

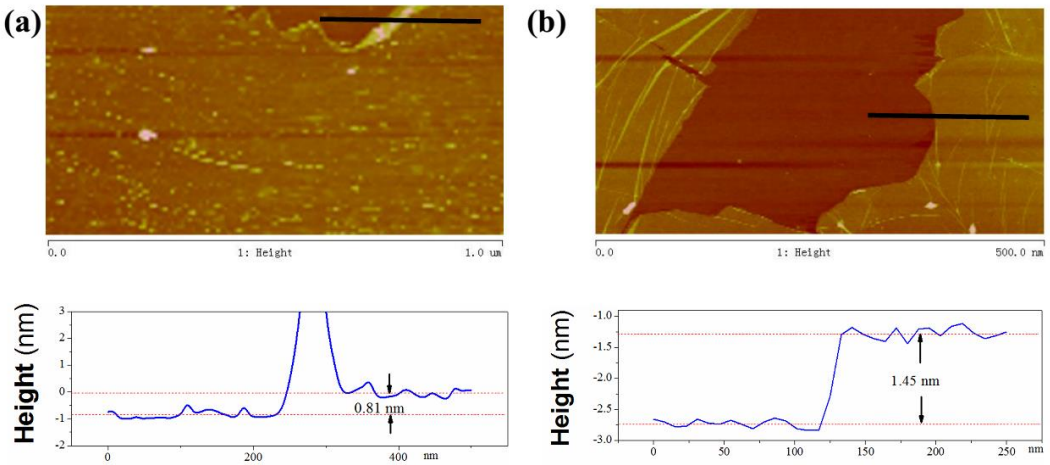

Figure 3.3 AFM images of (a) single layer graphene and (b) stacked double-layer graphene films with steps to show the thicknesses of the films.

Besides the doping effect on the graphene electrodes, PEDOT:PSS is also used as the adhesion layer in the lamination process of the graphene electrodes on top of

the perovskite active layers. PEDOT:PSS is in direct contact with the HTL (spiro-OMeTAD) by Van der Waals forces. Moreover, PEDOT:PSS is also an excellent material for hole transporting and electron blocking in solar cells.[95] In order to obtain a better contact at the interface both electronically and mechanically, D-sorbitol was introduced in the PEDOT:PSS film to increase the adhesiveness of the PEDOT:PSS film.[106] We noticed that the addition of D-sorbitol in PEDOT:PSS could dramatically improve the performance of the perovskite solar cells due to the improved contact at the interface of PEDOT:PSS and spiro-OMeTAD.

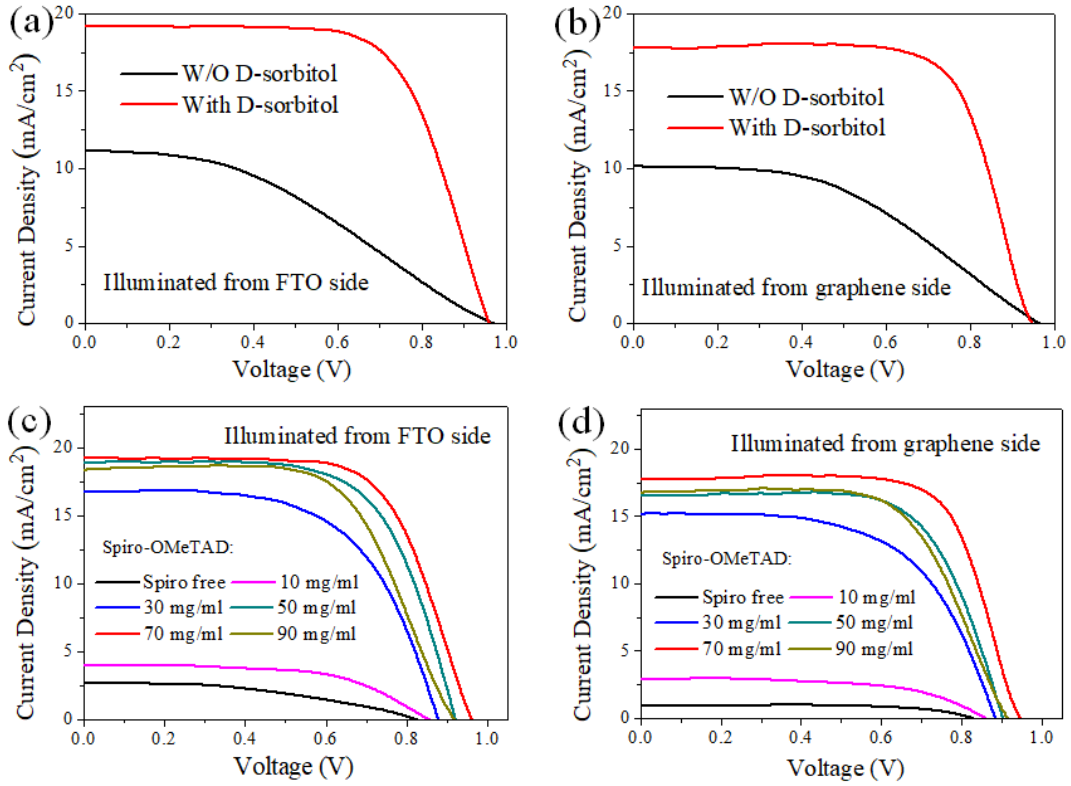

Figure 3.4 *J-V* characteristics of perovskite solar cells with or without D-sorbitol in PEDOT:PSS illuminated from (a) FTO side and (b) graphene side. *J-V* characteristics of solar cells coated with spiro-OMeTAD solutions with different concentrations illuminated from (c) FTO side and (d) graphene side.

Figure 3.4a and **3.4b** show the current density-voltage (*J-V*) characteristics of perovskite solar cells with laminated graphene electrodes (2-layer graphene was used

here). The device without the introduction of D-sorbitol has a short-circuit current density (J_{sc}) of 11.30 (10.17) mA/cm^2, an open-circuit voltage (V_{oc}) of 0.97 (0.965) V, a fill factor (FF) of 37.7 (44.5) % and a PCE of 4.13 (4.37)% when light is illuminated from the FTO (graphene) side. The bracketed data are for the device illuminated from the graphene side. The low J_{sc} and FF of the device are attributed to the poor contact at the interface between spiro-OMeTAD and PEDOT:PSS, which increases the overall series resistance (R_s) of the solar cell. In contrast, the devices with PEDOT:PSS and D-sorbitol mixture films exhibit much better overall performance when they are illuminated from both sides, as shown in **Figure 3.4a** and **3.4b**, indicating that PEDOT:PSS/D-sorbitol is an excellent electronic glue that can be used in various laminated electronics devices.[107] The optimum concentration of D-sorbitol added to PEDOT:PSS aqueous solution is about 150 mg/ml (See **Table 3.1**), which lead to J_{sc} of 19.17 (17.66) mA/cm^2, V_{oc} of 0.960 (0.945) V, FF of 67.22 (71.72) % and PCE of 12.37 (12.03) % under the light illumination from FTO (graphene) side. It is notable that both the fill factor and the short circuit current are dramatically improved by the introduction of D-sorbitol. However, too much D-sorbitol added in PEDOT:PSS may influence the hole transport property of PEDOT:PSS and reversely degrade the device performance. In addition, a control device with a top electrode made of PEDOT:PSS/D-sorbitol only shows PCEs of 3.84% and 3.43% measured from FTO and PEDOT:PSS sides, respectively, due to the high sheet resistance of the PEDOT:PSS film (~1 kΩ/□), as shown in **Figure 3.5**, indicating that the graphene film plays a key role in the top electrode.

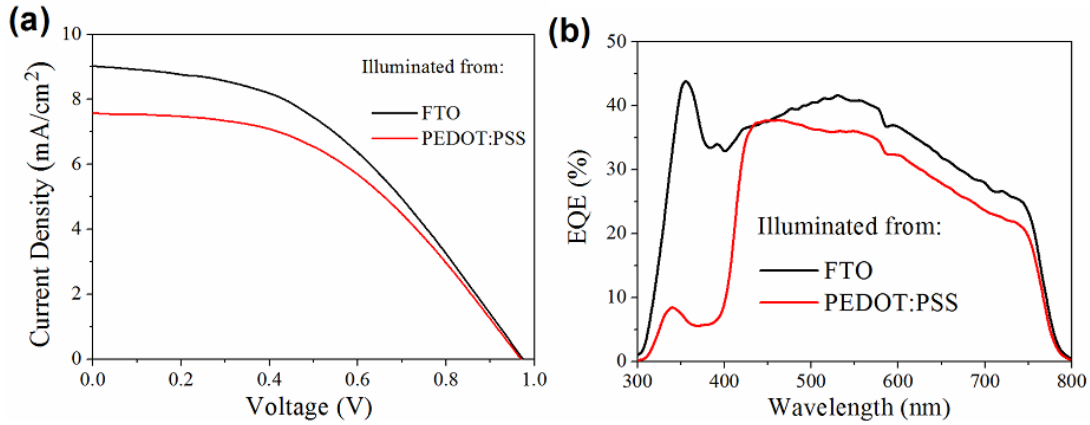

Figure 3.5 (a) *J-V* characteristics of a perovskite solar cell with a PEDOT:PSS/D-sorbitol top electrode illuminated from FTO side and PEDOT:PSS side. (b) EQEs of the perovskite solar cell illuminated from FTO side and PEDOT:PSS side.

Table 3.1 Photovoltaic parameters of the semitransparent perovskite solar cells prepared with different concentrations of D-sorbitol added in PEDOT:PSS solutions.

D-sorbitol	Illumination side	V_{oc} (V)	J_{sc} (mA/cm^2)	FF (%)	PCE (%)	Average PCE (%)
0 mg/ml	FTO	0.97	11.17	37.66	4.08	3.95±0.23
	Graphene	0.965	10.13	44.60	4.36	4.10±0.20
50 mg/ml	FTO	0.965	17.20	43.98	7.30	7.01±0.28
	Graphene	0.95	15.62	54.72	8.12	7.58±0.45
100 mg/ml	FTO	0.95	18.76	61.72	11.00	10.63±0.52
	Graphene	0.93	16.13	64.13	9.62	9.27±0.44
150 mg/ml	FTO	0.96	19.17	67.22	12.37	12.02±0.32
	Graphene	0.945	17.75	71.72	12.03	11.65±0.35
150 mg/ml (Without Graphene)	FTO	0.98	9.03	43.39	3.84	3.50±0.31
	PEDOT:PSS	0.97	7.58	46.51	3.42	3.02±0.53
200 mg/ml	FTO	0.95	18.01	58.91	10.08	9.83±0.32
	Graphene	0.94	16.35	62.98	9.68	9.36 ±0.37

Average PCE is the average value of more than 6 devices.

To form a good contact at the interface between Spiro-OMeTAD and PEDOT:PSS, the surfaces of the films should be as smooth as possible. The surface of a thin PEDOT:PSS film spin-coated on a flat CVD graphene film shows a low roughness (See **Figure 3.6**). The root mean square (RMS) value of the

PEDOT:PSS/graphene surface characterized by atomic force microscopy (AFM) is only 2.24 nm, which is far less than that of a transparent electrode made of metal networks or carbon nanotubes.[96, 100] On the other hand, the surface morphology of the spiro-OMeTAD films coated on perovskite layers was also characterized by using AFM (See **Figure 3.7**). We find that the surface roughness is related to the concentration of the spiro-OMeTAD solution. The perovskite film without spiro-OMeTAD has the largest roughness of about 68.3 nm due to the crystallization of the $CH_3NH_3PbI_{3-x}Cl_x$ film. Once the spiro-OMeTAD film was coated on the perovskite film, the surface roughness can be decreased dramatically. The optimum concentration of spiro-OMeTAD solution is ~70 mg/ml, which lead to the lowest surface roughness (~29.3 nm). The morphological changes of these films coated with different concentrations of spiro-OMeTAD can also be verified by SEM images shown in **Figure 3.8**.

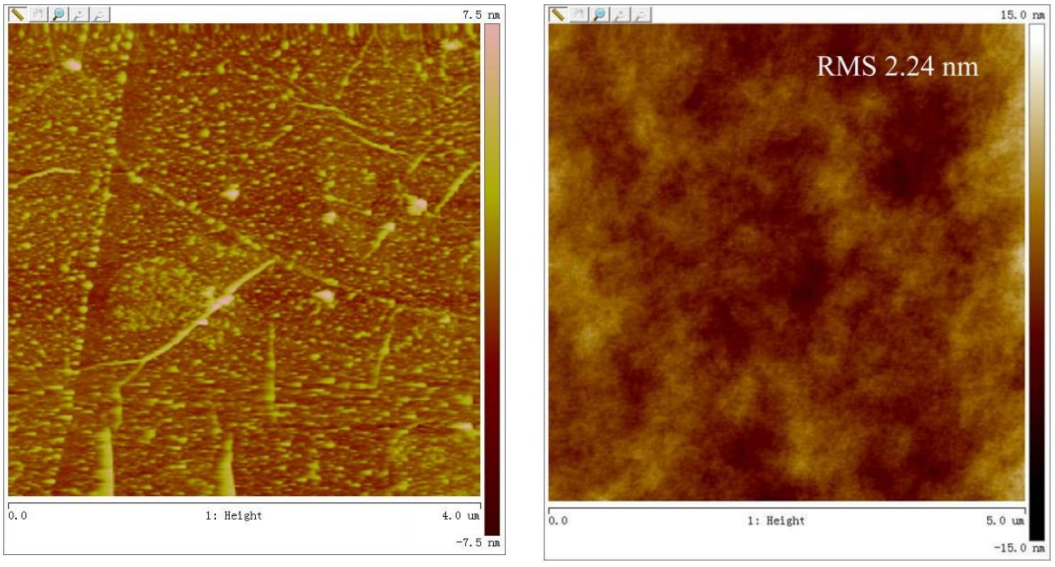

Figure 3.6 AFM image of a stacked 2-layer graphene film (left, roughness (RMS): 1.15 nm) and a PEDOT:PSS/graphene (2-Layer) film (right, roughness (RMS): 2.24 nm).

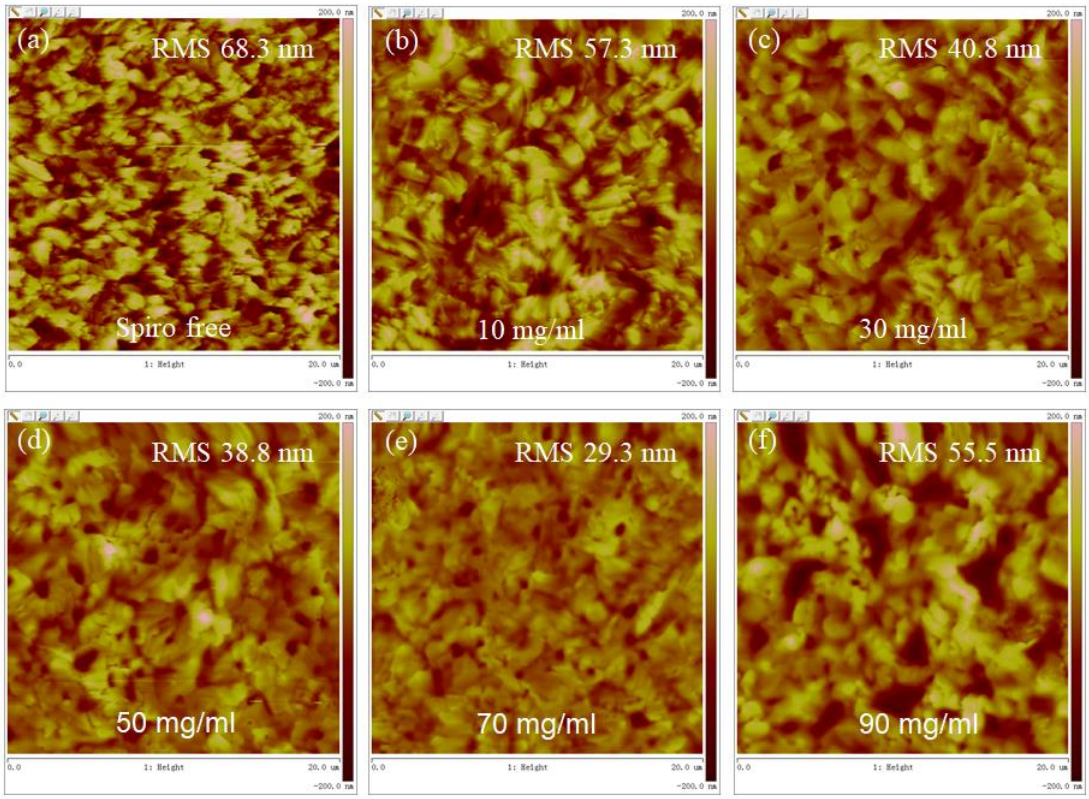

Figure 3.7 AFM images showing the morphologies of perovskite films coated with varying concentrations of Spiro-OMeTAD solutions. The corresponding surface roughness (RMS) for different concentration is shown in each figure.

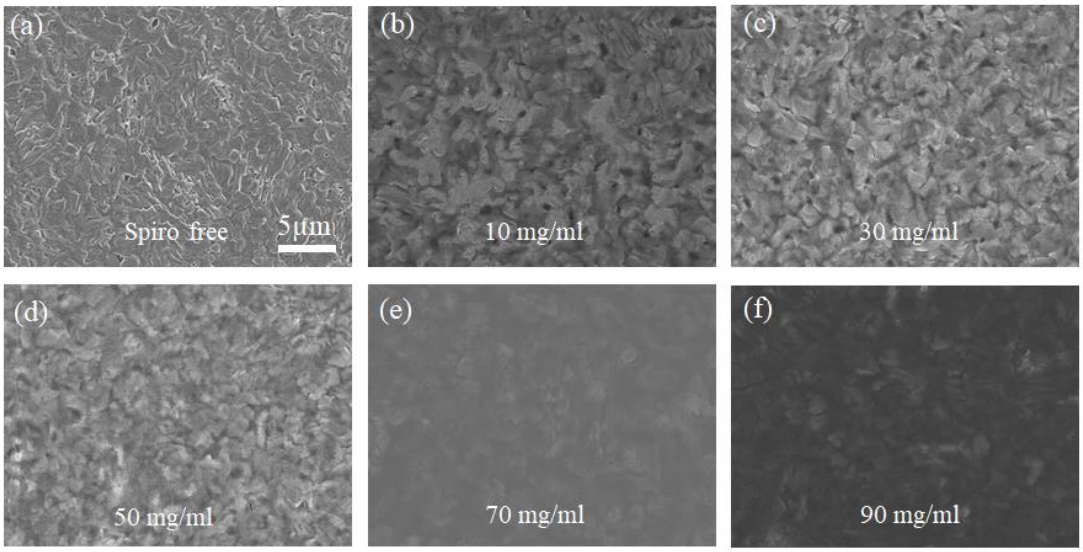

Figure 3.8 SEM images showing the morphologies of perovskite films coated with varying concentrations of Spiro-OMeTAD solutions.

Table 3.2 Photovoltaic parameters of the semitransparent perovskite solar cells fabricated with different concentrations of Spiro-OMeTAD solutions.

Spiro-OMeTAD	Illumination side	V_{oc} (V)	J_{sc} (mA/cm^2)	FF (%)	PCE (%)	Average PCE (%)
Spiro free	FTO	0.82	2.69	42.61	0.94	0.80±0.15
	Graphene	0.83	0.99	63.28	0.52	0.32±0.30
10 mg/ml	FTO	0.85	3.91	59.58	1.98	1.62±0.35
	Graphene	0.86	2.91	58.74	1.47	1.05±0.36
30 mg/ml	FTO	0.88	16.72	59.88	8.81	8.40±0.35
	Graphene	0.88	15.17	60.00	8.01	7.45±0.52
50 mg/ml	FTO	0.92	18.85	65.91	11.43	10.99±0.37
	Graphene	0.90	16.52	68.00	10.11	9.72±0.41
70 mg/ml	FTO	0.96	19.17	67.22	12.37	12.02±0.32
	Graphene	0.945	17.75	71.72	12.03	11.65±0.35
90 mg/ml	FTO	0.92	18.32	63.19	10.65	10.02±0.54
	Graphene	0.915	16.77	64.52	9.90	9.70±0.36

Average PCE is the average value of more than 6 devices.

The *J-V* characteristics of the perovskite solar cells with spiro-OMeTAD films made from the solutions with different concentrations are demonstrated in **Figure 3.2c** and **3.2d**. Here, 2-layer graphene was used in the devices. When the graphene/PEDOT:PSS electrode was directly laminated to the perovskite film without spiro-OMeTAD film, the solar cell shows PCEs of only 0.935 (0.52)% when it is illuminated from FTO (graphene) side (See **Table 3.2**). The PCEs of the perovskite solar cells increase gradually with the increasing concentration of spiro-OMeTAD solution from 10 mg/ml to 70 mg/ml, which can be mainly attributed to the increasing FF and *Jsc*. However, when the concentration of spiro-OMeTAD solution is higher than 70 mg/ml the performance decreases with the increase of the spiro-OMeTAD concentration. So the optimized spiro-OMeTAD concentration is ~70 mg/ml, which leads to the highest PCE of the devices. It is notable that, at this concentration, the spiro-OMeTAD film shows the lowest surface roughness. Therefore, lower surface roughness of both the spiro-OMeTAD and the

PEDOT:PSS surfaces can offer a better contact during the lamination and thus better performance of the solar cell.

Next, the effect of the number of layers of graphene electrodes were characterized in perovskite solar cells prepared under the optimized conditions obtained above. **Figure 3.9** shows the performance of the perovskite solar cells with 1 to 4 stacked layers of graphene electrodes. The photovoltaic parameters of the devices with graphene electrodes of different layers and a control device with an Au top electrode are shown in **Table 3.3**. The device with a single-layer graphene exhibits the lowest *Voc*, *FF* and *PCE* due to the relatively high sheet resistance of the graphene electrode. The device with a 2-layer graphene electrode gives an improved *Jsc* and *PCE* due to higher conductivity of the graphene electrode. However, for the devices with 3 or 4 layers of graphene, the device performance is reversely degraded although the conductivity of the graphene electrode is increased. We noticed that the multilayer graphene electrodes showed increased surface roughness with the increase of the number of layers due to some wrinkles of each layer of graphene. So multilayer graphene shows worse contact with the spiro-OMeTAD layer, which is probably the main reason for the degraded performance with the increasing number of layers of graphene. Moreover, the fact that more layers of graphene show lower transmittance should be another reason for the decreased performance with the increasing number of layers of graphene when the devices are illuminated from the graphene side. Therefore, the device with a 2-layer graphene electrode exhibits the highest average *PCE* of 12.37(12.03)% when it is illuminated from FTO (graphene) side. The average efficiencies of 6 devices prepared at the optimum conditions are 12.02% and 11.65% when they are illuminated from the FTO and graphene sides, respectively.

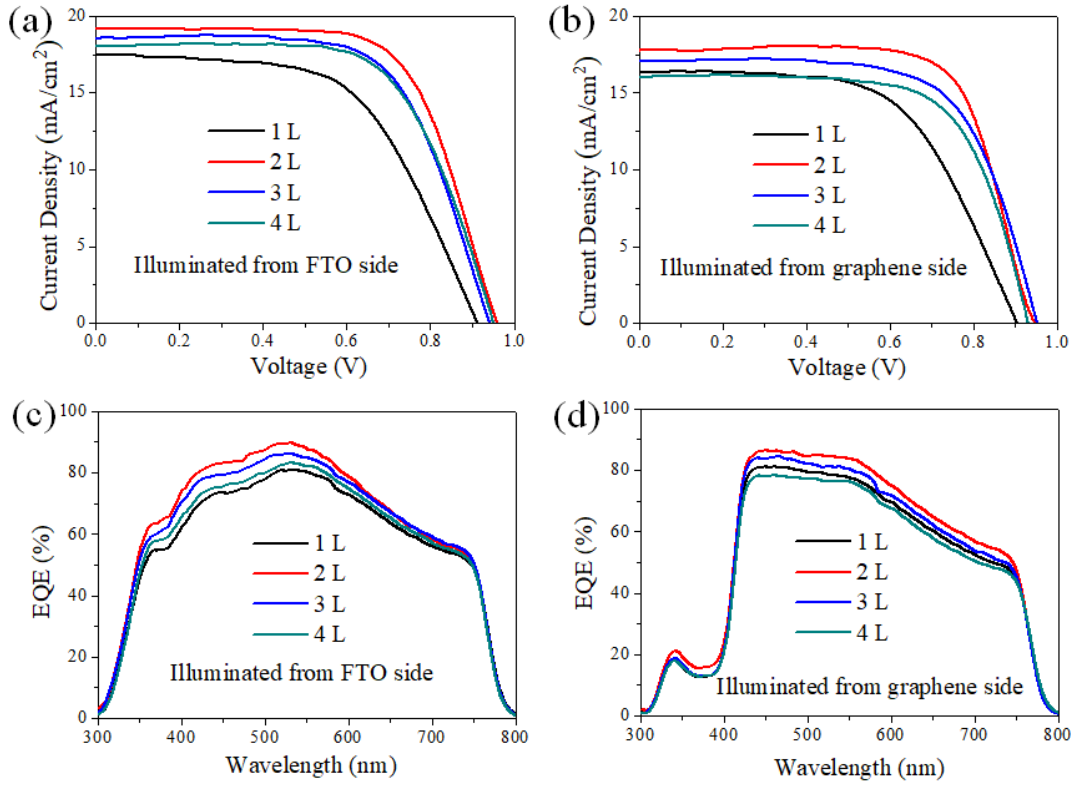

Figure 3.9 *J-V* characteristics of perovskite solar cells with 1 to 4 layers of graphene electrodes illnuminated from (a) FTO side and (b) graphene side. EQEs of the perovskite solar cells illuminated from (c) FTO side and (d) graphene side.

Table 3.3 Photovoltaic parameters of the semitransparent perovskite solar cells with graphene (1 ~ 4 layers) top electrodes and control devices with Au top electrodes.

Top electrode	Illumination side	V_{OC} (V)	J_{SC} (mA/cm^2)	FF (%)	PCE (%)	Average PCE (%)
Au	FTO	0.985	19.80	73.58	14.35	13.62±1.00
Graphene (1L)	FTO	0.910	17.46	57. 8	9.18	8.65±0.45
	Graphene	0.905	16.35	59.07	8.74	8.38±0.43
Graphene (2L)	FTO	0.960	19.17	67.22	12.37	12.02±0.32
	Graphene	0.945	17.75	71.72	12.03	11.65±0.35
Graphene (3L)	FTO	0.940	18.54	65.70	11.45	10.95±0.46
	Graphene	0.950	17.04	67.58	10.94	10.37±0.52
Graphene (4L)	FTO	0.950	18.05	65.72	11.27	10.68±0.57
	Graphene	0.930	16.01	68.37	10.18	9.27±0.83

Average PCE is the average value of more than 6 devices.

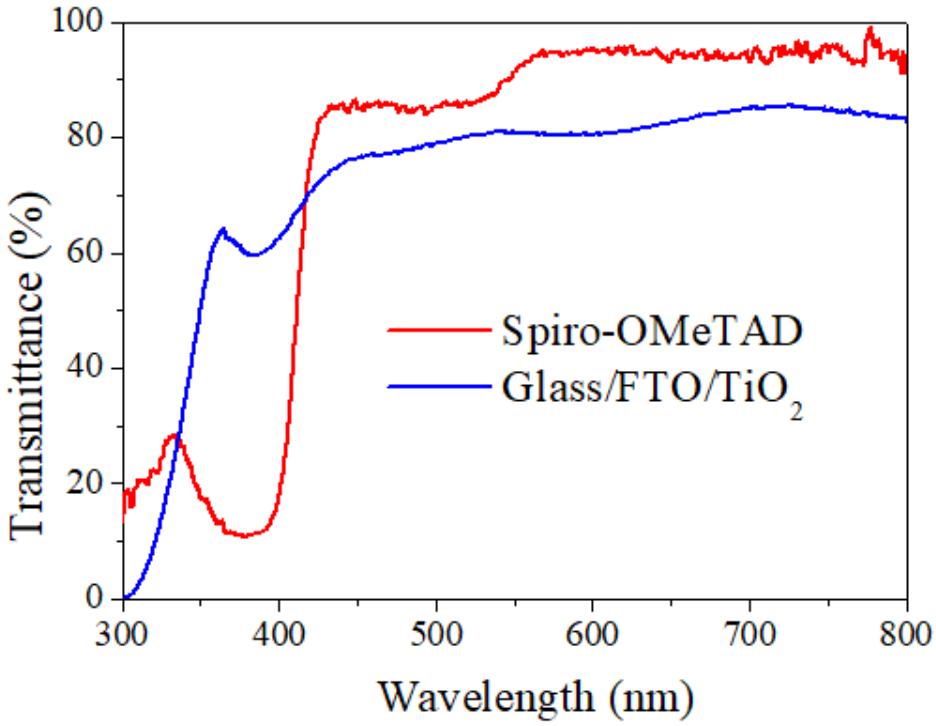

Figure 3.10 UV-Vis transmittance spectra of a Spiro-OMeTAD film and a Glass/FTO/TiO_2 substrate.

Figure 3.9c and **3.9d** show the EQEs of the solar cells with different number of layers of graphene measured in the wavelength region between 300 nm and 800nm. The device with 2-layer graphene shows the highest EQE at any wavelength, which is consistent with the highest short circuit current J_{SC} of the device shown in **Figure 3.8a** and **3.8b**. The ~800 nm cut-off wavelength corresponds to the 1.55 eV band gap of the $CH_3NH_3PbI_{3-x}Cl_x$ perovskite active layer. At shorter wavelengths, the photocurrent is cut off by the light absorption of ETL (TiO_2) or HTL (spiro-OMeTAD) (See **Figure 3.10**). The device shows high EQEs of above 80% in the wavelength region from 400 to 600 nm and lower values in the longer wavelength region. It is notable that the EQEs for the illumination from FTO and graphene sides are quite different. The major difference lies in the wavelength region from 330 nm to 430 nm, where the EQE value from graphene side is much lower than that from FTO side, due to the strong light absorption of spiro-OMeTAD film in

this wavelength region. Therefore, the device shows lower efficiency from graphene side than from FTO side although the transmittance of graphene electrodes is better than that of FTO in the visible region.

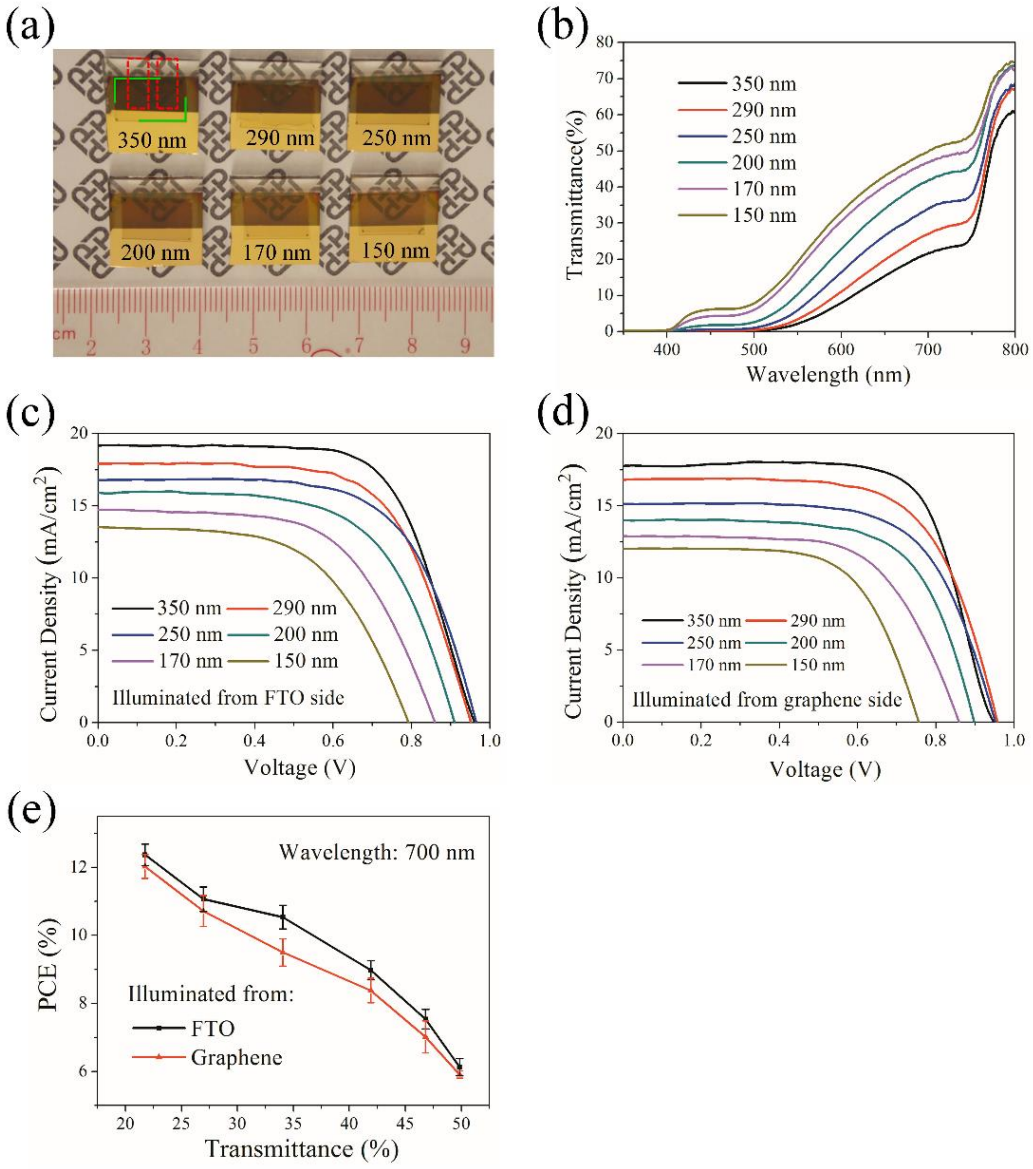

Figure 3.11 (a) Photos of semitransparent perovskite solar cells with transparent graphene electrodes. The thicknesses of the perovskite layers in the six devices are approximately 350 nm, 290 nm, 200 nm, 170 nm and 150 nm, respectively. (b) Transmittance spectra of the above devices. *J-V* characteristics of the semitransparent solar cells illuminated from (c) FTO side and (d) graphene side. (e) The average PCEs of the semitransparent perovskite solar cells as a function of the transmittance at the wavelength of 700 nm.

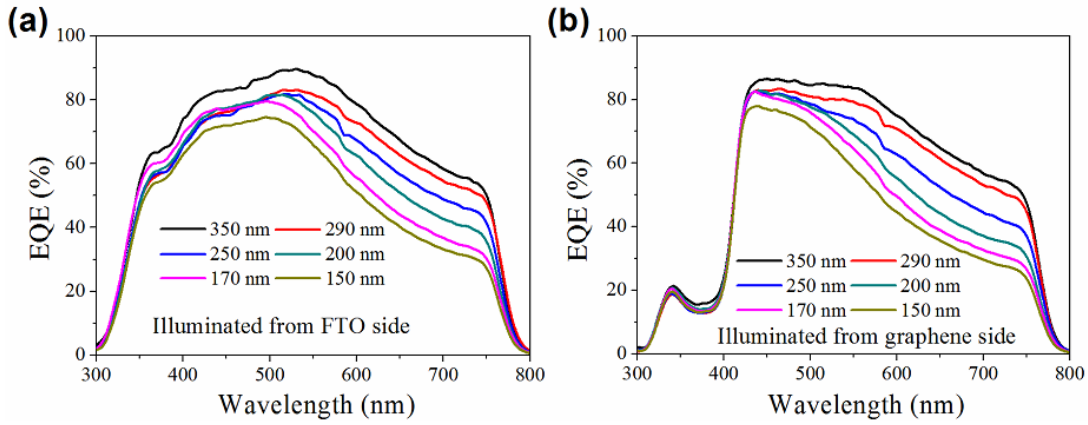

Figure 3.12 EQEs of the semitransparent solar cells with different perovskite layer thicknesses illuminated from (a) FTO side and (b) graphene side.

The transparency of the above devices is relatively low due to the thick perovskite layers (~350 nm). To increase the device transparency, we prepared devices with thinner perovskite layers under the optimum conditions of other steps as described above. **Figure 11a** shows the photos of the semitransparent perovskite solar cells with the thickness of the perovskite layer ranging from 150 nm to 350 nm (2-layer graphene electrodes are used in all of the devices). The red dash lines show the outline of the patterned FTO bottom electrodes and the edges of the graphene top electrode are indicated by green lines. The gold films deposited on one side are used to conduct holes from the top graphene electrodes. It is reasonable to find that the transparency of the device increases with the decrease of the perovskite layer thickness, as shown in **Figure 3.11a** and **3.11b**. All these devices show larger light transmittance at longer wavelength above 400 nm. The *J-V* curves of these devices with different active layer thicknesses are plotted in **Figure 3.11c** and **3.11d**. The device parameters (*Voc*, *Jsc*, FF and PCE) for different active layer thicknesses are shown in **Table 3.4**. The open circuit voltage remains almost unchanged at about 0.95±0.015 V when the active layer thickness is above 250 nm, but it becomes lower at thinner thickness, reaching the minimum of 0.755 V at a thickness of 150 nm most probably due to the incomplete coverage of the perovskite film in the device.[85] It is

also reasonable to find that *Jsc* and PCE decrease all the way with the decrease of the active layer thickness due to the decreased light absorption. Similarly, we can find that thinner perovskite films lead to smaller EQE values at any wavelength below 800 nm (see **Figure 3.12**).

Table 3.4 Photovoltaic parameters of the semitransparent perovskite solar cells with different perovskite layer thicknesses.

Perovskite layer thickness	Illumination side	V_{oc} (V)	J_{sc} (mA/cm^2)	FF (%)	PCE (%)	Average PCE (%)
350 nm	FTO	0.96	19.17	67.22	12.37	12.02±0.32
	Graphene	0.945	17.75	71.72	12.03	11.65±0.35
290 nm	FTO	0.94	17.93	65.68	11.07	10.67±0.36
	Graphene	0.96	16.80	66.47	10.72	10.23±0.45
250 nm	FTO	0.965	16.77	65.13	10.54	10.10±0.35
	Graphene	0.95	15.12	66.14	9.50	9.15±0.40
200 nm	FTO	0.91	15.92	61.99	8.98	8.72±0.28
	Graphene	0.90	13.98	66.60	8.38	7.95±0.36
170 nm	FTO	0.86	14.72	59.56	7.54	7.22±0.29
	Graphene	0.86	12.89	63.33	7.02	6.62±0.47
150 nm	FTO	0.79	13.55	57.27	6.13	5.98±0.25
	Graphene	0.755	12.00	65.23	5.91	5.70±0.20

Average PCE is the average value of more than 6 devices.

Figure 3.11e shows the relationship between the PCE and the transmittance at 700nm of the solar cells. The devices with 150nm-thick perovskite layers present the highest transmittance of about 50% at 700nm and show average PCEs of 5.98% and 5.70% from FTO and graphene sides, respectively. Compared with other semitransparent perovskite solar cells reported before,[85-91] our devices show the relatively high PCEs under light illumination from both sides at the same average transparency mainly due to the high transparency of the graphene electrodes (See **Table 3.5**). Moreover, the device performance of our devices is much better than that of other types of semitransparent solar cells, including organic solar cells,[95] and dye

sensitized solar cells[108]. Therefore, the devices are expected to find some potential applications in the future.

Table 3.5 Comparison of PCEs of different types of semitransparent solar cells.

Device type	Transparent Electrode	Device structure	PCE_{max} (T_{min})	PCE_{min} (T_{max})	References
Perovskite Solar Cell	Au	Glass/FTO/bl-TiO_2/$MAPbI_{3-x}Cl_x$/Spiro/Au	7.5% (7%)	3% (30%)	[85]
	Au	Glass/FTO/bl-TiO_2/$FAPbI_3$/Spiro/Au	5.2% (28%)		[86]
	Au	Glass/ITO/PEDOT:PSS/$MAPbI_3$/PCBM/Au/LiF	7.73% (10%)	3.39% (35.4)	[87]
	Carbon Nanotubes	Glass/FTO/bl-TiO_2/mp-TiO_2/$MAPbI_3$/ Carbon Nanotubes	6.87%		[90]
		Glass/FTO/bl-TiO_2/mp-TiO_2/$MAPbI_3$/Spiro/ Carbon Nanotubes	9.9%		
	Ag nanowires	Glass/ITO/PEDOT:PSS/ $MAPbI_{3-x}Cl_x$/ PCBM/ZnO/Ag nanowires	8.49% *Poor Stability		[88]
	Ag nanowires	Glass/FTO/bl-TiO_2/mp-TiO_2/$MAPbI_3$/Spiro/ Ag nanowires/PET	12.7%		[91]
	Ni mesh	Glass/FTO/bl-TiO_2/$MAPbI_{3-x}Cl_x$/Spiro/ PEDOT:PSS/Ni Mesh	13.3%		[89]
	Graphene	Glass/FTO/bl-TiO_2/$MAPbI_{3-x}Cl_x$/Spiro/ PEDOT:PSS+D-sorbitol/Graphene	12.02 (5.84%)	5.89% (21.76%)	**This work**
Organic Solar Cell	Graphene	Glass/ITO/ZnO/P3HT:PCBM/ PEDOT:PSS/Graphene/PMMA	2.6%		[95]
DSSC	Polyaniline (PANI)	Glass/FTO/TiO_2/N719/electrolyte/PANI	6.54%		[108]

Maximum PCE (PCE_{max}) corresponding to the minimum average visible transmittance (T_{min}).

Minimum PCE (PCE_{min}) corresponding to the maximum average visible transmittance (T_{max}).

Spiro=Spiro-OMeTAD.

It is notable that hysteresis of the *J-V* curves measured with positive (scan rate: +50 mV/s) and negative (scan rate: -50 mV/s) scan directions can be observed in all of the devices, which is a common problem for thin film perovskite solar cells.[74, 109] As shown in **Figure 3.13**, the PCE of the device calculated from a negative scan and

positive scan are 12.00% and 9.47%, respectively. So the PCEs obtained from the *J-V* curves are not the stable values of the device. The stabilized output power of the device was then characterized under the bias voltage of 0.72 V that corresponds to the maximum power of the device. As shown in **Figure 3.14**, the PCE increases with illumination time and arrives at the stable value of 11.17%, which is a little bit lower than the value obtained from the *J-V* curve with negative scan. Since the device has taken more than 50 s to arrive at the stable value, the big hysteresis of the *J-V* curves cannot be avoided when the device is characterized at the conditions of our experiments. But the PCEs obtained from the *J-V* curves by negative scan are very close to the stabilized values.

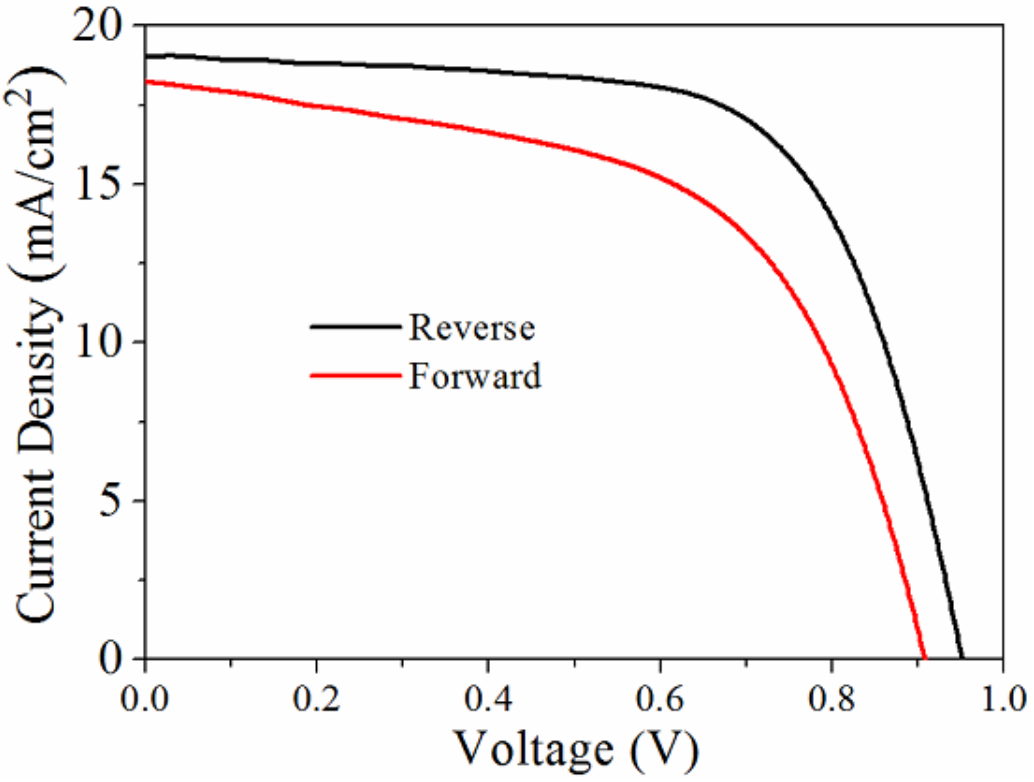

Figure 3.13 *J-V* characteristics of a semitransparent perovskite solar cell with a 2-layer graphene top electrode measured with reverse scan (from 1.5 V to -0.1 V) and forward scan (from -0.1 V to 1.5 V) with the scan rate of ±50 mV/s under the light illumination (100 mW/cm^2) from FTO side.

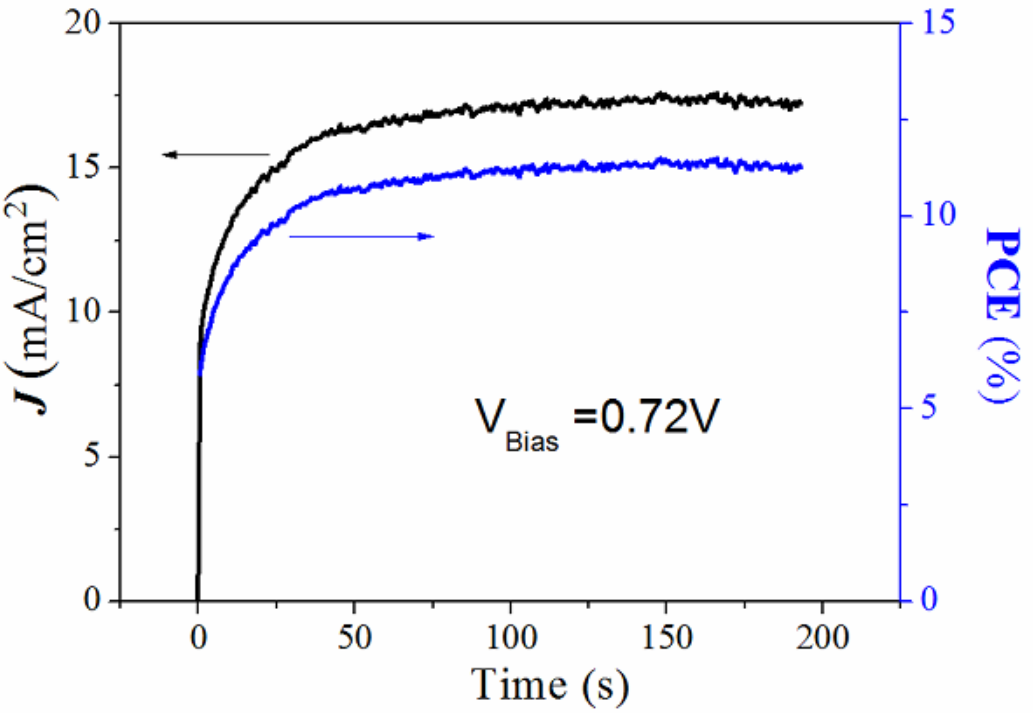

Figure 3.14 Steady-state photocurrents measured at the maximum power point (bias voltage: 0.72 V) versus time and the corresponding stabilized power output of the device.

3.4 Summary

In summary, semitransparent perovskite solar cells were fabricated by laminating stacked CVD graphene as top transparent electrodes on perovskite layers for the first time. The device performance was optimized by improving the conductivity of the graphene electrodes and the contact between the top graphene electrodes and the HTL (spiro-OMeTAD) on the perovskite films. The devices with double-layer graphene electrodes show the maximum PCEs of 12.02±0.32% and 11.65±0.35% from FTO and graphene side, respectively, which are relatively high compared with the reported semitransparent perovskite solar cells. This work indicates that CVD graphene is an ideal candidate for transparent electrodes of perovskite solar cells. Considering its excellent mechanical flexibility and convenient preparation, graphene electrodes are expected to be used in flexible

perovskite solar cells by printing or roll to roll process, which may find applications to complement the rigid inorganic solar cells currently dominated in the market.

Chapter 4 Few-layer Black Phosphorous Flakes for Hole-conducting at Grain Boundaries of Organometal Halide Perovskite Films

4.1 Introduction

Solar cells based on inorganic-organic hybrid perovskite materials, have obtained lots of attention during the past few years. Since the first report of the material used in solar cells in 2009,[2] the PCEs of PSCs have now reached a certified value of 22.7%, with an unprecedented fast growth rate. PSCs have attained comparable photovoltaic performance to CdTe and CIGS solar cells, and is approaching that of monocrystalline Si solar cells. The semiconducting organic-inorganic hybrid perovskites have shown great potential for photovoltaic applications, which are likely be attributed to their excellent optoelectronic properties, ease of processing, and low fabrication costs.[9, 10, 12, 19-22, 24, 27, 84]

In pursuit of high device efficiency and long-stability, the controlling of the perovskite film formation is of great importance. So far, most of the attention of researchers have been paid on the preparation of high-quality perovskite films and proper employment of charge transport layers. However, the interfaces between perovskite and charge transport layers are also crucial to the device performance and stability. It is believed that the hybrid perovskites contains under-coordinated ions (like $I^-$and Pb^{2+}) at film surfaces and grain boundaries (GBs).[110] These under-coordinated ions will behave as nonradiative recombination centers for charge carriers, which have an negative effect on the device performance of PSCs.[111-113]

Thus, the surface passivation strategies are needed to tackle this problem. In many cases, modification of perovskite interfaces with some semiconductor materials can greatly improve the device performance and reliability by optimizing the charge transport/extraction properties of the corresponding interfaces. Interfacial buffer layers between perovskites and charge transport layers often play great contributions to energy level band alignment, charge transport, trap passivation and device stability.[114, 115]

Fullerene Derivatives are often used to modify the interface between perovskite and ETLs.[116-118] Yang *et al*. adopted a triblock fullerene derivative (PCBB-2CN-2C8) to modify the TiO_2/perovskite interface in the planar n-i-p PSCs, which resulted in 20.7% improvement in PCE and much more better stability, because of the enhanced charge extraction, uplifted surface work function and reduced charge recombination at the interface.[116] Wu *et al.* also reported efficient inverted PSCs with a perovskite-fullerene gradient interlayer.[118] This structure was found capable of enhancing the PCEs of the devices owing to the improved photoelectron collection and reduced recombination loss. By employing this strategy, they have achieved a certified efficiency exceeding 18% (device area ~ 1 cm^2). Similarly, some organic small molecules were widely used as interfacial modification materials at the perovskite/HTL interface.[112, 113, 119, 120] Snaith *et al.* deposited a supramolecular halogen bonding donor-acceptor complexation on top of the perovskite film, and successfully passivated the hole traps at the perovskite/HTL heterojunction and led to enhanced operation in the PSCs. Park *et al*. adopted 2,3,5,6-Tetrafluoro-7,7,8,8-Tetracyano-quinodimethane (F4TCNQ) to modify the perovskite/HTL interface, which realized the dual function including the surface passivation and the interfacial doping of the intrinsic perovskite.[119] Consequently, the average PCE of the PSCs was remarkably improved from 14.3±0.9% to 16.4±1.0%.

Recently, two-dimensional materials like graphene (or graphene oxide, GO) and Transition metal dichalcogenides (TMDs) have also been used as interfacial buffer layers for PSCs.[110, 121-123] For example, Wen *et al.* reported the utilization of a solution processed amino-functionalized graphene for interfacial modification at the perovskite/spiro-OMeTAD interface.[110] It was found that the amino group could reduce surface trap density of perovskite films, and the graphene could behave as an efficient pathways for hole transport through the hole transport layer, which led to a great PCE improvement. Solution-processed few-layer MoS_2 flakes were also employed as an active buffer layer by Capasso and co-workers.[123] The MoS_2 flakes at the perovskite/spiro-OMeTAD interface act as hole transport layer as well as a surface passivation layer, which prevents the iodine migration from the perovskite into the spiro-OMeTAD and the formation of Au pathways from the metal electrode to the perovskite layer, giving a higher lifetime stability with respect to the reference cell.

Black phosphorus (BP) with a puckered orthorhombic layered structure, has emerged as a excelent two-dimensional material for its extraordinary electronic properties, like high carrier mobilities and tunable direct bandgap.[124] A room-temperature hole mobility of 5200 $cm^2V^{-1}s^{-1}$ was obtained by Long *et al*. from a field-effect transistor fabricated with few-layer BP flake.[125] Unlike the zero band gap of graphene, BP has a thickness-dependent band gap, which can be tuned from a narrow band gap of around 0.3 eV (for bulk BP) to a large band gap value around 2 eV (for single-layer).[124] And unlike MoS_2 which has an direct band gap only in its monolayer form (with indirect band gap in the bulk), BP has a universal direct band gap.[124] Its excellent optoelectronic properties make it an attractive nanomaterial for applications in batteries, transistors, supercapacitors, sensors and optoelectronic devices.[124, 126-131]

One key challenge in developing the interfacial materials is to find ultrathin

materials with high charge mobilities and tunable energy band gaps. Graphene can offer extremely high charge mobilities; however, the lack of a band gap presents a significant barrier. Transition metal dichalcogenides like MoS_2 possess thickness-dependent tunable band gaps; however, their charge mobilities are relatively low. Here we show that black phosphorus with room-temperature charge mobilities and tunable bandgap has excellent potential for interfacial modification.

In this chapter, we introduced the utilization of ultrathin BP flakes as an effective interfacial buffer layer between perovskite and hole transport layer to take advantage of the outstanding optoelectronic properties of BP material. The ultrathin BP nano-flakes, prepared by liquid phase exfoliation and dispersed in appropriate solvent, were deposited on top of perovskite films by drip-coating. The photovoltaic performances were greatly enhanced after the incorporation of BP flakes, due to the improved charge transport and reduced recombination loss at the perovskite/HTL interface. Besides, the device stability was also significantly improved due to the excellent passivation effect of the BP flakes.

4.2 Devices Fabrication and Characterization

Preparation of BP Thin Flakes.

The commercialized bulk BP crystals were used for the preparation of black phosphorus thin flakes. The crystals were firstly grinded manually with mortar in glovebox to get the BP powder. 10 mg of the obtained BP powder was dispersed in 4 ml anhydrous IPA and ultrasonicated for about 20 hours in a sonication bath (~400 W). The solution was then centrifuged at 3000 rpm for 40 min and the upper dispersion was collected and centrifuged again at 6000 rpm for 40 min. The upper dispersion solution containing the BP thin flakes was collected for test and solar cell application.

The obtained solution was stable for weeks. For comparison, MoS_2 flakes was prepared in the same way with BP flakes, GO flakes was purchased from market and BP QDs was synthesized according reference [132].

Materials Characterization

AFM measurement of BP thin films. Samples for AFM measurement was prepared by drip-coating of the obtained BP dispersion on clean Si/SiO_2 (300 nm SiO_2) substrates at 4000 rpm for 30 s in glovebox and annealed at 90 ºC for 5 min. A scanning probe microscope (SPM, Bruker Nanoscope 8) was used to measure the morphology, size and thickness of the exfoliated BP flakes.

TEM measurement of BP flakes and BP QDs. TEM and HRTEM observations were carried out by using a JEOL JSM 2100F scanning transmission electron microscope (operating at 200 kV) equipped with energy dispersive X-ray (EDX) accessory for element analysis.

UPS measurement of BP thin films. The films for ultraviolet photoelectron spectroscopy (UPS) measurements were prepared by drip-coating BP dispersion solution on silicon substrates in glovebox and annealed at 90 ºC for 5 min. UPS measurements were carried out with a VG ESCALAB 220i-XL ultrahigh vacuum surface analysis system equipped with a He-discharge lamp providing He-I photons of 21.22 eV. The base vacuum of the system is around 10^{-10} Torr, and a -5.0 V bias was applied during the measurements.

UV-visible absorbance measurement of BP dispersion. The absorbance spectra of the BP dispersion (in IPA) were measured by using a UV-Vis spectrophotometer (UV-2550, Shimadzu).

Raman measurement of BP flakes. A Horiba HR800 Raman microscopic system were used to get the Raman spectra of BP flakes on Silicon substrates. A 488 nm laser

with 180 mW output power was used.

Photoluminescence measurement of BP thin films. BP thin film for PL measurement was prepared by the same way as the above AFM samples. The steady-state PL measurements of the samples were carried out by using an Edinburgh FLSP920 fluorescence spectrophotometer. A 636.2-nm laser was used as an excitation light source.

Preparation of Perovskite Solar Cells

The control devices have a structure of glass/FTO/block-layer TiO_2 (bl-TiO_2)/mesoporous TiO_2 (mp-TiO_2)/perovskite/spiro-OMeTAD/Au.

Preparation of TiO_2 films. The FTO glass we use for solar cell fabrication was bought from market (already patterned in advance by laser). The sheet resistance of the FTO layer was about 14 Ω/□. The FTO substrates were cleaned with soap water and distilled-water, ultrasonically cleaned sequentially in acetone, distilled-water, ethanol and IPA, and dried with condensed air flow. Before spin-coating of the bl-TiO_2 layer, the FTO substrates were cleaned again with O_2 plasma treatment for 5 min. A thin bl-TiO_2 film (20 ~ 30 nm) was then deposited on the cleaned FTO glass by spin-coating at 4000 rpm from a precursor solution of 0.15 M titanium isopropoxide in anhydrous ethanol (with addition of 1.5 mM HCl from 37 wt% hydrochloric acid). The as-deposited film was annealed on hot plate for 10 min at 80 ºC and was later sintered at 500 ºC for 30 min in an oven with continuous air flow. After cooling down to room temperature, a mp-TiO_2 layer (150 ~ 200 nm) was spin-coated on bl-TiO_2 at 4000 rpm, using 30 nm TiO_2 nanoparticle paste (Dyesol 30 NR-D) diluted in anhydrous ethanol (weight ratio 1:7). After spin-coating, the substrates were dried on hotplate at 100 ºC for 10 min and then sintered again at 500 ºC for 30 min. After cooling down to room temperature, the substrates were immersed in a 40-mM clear

aqueous solution of $TiCl_4$ for 30 min at 70 ºC, washed with distilled-water and IPA after cooling down, and sintered again at 500 ºC for 30 min after blow-dried with air flow. And then, after cooling down to about 100 ºC, the substrates were transferred into glovebox (filled with high purity N_2) immediately to deposit perovskite film.

Perovskite precursor solution and film preparation. The organic CH_3NH_3I (MAI) was bought from Dyesol, and the PbI_2 (99%) was bought Sigma-Aldrich. The perovskite solution was prepared by dissolving 0.5763 g PbI_2 and 0.1986 g MAI in 1 ml mixed solvents of anhydrous DMF and DMSO (volume ratio, 8:1). After filtered, the perovskite precursor solution was spin-coated on top of the mp-TiO_2 film at 4000 rpm for 30 s in glovebox. During the spin-coating process, about 100 µl of chlorobenzene was poured onto the spinning substrate at 10 s after start. The substrates were then annealed on hotplate at 65 ºC for 2 min followed by 100 ºC for 60 min in glovebox.

Drip-coating of BP flakes on perovskite films. After the annealing process, the perovskite films were cooled down to room temperature. For devices with modification of BP flakes, around 100 µl of the freshly prepared dispersion solution was poured onto the spinning perovskite film (4000 rpm), followed by annealing at 90 ºC for 5 min and cooling down to room temperature. This drip-coating process may repeat for one or two times to form BP thin films with larger coverage and thickness.

Deposition of hole transport layer and top electrode. After the substrates cooling down to room temperature, a spiro-OMeTAD (Lumtec, 80 mg/ml in chlorobenzene) solution was spin-coated at 4000 rpm for 30 s in glovevox. The spiro-OMeTAD solution (1 ml) was doped with 29 µl 4-tert-Butylpyridine (TBP, Sigma-Aldrich) and 17.5 µl bis(trifluoromethylsulphonyl)imide lithium salt (Li-TFSI, Sigma-Aldrich, 520 mg/ml, dissolved in acetonitrile). The samples were then taken out from the glovebox and kept in dry air (humidity<10%) for around 10 hours. Finally, gold electrode (~ 80

nm) was deposited on top through a shadow mask by thermal evaporation. The active area of an individual solar cell was about 8 mm^2. Each substrate was then encapsulated with epoxy and glass.

Preparation of inverted structure perovskite solar cells. Perovskite solar cells with inverted structure (glass/ITO/P3HT/perovskite/PCBM/BP/BCP/Ag) were fabricated for comparison. Briefly, after O_2 plasma treatment of the ITO glass for 5 min, a hole transport layer was spin-coated from a 2.5 mg/ml P3HT solution in chlorobenzene at 3500 rpm and annealed at 135 ºC for 30 min in glovebox. After cooling down, the perovskite solution was spin-coated on top and annealed in the same way described above. For BP modified devices, the above dispersion solution containing BP thin flakes was deposited on top of perovskite film also by drip-coating and annealed at 90 ºC for 5 min. The electron transport layer was then deposited by spin-coating a PCBM solution (Nano-C, 20 mg/ml in chlorobenzene) at 3000 rpm and annealed at 90 ºC for 30 min. A thin 2,9-dimethyl-4,7-diphenyl-1,10-phenanthroline (BCP) film was then spin-coated at 5500 rpm from a saturated solution of BCP in methanol. And finally, a Ag electrode with thickness more than 100 nm was evaporated.

Preparation of GO modified perovskite solar cells. PSCs with a structure of glass/FTO/TiO_2/perovskite/GO/spiro-OMeTAD/Au were also prepared as comparison. The fabrication process was similar with the BP devices. GO flakes were also dispersed in anhydrous IPA and drip-coated on the perovskite films as a buffer layer.

Preparation of perovskite solar cells with BP only (without spiro-OMeTAD). For comparison, some devices were prepared without spin-coating of spiro-OMeTAD layer while the Au electrode was deposited directly on the BP film.

Preparation of perovskite solar cells with IPA drip-coating only. As control

devices, only IPA was coated on perovskite films instead of BP dispersion in IPA.

Solar Cell Characterizations.

Current-voltage characteristics. The *I-V* curves of the PSCs were measured with a Keithley 2420 source meter under light illumination of 100 mW/cm^2. The light intensity was calibrated frequently during I-V test by using a standard reference silicon solar cell to ensure accurate light intensity. The I-V characteristics were performed by applying an external voltage while measuring the current response with the Keithley 2420. For a standard sweeping cycle, the external applied bias changed from 1.2 V to 0 V (reverse scan) and then returned back to 1.2 V (forward scan). Normally, the voltage scan rate was 30 mV/s. And no preconditioning (such as longtime forward bias or light soaking) was applied before all the measurements.

EQE measurements. External quantum efficiency (EQE) was measured with a standard EQE test system of Newport, consisting of a xenon lamp (Oriel 66902, 300 W), a monochrometor (Newport 66902), a Silicon detector (Oriel 76175_71580), and a dual channel power meter (Newport 2931_C). The measurement was performed in DC mode at room temperature. The light spot is smaller than the active area of the device, to make sure that all the light was illuminated on the active area of the device. The EQE response from wavelength of 300 nm to 800 nm was recorded by a computer.

Stable power output measurements. The stable power output characteristic was carried out at the maximum power point of the device under standard light illumination of 100 mW/cm^2, and the current response was recorded as a function of time by a Keithley 2400 source meter.

Impedance measurements. The impedance measurements of the devices were carried out under light illumination of 100 mW/cm^2 (white light), by using a Zahner

Zennium 40630 electrochemical work station. The oscillating voltage was 50 mV and the applied DC bias voltages varied from 0 to 1.0 V. The frequency of the sinusoidal signal changed from 2 MHz to 1 Hz.

Illumination-V_{oc} and illumination-J_{sc} measurements. The relationship between Voc (or J_{sc}) and light intensity was recorded by a photo-electrochemical system (the integrated system consisting of the above-mentioned Zahner Zennium 40630 electrochemical work station and a light intensity control accessory). The light intensity can be tuned continuously from 0 to 100 mW/cm^2.

Photoluminescence quenching measurements. Samples for photoluminescence (PL) measurements were fabricated by spin-coating perovskite solution, BP solution and spiro-OMeTAD solution on quartz substrates, with a structure of quartz/perovskite, quartz/perovskite/spiro-OMeTAD and quartz/perovskite/BP/spiro-OMeTAD. Both the steady-state and time-resolved PL measurements of the samples were carried out by using an Edinburgh FLSP920 fluorescence spectrophotometer. A 485-nm laser was used as an excitation light source. All experiments were conducted at room temperature.

Device stability measurements. For device stability measurements, all the solar cells were encapsulated with epoxy and glass were kept in air with humidity around 30%.

Scanning electron microscopy (SEM) measurements was performed on a JEOL JSM 6335F field emission SEM.

4.3 Results and Discussion

Figure 4.1a shows the UV-visible absorption spectrum of the BP dispersion in anhydrous IPA, which is quite similar with the literature reports.[133, 134] Also, the inset

picture in **Figure 4.1a** shows a photo of the BP dispersion in isopropanol (IPA), which indicates the BP flakes were well dispersed in the solution, presenting a light-yellow color. It should be noticed that the solvent adopted for BP dispersion should have no damage on the perovskite film while maintaining good dispersion, thus IPA was used here. The BP flakes were also characterized with Raman spectroscopy, as shown in **Figure 4.1b**. Three peaks observed here in the Raman spectrum can be defined as A_g^1, B_{2g} and A_g^2 respectively.[127, 128, 130, 133] The inset in Figure 4.1b shows the schematic diagram of the crystal structure of BP.

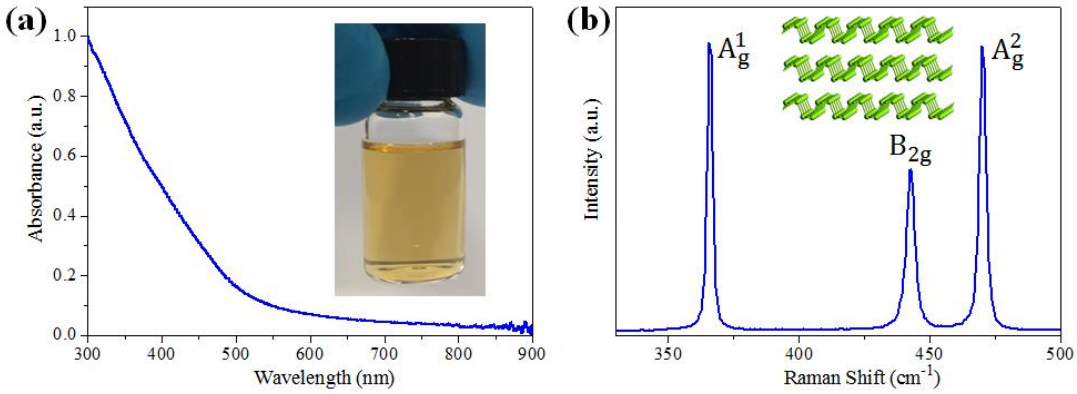

Figure 4.1 (a) UV-visible absorbance curve of BP dispersion in IPA. Inset shows the photo of the BP dispersion. (b) Raman spectrum of BP flakes.

The morphology of the BP flakes was characterized by atomic force microscopy (AFM) and transmission electron microscopy (TEM). **Figure 4.2a** shows the AFM image of BP flakes on oxidized silicon substrate. Statistics of the size and thickness of BP flakes based on the AFM image were demonstrated in **Figure 4.2b and c.** The average size of the BP flakes was about 39 nm, while the average thickness was around 4.3 nm. Most of the BP flakes were thinner than 8 nm, which is suitable for charge transport as a buffer layer. **Figure 4.3a** shows the bright field TEM image of the BP flakes, showing similar flake size with that of the AFM image. In-situ energy dispersive X-ray spectroscopy (EDX) study of the BP flakes under TEM revealed that the flakes consist of phosphorus element only, as shown in **Figure 4.3c**. High

resolution TEM (HRTEM) image of a BP flake shown in **Figure 4.3b** further confirms the orthorhombic crystal structure of BP. The lattice fringe spacings in two perpendicular directions (~0.217 nm and 0.168 nm) is corresponding to the (200) and (020) lattice planes of BP, respectively.

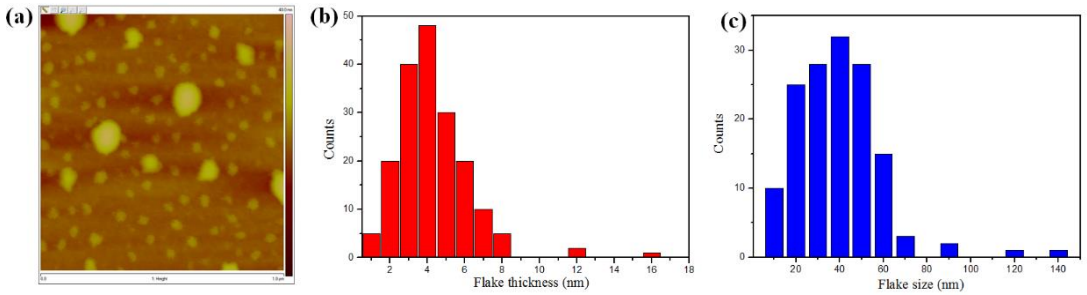

Figure 4.2 (a) AFM image of drip-coated BP flakes on Si substrate. (b) and (c) The thickness and size distribution graphs of the BP flakes.

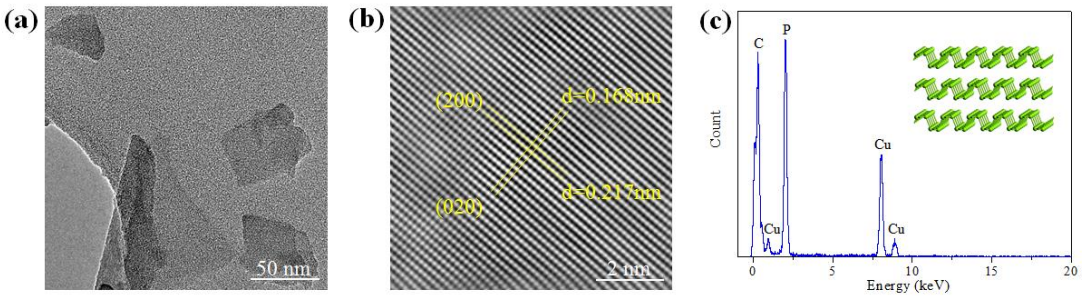

Figure 4.3 (a) Bright field TEM image of the BP flakes. (b) High resolution TEM image of one BP flake (after Fourier filtering). (c) Energy dispersive X-ray spectrum of BP flake. Inset show the crystal structure of BP.

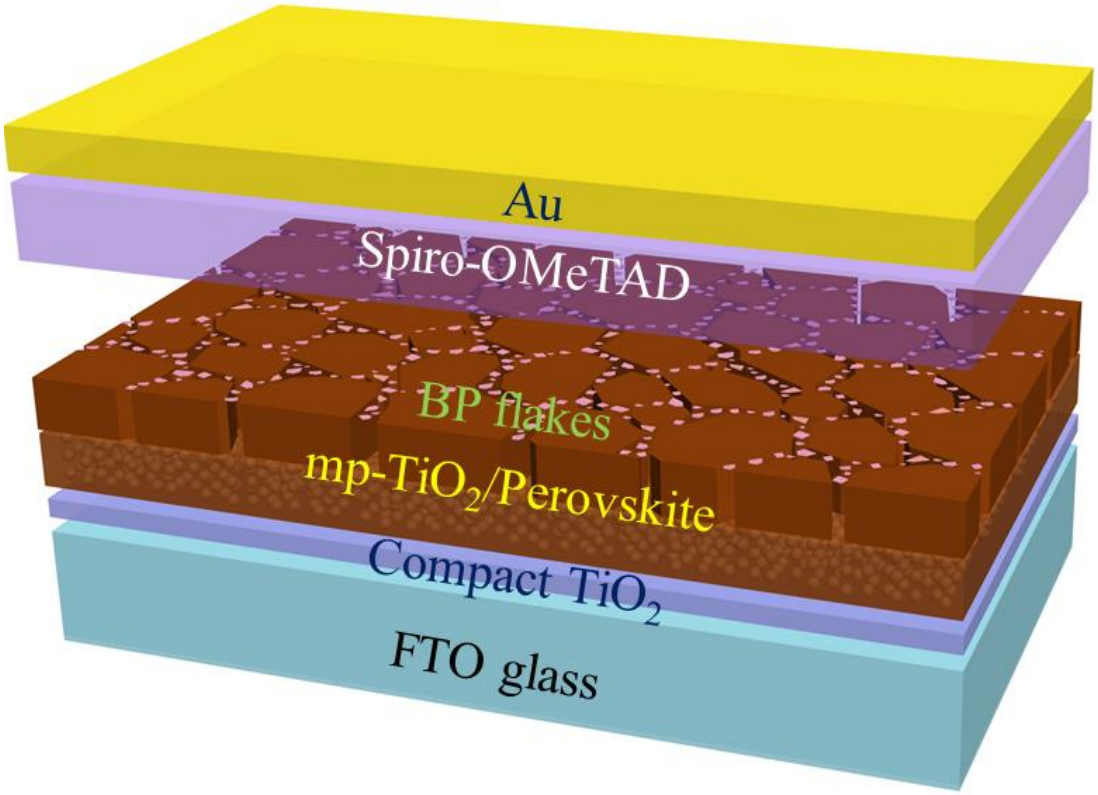

Figure 4.4 The schematic diagram of the BP-modified perovskite solar cells (normal structure).

Perovskite solar cells were fabricated with a device configuration of glass/fluorine doped tin oxide (FTO)/block layer TiO_2 (bl-TiO_2)/mesoporous TiO_2 (mp-TiO_2)/perovskite/spiro-OMeTAD/Au, as shown in **Figure 4.4**. The perovskite films were prepared through an anti-solvent assisted crystallization method. According to the SEM image of the perovskite film, as shown below, the perovskite film was quite smooth and uniform without pinholes. Dispersion solution of BP thin flakes in IPA was coated for 1 ~ 3 times on top of perovskite films through a dripping deposition method. The BP layer works as an interfacial buffer layer between perovskite and spiro-OMeTAD.

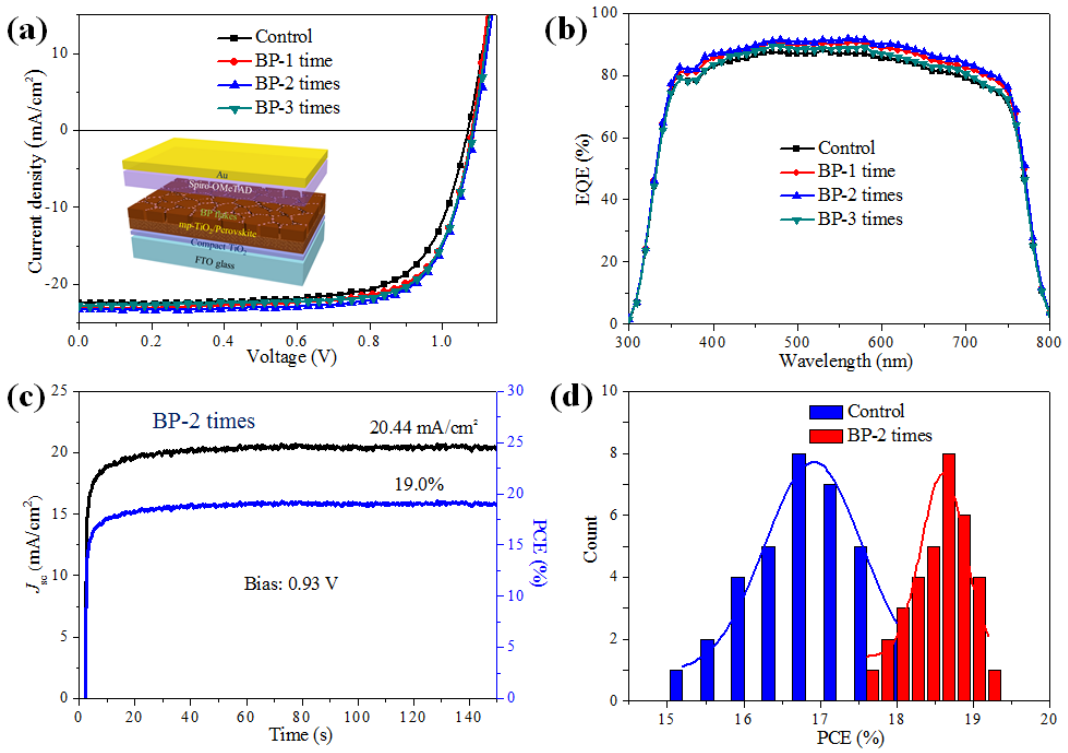

Figure 4.5 Representative *J-V* curves (a) and EQE spectra (b) of perovskite solar cells without and with BP deposition (1~3 times) on perovskite surface. (c) Steady-state photocurrent measured at a bias voltage (0.93 V) near the maximum power point and stabilized power output. (d) Histogram of efficiencies measured using reverse scans for 30 devices.

Table 4.1 Photovoltaic parameters of perovskite solar cells without and with BP deposition (1~3 times) on perovskite surface (average of 20 devices for each condition).

Devices	**V_{oc} (V)**	**J_{sc} (mA/cm^2)**	**FF (%)**	**PCE (%)**	**Champion PCE (%)**
Control	1.07±0.01	22.38±0.50	70.6±1.90	16.88±0.71	17.96
BP-1 time	1.08±0.01	23.13±0.38	72.1±1.48	18.05±0.63	18.87
BP-2 times	1.09±0.01	23.24±0.42	73.7±1.15	18.65±0.49	19.16
BP-3 times	1.085±0.01	22.78±0.50	74.0±1.42	18.26±0.45	18.80

Figure 4.5 shows the representative current density-voltage (*J-V*) curves of the perovskite solar cells without (control device) and with BP deposition (1 ~ 3 times) on perovskite surface. The corresponding photovoltaic parameters were listed in **Table 4.1**. The control devices exhibited only a moderate photovoltaic performance, with

average PCE of 16.88%, V_{oc} of 1.07 V, J_{sc} of 22.38 mA/cm^2 and FF of 70.6%. It was interesting that a dramatically improved photovoltaic performance was obtained when the BP dispersion was drip-coated for 1 time on perovskite layer, achieving an average V_{oc} of 1.08 V, J_{sc} of 23.13 mA/cm^2, FF of 72.1% and PCE of 18.05%, which is approximately 7% higher than that of the control devices. Moreover, the device performance was further improved when BP was drip-coated for 2 times (which is the optimized condition), showing an average V_{oc} of 1.09 V, J_{sc} of 23.24 mA/cm^2, FF of 73.7% and PCE of 18.65% (about 10.5% higher than that of the control devices). However, the device performance decreased slightly when BP was deposited for 3 times, which could be explained according to the SEM images of BP flakes on perovskite films, as shown in **Figure 4.6 and 4.7**. It was noted that most of the BP thin flakes were distributed at the grain boundaries, as illustrated by the schematic diagram below. According to the contact angle measurement results, shown in **Figure 4.8**, the water contact angle was smaller on amorphous perovskite precursor film (~27º) than that on the crystalline perovskite film (~54º) and the single crystal (72º) surfaces. This indicates that the grain boundary area, which often contains lots of amorphous phases, shows higher surface energy and stronger interaction with BP dispersion in IPA. Also, the grain boundary area is lower in height than the grain area, as indicated in the AFM image of the perovskite surface, shown in **Figure 4.9**. Therefore, most of the flakes will leave at the grain boundaries. The optimized BP coating times of BP was two times, which are supposed to be ascribed to the appropriate coverage of BP at the grain boundaries. Thus, in general, compared with the control devices, the photovoltaic performance of BP-modified perovskite solar cells (2 times) was higher in all the photovoltaic parameters (PCE, J_{sc}, V_{oc} and FF) at different levels. The champion device shows a V_{oc} of 1.10 V, J_{sc} of 23.25 mA/cm^2, FF of 74.9% and PCE of 19.16%, as shown in **Figure 4.10** and **Table 4.2**. Apparently, the hysteresis was greatly reduced with the incorporation of BP flakes compared with control devices.

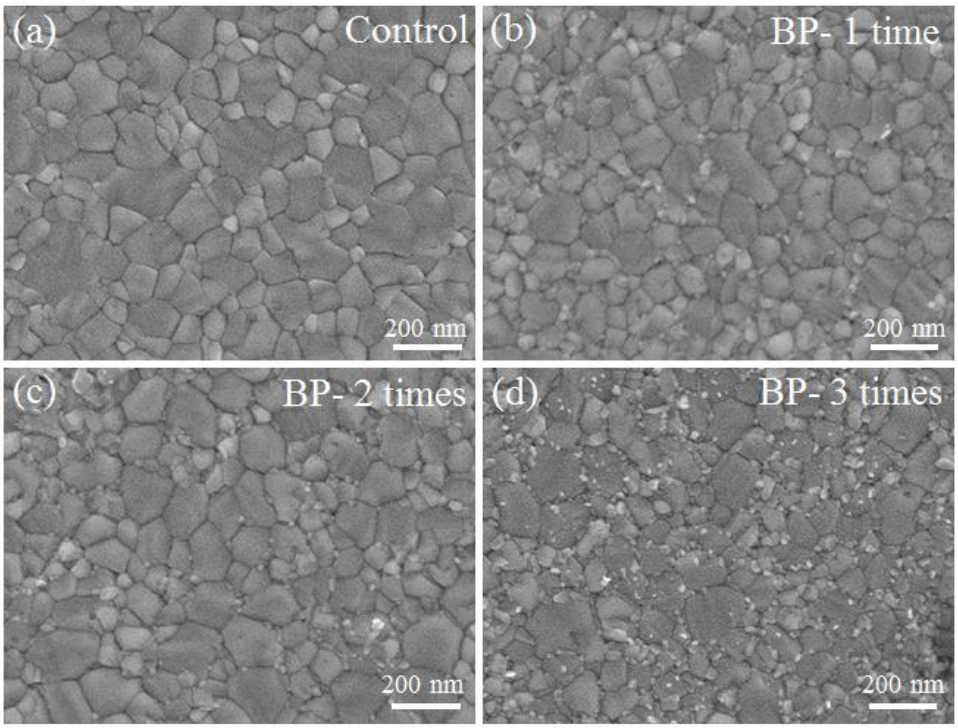

Figure 4.6 Low magnification SEM images of perovskite films without and with BP drip-coating for 1 ~ 3 times.

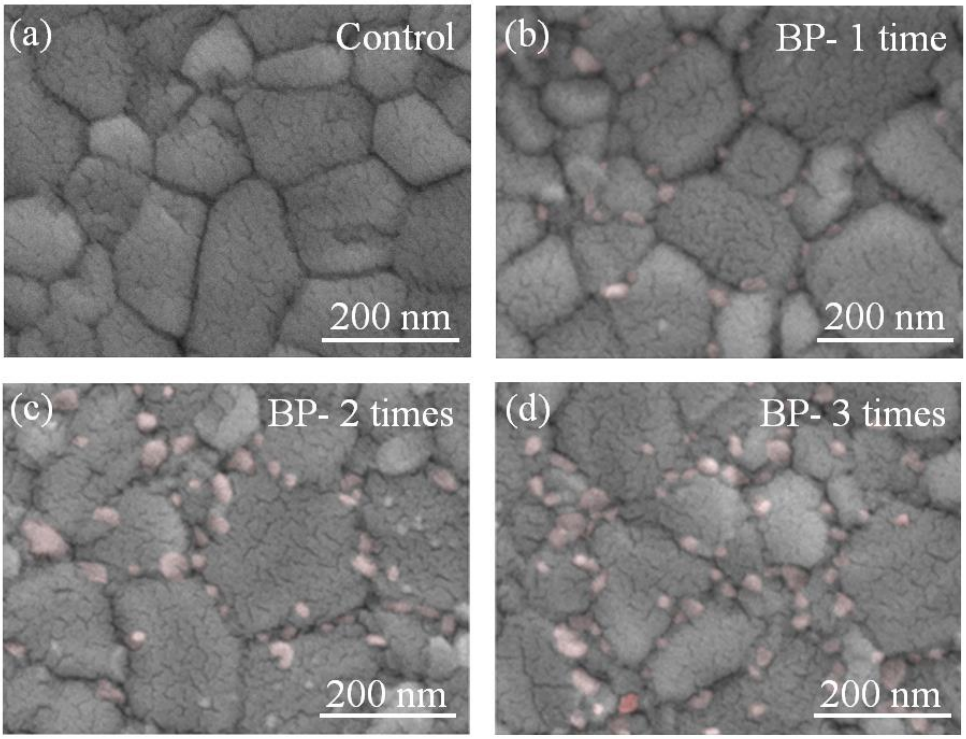

Figure 4.7 High magnification SEM images of perovskite films without and with BP drip-coating for 1 ~ 3 times.

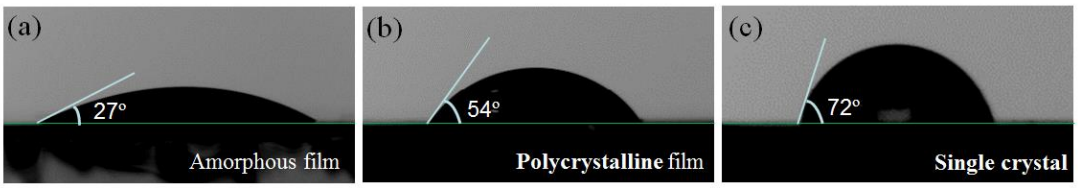

Figure 4.8 Contact angle of water on different perovskite surfaces.

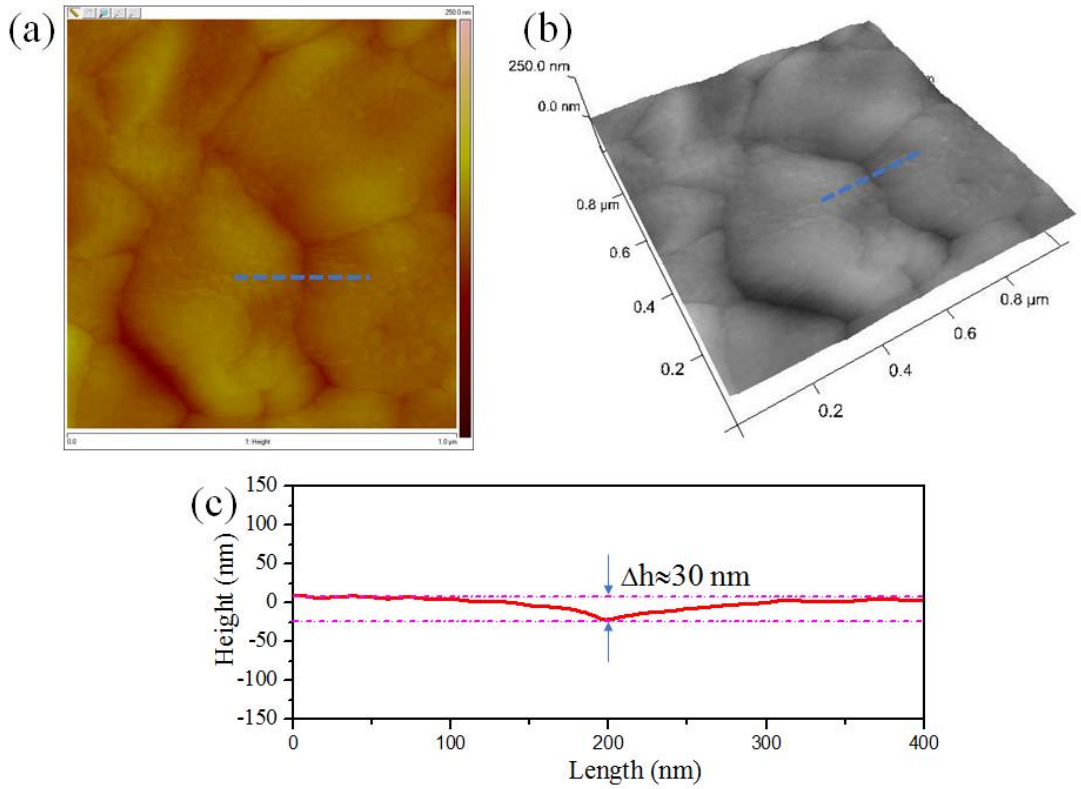

Figure 4.9 (a) 2D AFM image perovskite film. (b) 3D AFM image of perovskite film. (c) The height profile obtained at the grain boundary area in figure a and b.

Table 4.2 Photovoltaic parameters of perovskite solar cells without and with BP deposition on perovskite surface, showing *J-V* hysteresis with the forward and reverse scans.

Devices	Scan direction	V_{oc} (V)	J_{sc} (mA/cm^2)	FF (%)	PCE (%)
Control	Reverse	1.075	22.66	72.3	17.60
	Forward	1.065	22.64	60.5	14.59
BP-2 times	Reverse	1.10	23.25	74.9	19.16
	Forward	1.105	23.06	69.8	17.78

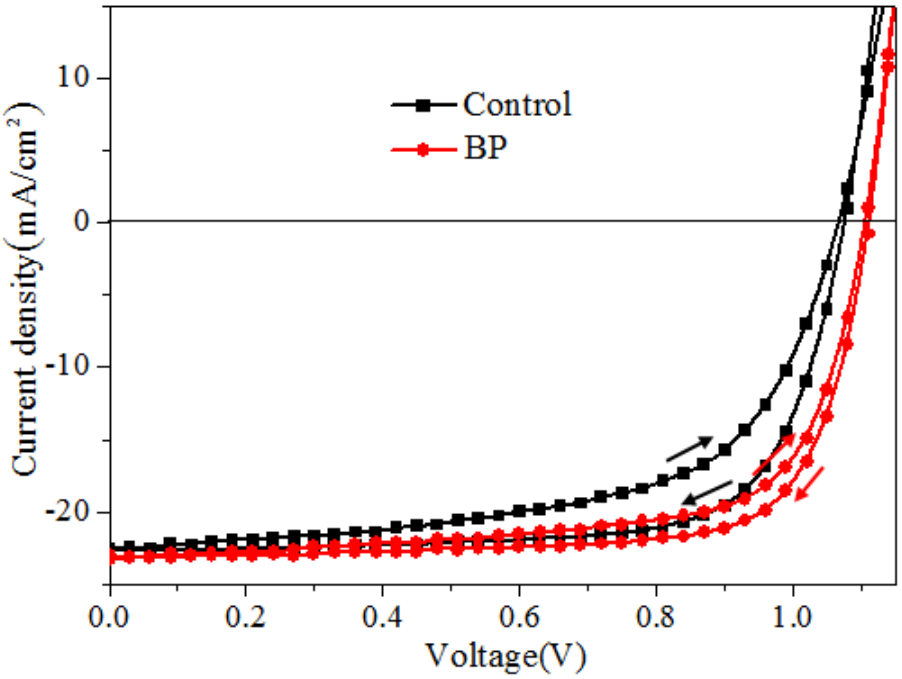

Figure 4.10 *J-V* curves of champion devices without and with BP deposition on perovskite surface.

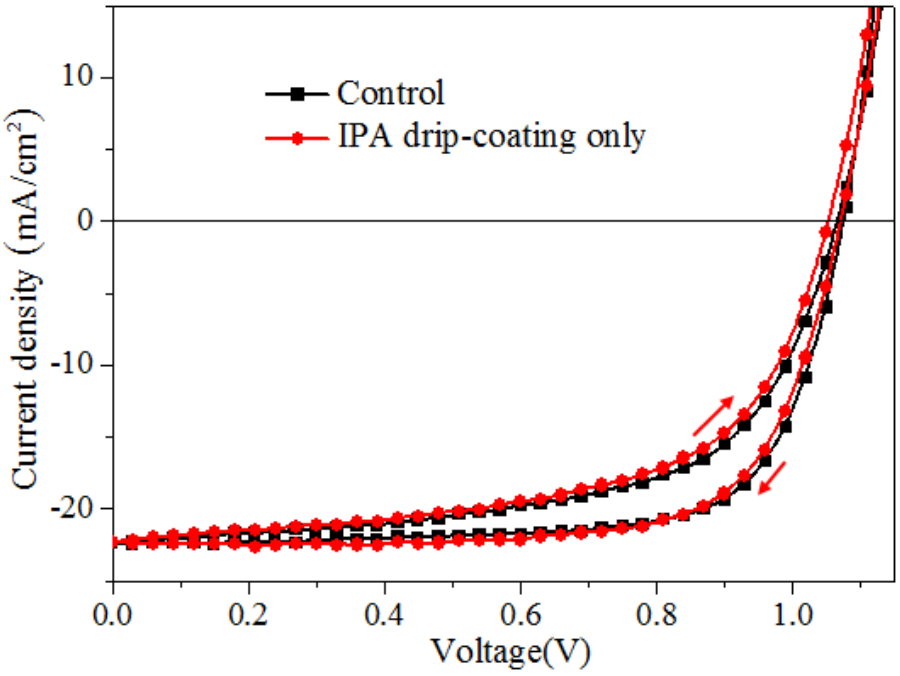

Figure 4.11 *J-V* curves perovskite solar cells with and without (control) IPA drip-coating.

To eliminate the effect of IPA solvent in the BP dispersion during the dripping deposition, devices with only IPA drip-coating on perovskite films were prepared as one set of reference devices. The *J-V* curves of the devices with and without IPA coating were presented in **Figure 4.11**. It was observed that there was no clear difference between the devices, showing that the IPA solvent here used have no obvious effect on the device performance.

Figure 4.5b shows the external quantum efficiency (EQE) spectra for the above cells. In comparison with the EQE of control device, the remarkable increased EQE value of the BP-modified devices in the whole wavelength range (from 300 nm to 800 nm) well explains the enhanced J_{sc} in *J-V* characteristics. The integrated current density based on the best EQE spectrum (BP-2 times) was approximately 22 mA/cm^2 (as shown in **Figure 4.12**), which are very close to that derived from the *J-V* curves.

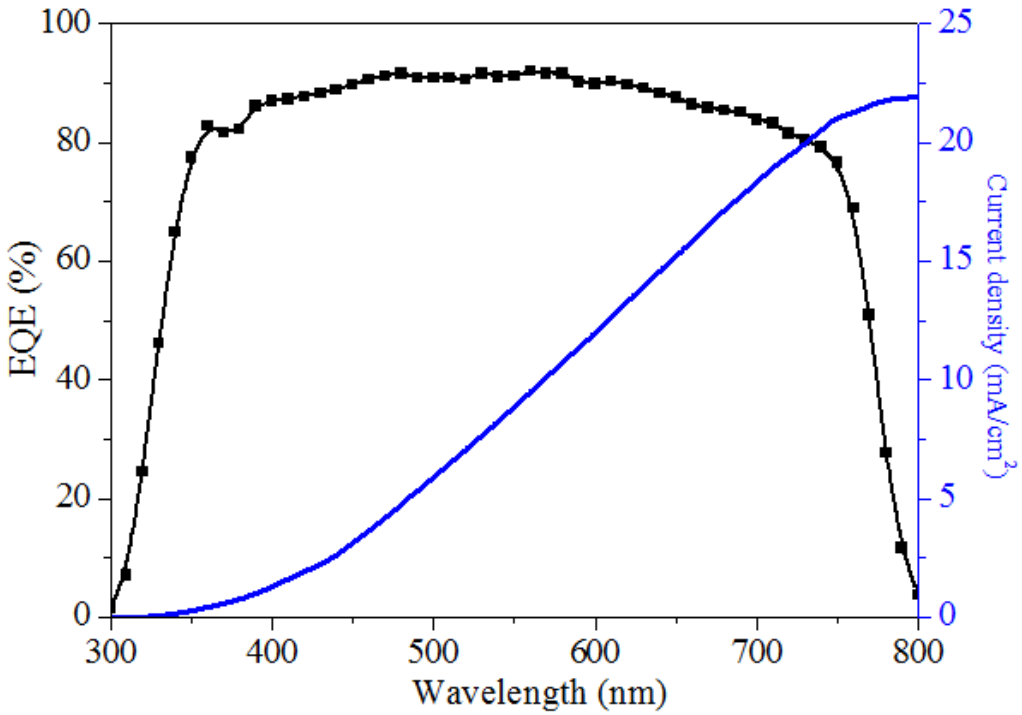

Figure 4.12 EQE curve and the integrated photocurrent from one of the best BP-modified perovskite solar cells.

By applying a voltage bias at the maximum power point (0.93 V) to the champion device mentioned above, a stabilized photocurrent of 20.44 mA/cm^2 and efficiency of ~19.0% was obtained, as shown in **Figure 4.5c**, which is in good agreement with the *J-V* characteristics. **Figure 4.5d** shows the histogram statistics of PCEs for 30 devices fabricated under the above optimized conditions. The PCEs calculated from reverse scanning results were distributed in a narrow range between 17.23% and 19.16%, with average PCE of 18.65%, showing good device reproducibility.

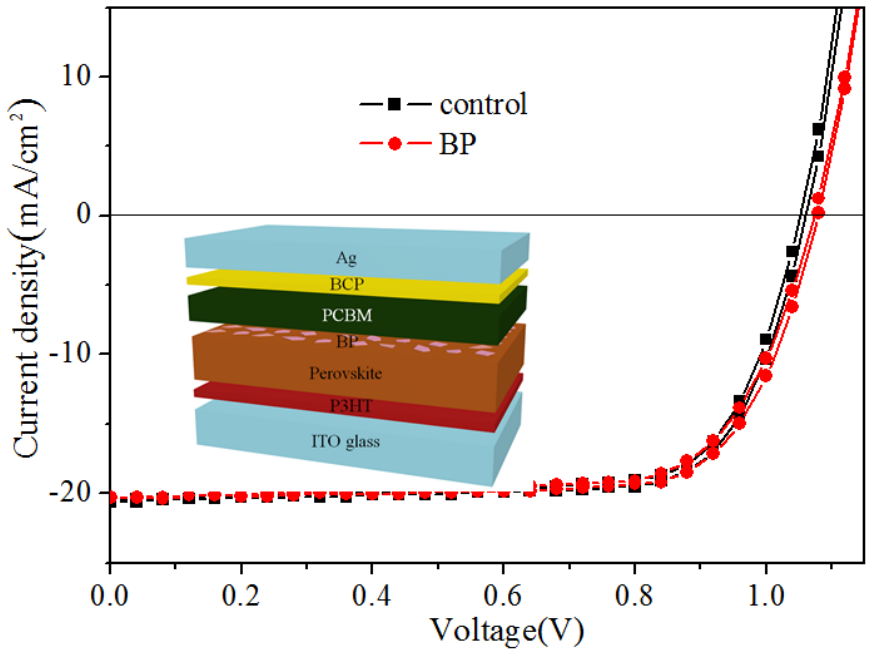

Figure 4.13 *J-V* curves of inverted-structure perovskite solar cells (inset shows the device structure).

Table 4.3 Photovoltaic parameters of inverted-structure perovskite solar cells without and with BP deposition (2 times) on perovskite surface. The average PCE was calculated based on a batch of 8 devices.

Devices	Scan direction	V_{oc} (V)	J_{sc} (mA/cm^2)	FF (%)	PCE (%)	Average PCE (%)
Control	Reverse	1.06	20.60	74.3	16.22	15.65
	Forward	1.05	20.55	73.3	15.82	15.21
BP	Reverse	1.08	20.30	74.3	16.28	15.48
	Forward	1.07	20.32	71.7	15.60	14.70

The above results indicate that the BP film in the structure of glass/FTO/bl-TiO_2/mp-TiO_2/perovskite/BP/spiro-OMeTAD/Au can greatly enhance the device performance. As another set of reference devices, perovskite solar cells with inverted structure (glass/ITO/P3HT/perovskite/PCBM/BCP/Ag) were also prepared.[135] BP flakes were deposited in the similar way as interfacial layer between perovskite and PCBM. The *J-V* cures and photovoltaic parameters of the inverted cells were shown in **Figure 4.13** and **Table 4.3**, respectively. It turned out that the average efficiencies of the inverted cells decreased slightly after BP modification. In considering of the lower performance in the inverted-structure cells, the large enhancement of photovoltaic performance in normal-structure devices should be attributed to the enhanced hole extraction or reduced recombination loss at the perovskite/HTL interface.

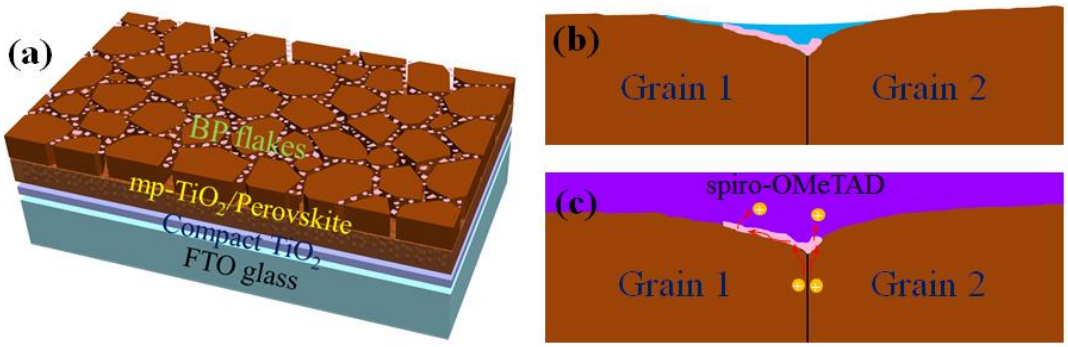

Figure 4.14 (a) Schematic diagram of BP-modified perovskite films. (b) Schematic diagram of the grain boundary area when BP dispersion in IPA was drip-coated on the perovskite films. (c) Schematic diagram of the grain boundary area after deposition of BP and spiro-OMeTAD. BP flakes were left at the grain boundary area.

Figure 4.14a shows the schematic diagram of the BP-modified perovskite films. The BP flakes were found at the grain boundary region, as confirmed by the SEM images in **Figure 4.7**. When the BP dispersion in IPA was drip-coated on the perovskite film, as illustrated in **Figure 4.14b**, the BP flakes are more likely leave at the grain boundary after the spinning process due to the lower height and the higher

surface energy of the grain boundary area. Thus, for the complete device, the BP flakes can contribute greatly to the charge transport at the grain boundary region, as shown in **Figure 4.14c**.

Figure 4.15 Dispersion of 2D materials in anhydrous IPA.

Besides, we also compared the BP thin flakes with GO flakes, MoS_2 flakes and BP quantum dots (BP-QDs) as perovskite/HTL interface buffer layer in normal-structure perovskite solar cells. **Figure 4.15** shows the photos of these dispersions in IPA. The TEM images of BP-QDs are shown in **Figure 4.16.** The average size of BP nanocrystals is less than 10 nm, and the crystal structure can be confirmed based on the HRTEM image. **Figure 4.17** shows the TEM images of the MoS_2 flakes, which have similar size with the BP flakes. The SEM images of perovskite films modified with GO and MoS_2 flakes are shown in **Figure 4.18**. It is interesting to find that most of the flakes are distributed at the grain boundary area the same as that of the BP flakes on perovskite surface. The obtained *J-V* curves and photovoltaic parameters are shown in **Figure 4.19** and **Table 4.4**, respectively. The results show that the BP flakes give better photovoltaic performance with respect to the other 2D materials. Thus, the ultra-thin BP flakes is better as hole extraction buffer layer compared with GO flakes, MoS_2 flakes and BP-QDs, which is probably

attributed to the high carrier mobility and crystallinity of BP flakes. By comparing the HRTEM images of BP flake and QDs in **Figure 4.20**, it is noted that the BP QDs shows poor crystallinity with many lattice defects, while the BP flake is well crystallized showing regular crystal lattice. Besides, due to the high specific surface area, BP QDs have a lot more surface dangling bonds than flakes, which will introduce lots of deep trap states.[136] In comparison with BP QDs, the much better crystallinity and less surface dangling bonds of BP thin flakes offer great advantages as interfacial buffer layers. This result indicates the superior potential of BP thin flakes as effective hole collection buffer layer in photovoltaic devices.

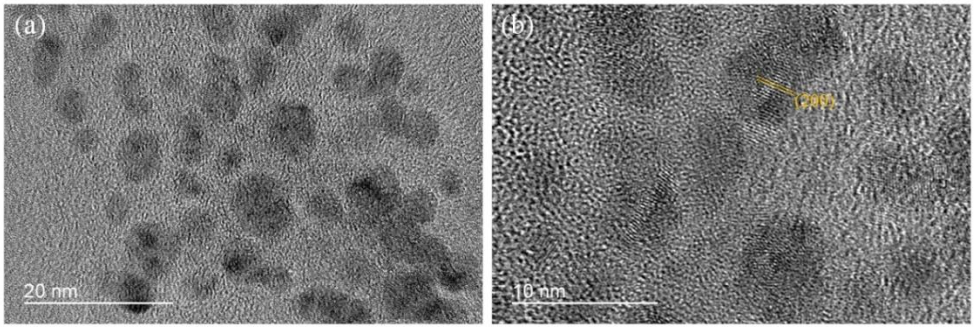

Figure 4.16 TEM images of BP QDs.

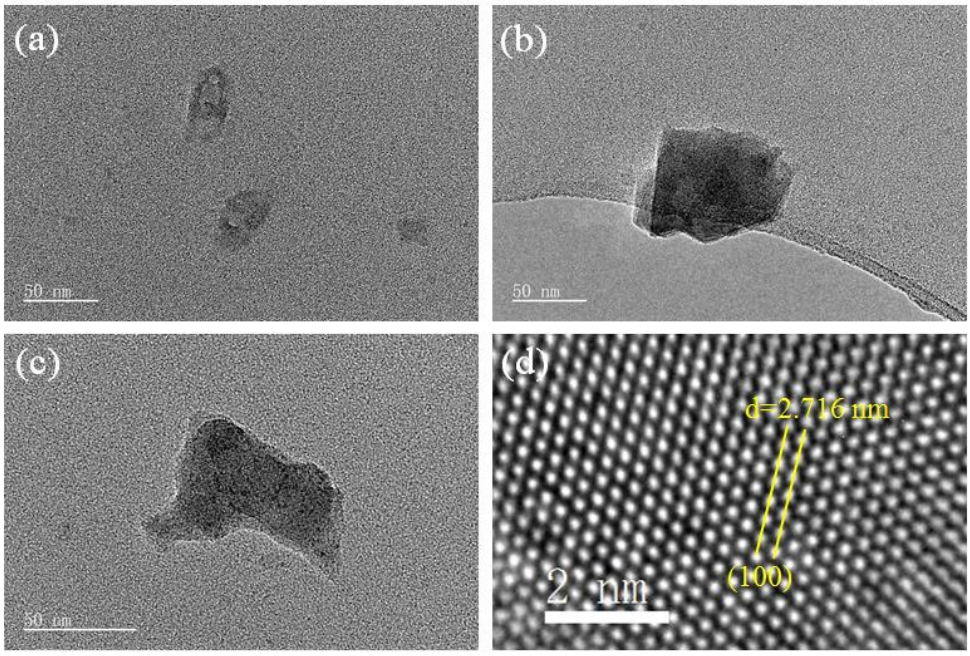

Figure 4.17 TEM images of MoS_2 flakes.

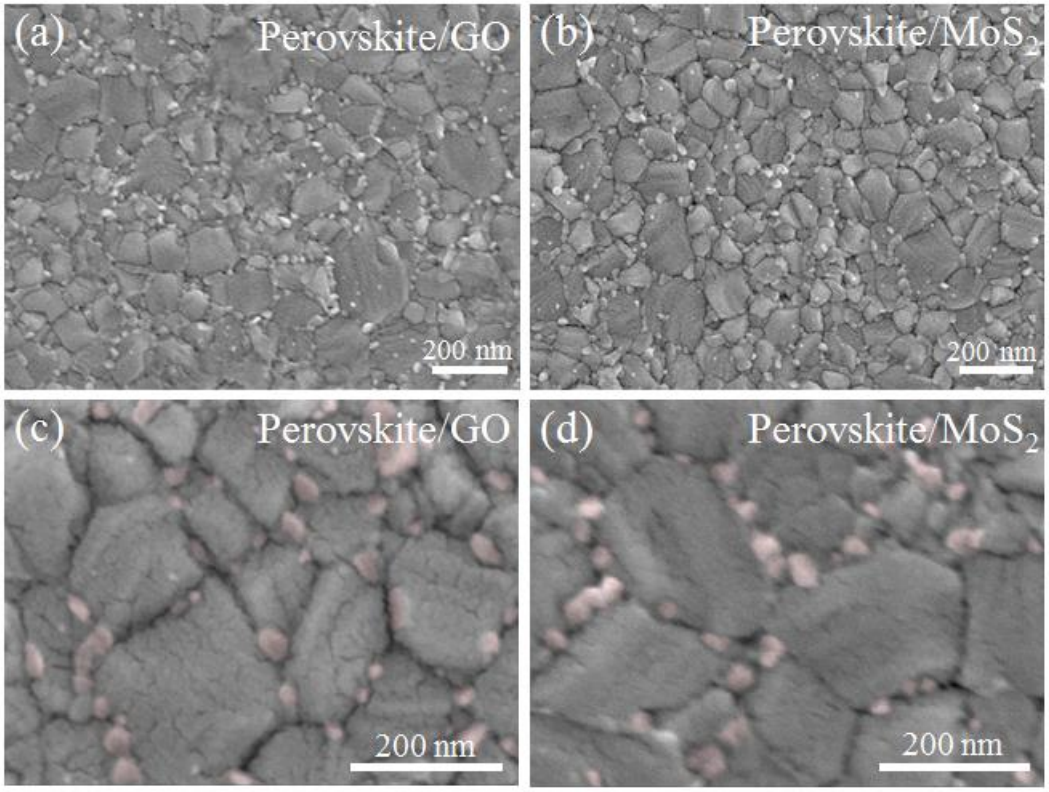

Figure 4.18 SEM images of perovskite films modified with GO and MoS_2 flakes.

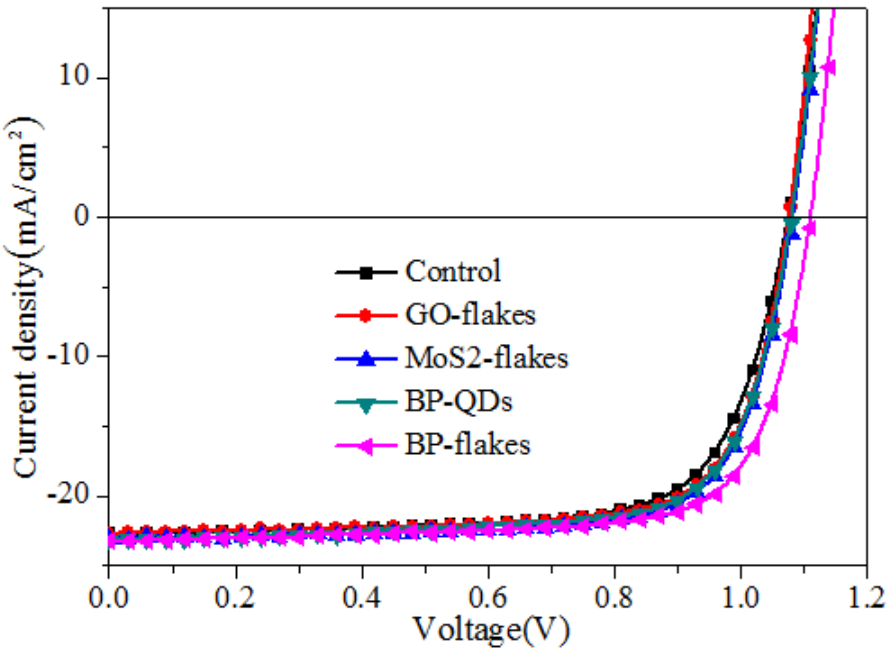

Figure 4.19 *J-V* curves of perovskite solar cells with different interfacial layers, including GO flakes, MoS_2 flakes, BP-QDs and BP-flakes.

Table 4.4 Photovoltaic parameters of perovskite solar cells with different interfacial layers, including GO-flakes, MoS_2-flakes, BP-QDs and BP-flakes.

Devices	V_{oc} (V)	J_{sc} (mA/cm^2)	FF (%)	PCE (%)
Control	1.075	22.66	72.3	17.60
GO-flakes	1.075	22.70	74.3	18.12
MoS_2-flakes	1.08	23.01	74.4	18.51
BP-QDs	1.08	23.15	73.3	18.33
BP-flakes	1.10	23.25	74.9	19.16

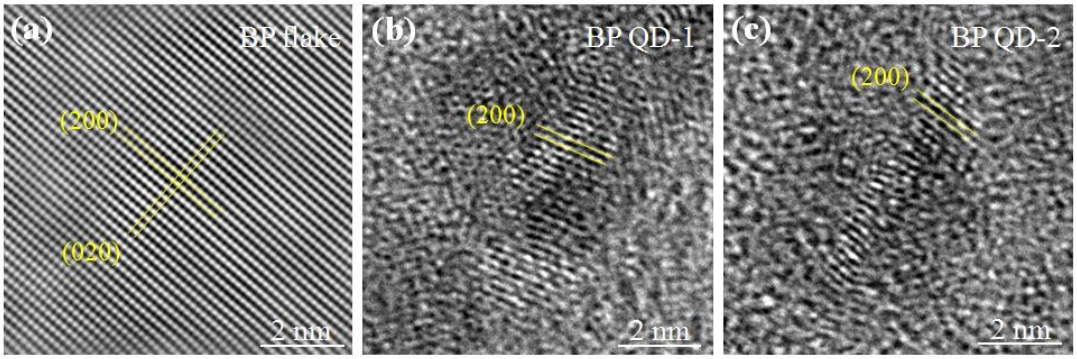

Figure 4.20 The HRTEM images of BP flakes and QDs with the same magnification.

To understand the tremendous performance for the BP-modified perovskite solar cells, we carried out a series of optical and electrical characterizations on the perovskite films and devices. Firstly, steady-state and time-resolved photoluminescence (PL) characterizations were carried out for the following three samples: perovskite, perovskite/spiro-OMeTAD (perovskite/spiro) and perovskite/BP/spiro-OMeTAD (perovskite/BP/spiro) films. The obtained PL spectra were shown in **Figure 4.21**. The perovskite film itself showed a strong PL peak with a relatively long lifetime. As shown in **Figure 4.21a**, the introduction of spiro-OMeTAD layer on top of perovskite reduced the PL intensity greatly, which was further quenched by the presence of BP buffer layer, indicating a more efficient hole transfer property for the perovskite/BP/spiro-OMeTAD case. The time-resolved PL decay curves in **Figure 4.21b** showed similar results. The decay curves were fitted

with a biexponential model: $y(t) = y_0 + A_1 e^{-t/\tau_1} + A_1 e^{-t/\tau_2}$. The derived PL lifetime constants (τ_1 and τ_2) of the bare perovskite was 3.4 ns and 25.3 ns, which decreased to 1.4 ns and 9.2 ns when spiro-OMeTAD was coated, and further dropped to 0.8 ns and 2.9 ns after BP modification. The improved PL quenching yield of the BP-modified devices indicates an improved hole transfer rate from perovskite to spiro-OMeTAD, which may originate from the reduced centers and thus reduced recombination loss at the interface after PB modification. These results are in accordance with the improved EQE and larger J_{sc} values of the BP-modified cells.

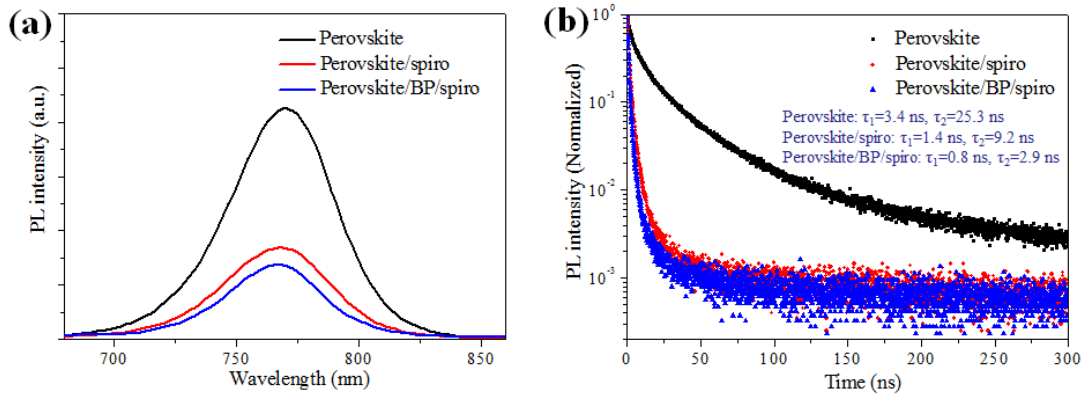

Figure 4.21 Steady state and time-resolved PL spectra of perovskite film, perovskite/spiro film and perovskite/BP/spiro film; the films were deposited on quartz substrates.

To further investigate the charge recombination behavior of the perovskite solar cells with and without BP modification, we performed the transient photocurrent and photovoltage measurements. The J_{sc} and V_{oc} as a function of light intensity was shown in **Figure 4.22**. It can be found that the BP-modified device exhibits a higher J_{sc} and V_{oc} values than the reference device under any light intensity, which is in accordance with the higher J_{sc} and V_{oc} values in the *J-V* characteristics. Both devices show linear features in case of J_{sc} while the BP-modified device shows a larger slope than that of the reference device, which is in accordance with the increased J_{sc} after BP modification. For the reference device, the V_{oc} value drops quickly when the light

intensity decreases, showing a trap-assisted recombination process dominated by deep-level trap states. However, for the BP-modified device, the light intensity-V_{oc} slope is quite stable with varying light intensity, suggesting that the introduction of BP flakes at the interface can greatly help reduce the trap-assisted recombination process.[120]

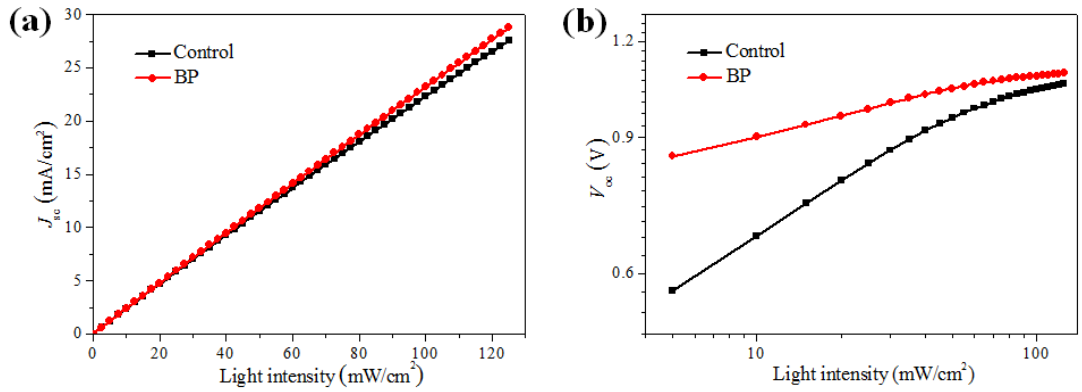

Figure 4.22 J_{sc} and V_{oc} of the perovskite solar cells as a function of light intensity.

Electrochemical impedance spectroscopy (EIS) measurements were also performed on the PSCs with and without BP modification under light illumination of 100 mW/cm^2. **Figure 4.23a and b** shows the EIS spectra of the devices at different bias under constant light illumination. Two different regions can be found in the plots: a low frequency region related with slow dielectric and ionic relaxation in perovskite films (small half circle), and a high frequency region corresponding to the charge recombination process (big half circle). When a 0.8 V bias voltage was applied, the BP-modified PSCs show much higher recombination resistance (~ 462 Ω) than that of the control device (~327 Ω), indicating improved hole extraction from perovskite to spiro-MeOTAD. **Figure 4.23c and d** shows the recombination resistance (R_{rec}) and carrier lifetime values of the two devices at different applied voltages under light illumination of 100 mW/cm^2. The R_{rec} and lifetime data were derived from the Nyquist plots obtained at a variety of voltages (as shown in **Figure S15**). Both devices show a similar decrease of R_{rec} and lifetime with the increase of the bias voltage due to the

increased carrier densities,[137] and higher R_{rec} value and longer carrier lifetime were observed in the BP-modified PSCs at any bias voltages compared with the control device, demonstrating a slower recombination rate and longer carrier lifetime in the BP-modified cell. Thus, the observation is consistent with the better photovoltaic performance of the BP-modified solar cell than the control device. The reduced recombination in the BP-modified solar cells can be attributed to two possible reasons. One is the passivation effect of the BP flakes, which can reduce direct carrier recombination at the perovskite/HTM interface. The other is the lower density of trap states at the perovskite/BP/HTM interface, as evidenced by the above measurements. Furthermore, the increased R_{rec} will contribute to the shunt resistance of the solar cells, which is the main reason for the increased FF of the BP-modified device.

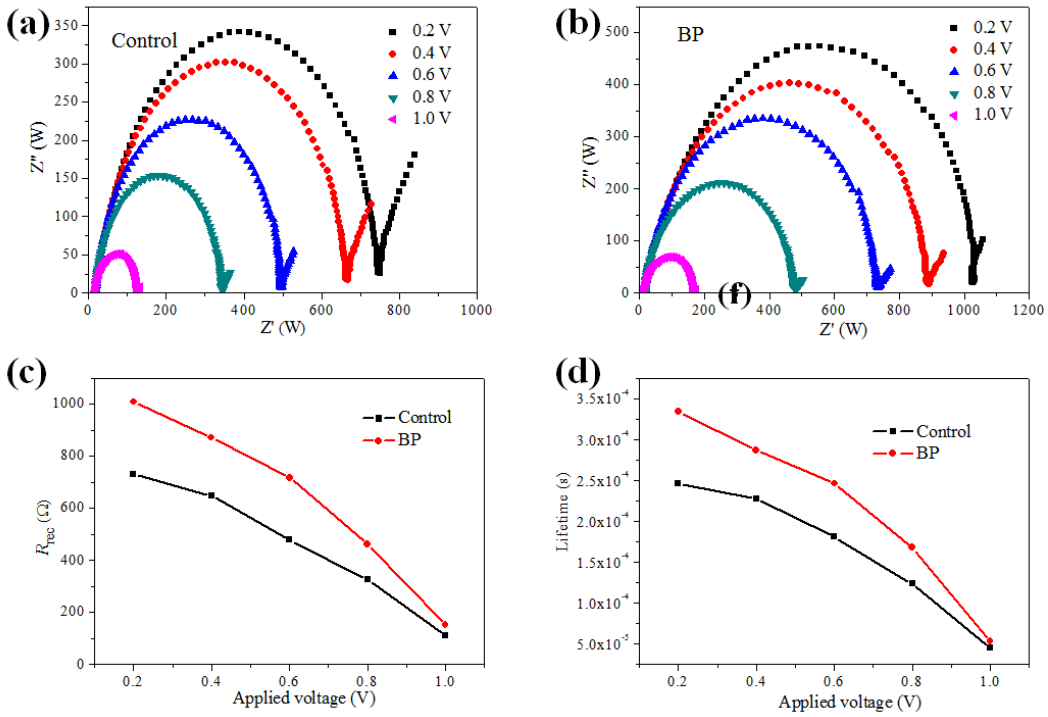

Figure 4.23 (a) and (b) EIS spectra of control and BP modified devices measured at different bias voltages under light illumination of 100 mW/cm^2. (c) and (d) The recombination resistance and carrier lifetime of perovskite solar cells derived from impedance spectra under different bias voltages under light illumination of 100 mW/cm^2.

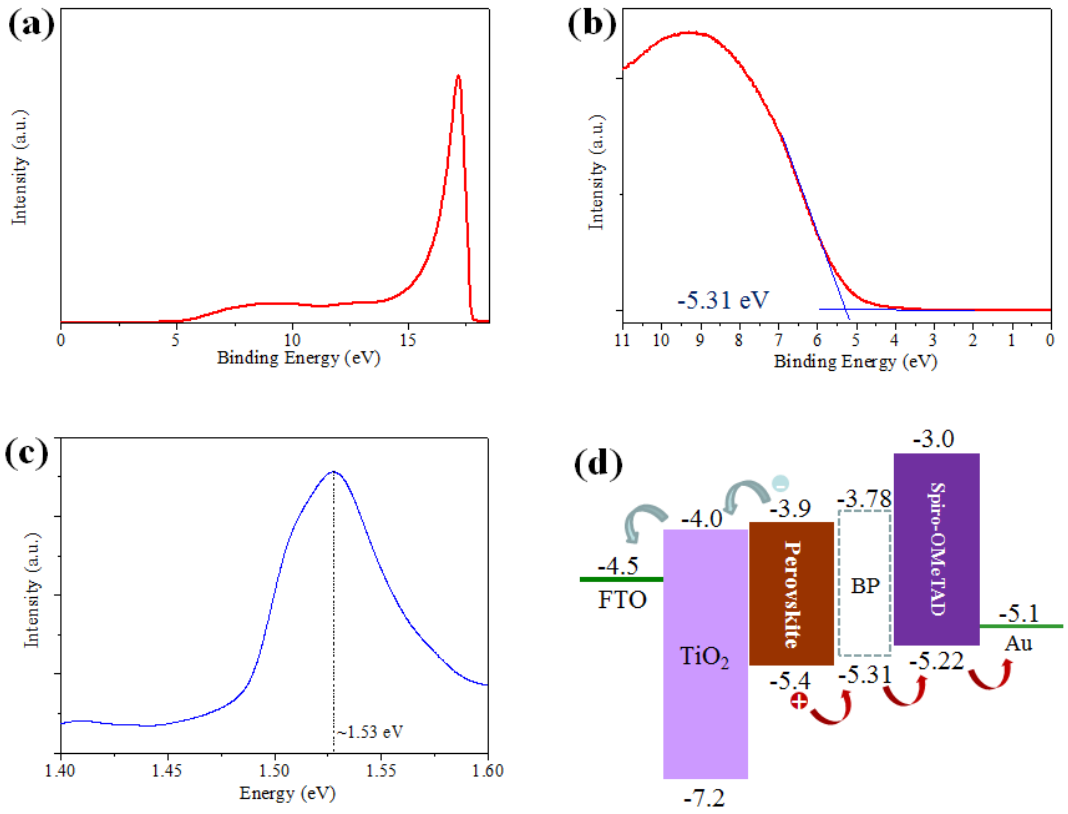

Figure 4.24 (a) UPS spectra of BP film on silicon substrate. (b) The near E_f region of the UPS spectra. (c) PL spectrum of BP film on Si/SiO_2 substrate (300-nm SiO_2). (d) The energy-level band diagram of the BP-modified perovskite solar cells with normal structure.

The introduction of BP thin film at the interface between perovskite and HTL may affect the interfacial band alignment, which is also of great importance to the charge transfer dynamics. Thus, ultraviolet photoelectron emission spectra (UPS) of BP thin film on silicon substrate were obtained, as shown in **Figure 4.24a**. The near Fermi level (E_f) region of the spectra were shown in **Figure 4.24b**. The valence band maximum (VBM) of BP was found about -5.31 eV. Based on the PL spectrum of BP dispersion as shown in **Figure 4.24c**, the band gap of BP thin flakes was estimated around 1.53 eV. Therefore, the conduction band minimum (CBM) of BP thin film was calculated to be -3.78 eV. The schematic energy level band diagram of perovskite solar cells with normal structure

(glass/FTO/cp-TiO_2/mp-TiO_2/perovskite/BP/spiro-OMeTAD/Au) was illustrated in **Figure 4.24d**. The energy levels of all the other materials in the device except for BP were adopted from the literature.[46, 138] It is notable that the VBM of BP (-5.31 eV) matched very well with that of perovskite (-5.4 eV) and spiro-OMeTAD (-5.22 eV), and thus a cascaded band structure was formed with the incorporation of BP flakes, which can not only facilitate hole transport but also reduce the chance of carrier recombination at the perovskite/HTM interface. On the contrary, for perovskite solar cells with inverted structure, the introduction of BP at the perovskite/PCBM interface has little effect on the band alignment condition of the whole device (as shown in **Figure 4.25),** which explains the almost unchanged photovoltaic performance after BP incorporation in inverted structure devices. The energy band diagram comparison of the different kinds of 2D materials were also illustrated in **Figure 4.26** based on the UPS results and references.[122, 132] The UPS spectrum of the MoS2 flakes were shown in Figure 4.27, demonstrating a VBM of ~5.25 eV. Therefore, it was obviously to find that the BP flakes show the best band alignment with the normal device structure.

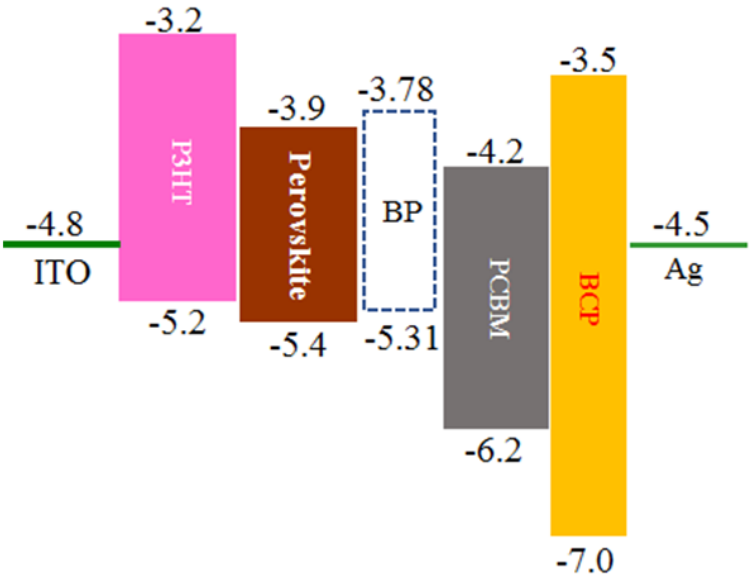

Figure 4.25 Energy-level band diagram of the inverted-structure perovskite solar cells modified with BP flakes.

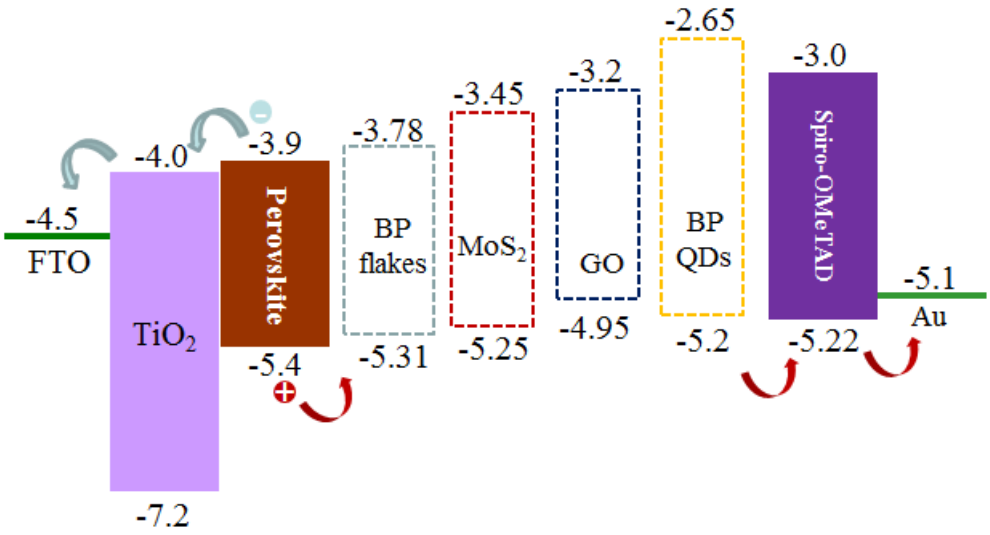

Figure 4.26. Energy-level band diagram of the perovskite solar cells modified with different 2D materials.[122, 132]

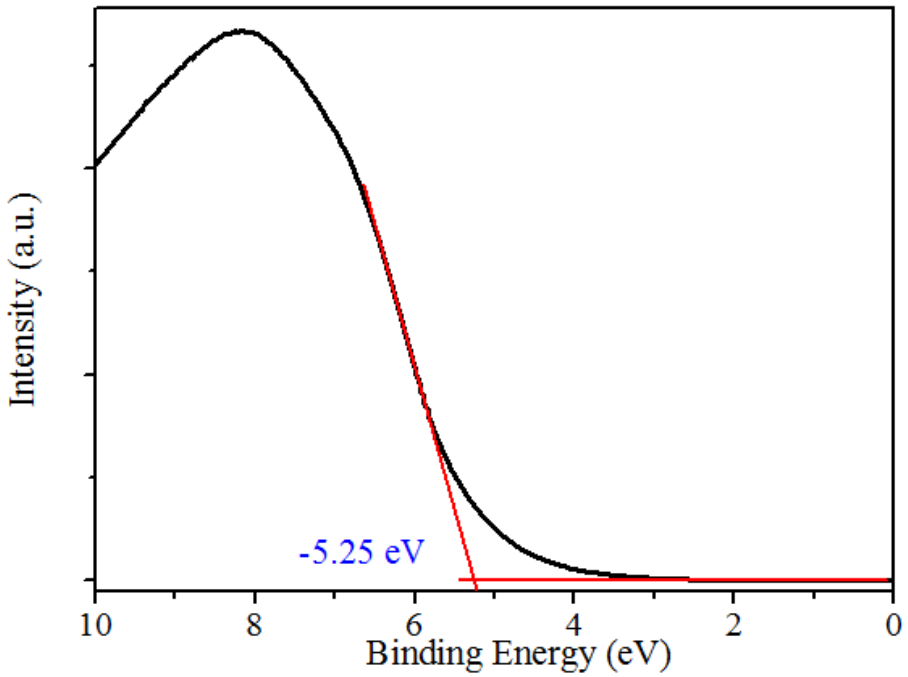

Figure 4.27 UPS spectrum of MoS_2 film on silicon substrate.

Based on the above studies, we conclude that the role of BP thin flakes in improving charge collection includes several aspects. Firstly, the BP thin flakes with superior hole mobilities can work as an effective hole conducting bridge that enhanced the hole extraction and injection from the perovskite to spiro-OMeTAD. Secondly, the

reduced recombination centers and trap-assisted recombination loss at the perovskite/spiro-OMeTAD interface after PB modification contribute to the improved hole transport rate at the interface. Thirdly, the cascade energy level of the perovskite/BP/spiro-OMeTAD structure can not only facilitate hole transport but also reduce the chance of carrier recombination at the interface.

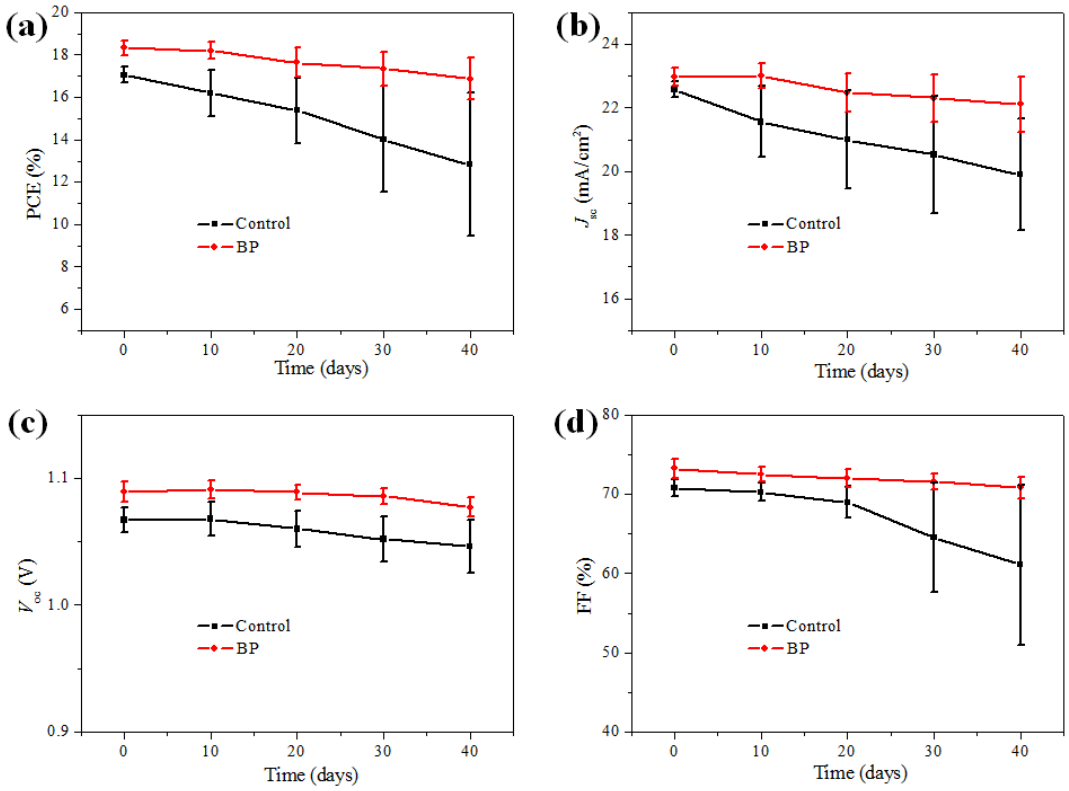

Figure 4.28 Evolution of photovoltaic parameters during stability test (average of 10 devices for each condition). All the devices were encapsulated and kept in air with humidity around 30%.

The stability of the reference and BP-modified devices (10 for each, with a simple encapsulation) was studied by keeping the devices in air with humidity of around 30%. *J-V* curves of the devices were measured every 10 days. The statistical data of the PCEs after 40 days' degradation was plotted in **Figure 4.28**. Apparently, the devices with BP incorporation were much more stable than the reference devices. It was noticed that the BP-modified devices maintained about 92% of its initial

average efficiency, while the reference devices retained only 76% of the original value. In addition, the PCE deviation of the control devices increased greatly during the degradation process while the BP-modified devices showed little change in deviation. It was found that the degradation of the control devices was mainly ascribed to the rapid decrease in J_{sc} and FF, while the BP modified devices showed much slower degradation rates in both Jsc and FF. The improved stability of the device after the incorporation of BP are likely attributed to the passivation effect of the BP flakes, which prevents the ionic migration between the perovskite and the spiro-OMeTAD layers and reduces the shunting pathways.[123] Moreover, the presence of BP buffer layer could suppress the perovskite degradation induced by the additives (like Li-TFSI and 4-tert-butylpyridine, which are needed to increase the hole conductivity of spiro-OMeTAD) in spiro-OMeTAD film.[122] It is noted that although the phosphorus material is prone to undergo degradation upon exposure to ambient air, the BP flakes at the perovskite/HTM interface seems to be relatively stable, which is probably ascribed to the protection by the upper HTL and top electrodes as well as the proper encapsulation.

4.4 Summary

In summary, we have introduced the utilization of few-layer BP flakes with high carrier mobilities as an effective interfacial buffer layer at the perovskite/HTL interface in normal-structure PSCs. The ultrathin BP nano-flakes, prepared by liquid phase exfoliation and dispersed in anhydrous IPA, were deposited on top of perovskite films by dripping deposition. The photovoltaic performances were greatly enhanced after BP modification, due to the better band alignment, improved charge transport and reduced recombination loss at the perovskite/HTL interface. Besides, the device stability was also significantly improved due to the passivation effect of the BP flakes.

Our results pave the way towards the implementation of BP thin flakes as an effective perovskite interfacial layer to boost the device performance.

Chapter 5 Controllable Crystallization of Organometal Halide Perovskite Films with Robotic Laser System

5.1 Introduction

Photovoltaics, being a promising renewable alternative to fossil fuels, can alleviate the energy crisis and avoid environmental pollution in the world. Organometal halide PSCs have attracted tremendous attention in recent years due to their significantly high and increasing PCE along with low fabrication cost. The unique properties of the organometal halide perovskites, including a tunable bandgap, a high absorption coefficient, a broad absorption spectrum, high carrier mobilities and long carrier diffusion lengths, which are responsible for the high photovoltaic performance. Since the first successful fabrication of PSCs with a PCE of 3.8% in 2009, the efficiency now has been improved to 22.1% [2-4, 30, 44, 53, 55] However, the reported PCEs are still much lower than the theoretical value mainly due to some defects existing in the perovskite films that induce trap-assisted recombination of carriers. For the $CH_3NH_3PbI_3$ perovskite with a bandgap of ~1.55-1.6 eV, the maximum PCE would be ~31% according to the Shockley–Queisser limit.[139] Hence, there is a large room to enhance the PCE of the PSCs, which requires the development of novel fabrication techniques to get high-quality perovskite films with fewer defects.

Grain size and crystalline quality in perovskite films are the most critical factors influencing the performance of PSCs. A large number of publications have

demonstrated that enlarging the grain size of a perovskite film can suppress charge trapping, improve the device stability and eliminate the hysteresis in the resulting PSC.[56, 57, 63, 65, 140-142] Larger grains have a lower density of trap states and higher carrier mobilities, which can reduce the recombination of photogenerated carriers propagating in the perovskite layers. These effects are critical to the V_{oc}, J_{sc} and FF of a solar cell, as shown by many experiments. For example, Xiao *et al.* prolonged the charge-recombination lifetime from 1.7 μs (using thermal annealing as the control) to 7.2 μs by increasing the grain size up to 1 μm using solvent annealing method. The corresponding PCE was improved relatively by 57%.[140] Incorporating additives into the perovskite precursor is a frequently used method to increase the crystal size. Ke *et al.* significantly increased the grain size (from 100-400 nm to 2 μm) of perovskite films by adding a tiny amount of lead thiocyanate ($Pb(SCN)_2$) to the perovskite precursor. Consequently, the efficiency was improved from 15.57% to 18.42%.[63] Zhang *et al*. demonstrated that the addition of hypophosphorous acid (HPA) in the perovskite solution can greatly enhance the film quality by enlarging the average grain size from 168 to 769 nm, resulting in an efficiency enhancement from 13.2% to 16.2%.[141] Wu *et al.* exhibited the highest FF of 85% and a PCE of 18% by adding a small amount of water into the precursor solution to produce a large grain size.[57] Nie *et al*. demonstrated a easy hot-casting technique to grow high-quality films with millimeter-scale perovskite grains. Due to the reduced bulk defects and improved charge carrier mobilities, a high efficiency of approximately 18% was achieved.[65] Yang *et al.* grew perovskite films with a large grain size and a high crystalline quality on non-wetting hole transport layers and achieved PCEs up to 18.3%.[56] Recently, Li *et al.* adopted vacuum-flash treatment to improve the perovskite crystallinity and grain size, leading to the maximum efficiency of 20.5% in a device with an area exceeding 1 cm^2[142]

However, the aforementioned approaches to get high-quality perovskite thin

films are all based on thermal annealing processes at temperatures of around 100 °C, which limits the working area, geometric shape, material choice and mass production of PSCs. In particular, it is a great challenge to control the thermal annealing condition of devices on curved surfaces, bulky or large-area substrates due to the difficulty of achieving a uniform surface temperature. Some substrates, especially plastic ones, can only tolerate temperatures below 100°C. Therefore, a novel crystallization approach is desired to overcome the limitations of the existing techniques and produce high-quality, large-area PSCs on any surfaces.

Annealing process by scanning a laser beam on surfaces is an alternative approach to the traditional thermal-annealing process and has been successfully used in the semiconductor industry for the mass production of large-scale devices. Laser-annealing provides numerous advantages over thermal-annealing methods: (i) Laser's localized energy distribution decreases thermal diffusion to other layers, leading to low-temperature processing for device fabrication.[143-145] (ii) The temperature of the sample surface is controllable via tuning the laser output power as well as the laser engagement time.[146] (iii) A uniform temperature distribution can be established on large-area samples by scanning the laser spot, which can hardly be realized with other heating methods. It is also notable that a suitable temperature gradient is favorable for crystal growth.[147-149] (iv) The non-contact feature of the laser annealing method can eliminate the potential chemical contamination that may occur in contact heating approaches.[150] (v) Using an advanced robotic system, the laser annealing approach can be applied to industrial grade mass production with high stability.[151] (vi) Complex patterns can be produced by scanning the laser spot in a programmable path with computer-aided designs.[152]

Particularly, laser-annealing can be used to achieve controllable crystallization of thin films by tuning the power and the scanning conditions of laser beams. A good

example of this is the fabrication of polycrystalline silicon thin-film transistors for large-area displays by laser annealing.[144, 153, 154] Large-grained polycrystalline Si films can be fabricated at room temperature through a sequential lateral solidification (SLS) process,[155, 156] which is based on the accurate control of the scanning speed of the linear laser on the surface to match the growth rate of Si crystals. Consequently, Si with grain sizes of tens of micrometers can be produced, leading to very low trap densities and high carrier mobilities in the film.[156] Laser processing for inorganic solar cells have also been reported.[157-160] Moreover, the laser-induced amorphous to crystalline phase change has been widely used in optical recording technology, including in CD, DVD and Blue-ray media.[161] The as-prepared thin films on the recording layer behave as amorphous materials, which can be converted to crystalline spots by controllable laser annealing.[162] The amorphous and crystalline laser-written patterns represent 0 and 1, respectively. However, there are only few studies on laser annealed PSCs. Jeon *et al.* reported the application of a 1064 nm laser to selectively heat the ITO electrodes of PSCs and realized a PCE of only 11.3%.[163] It is notable that the laser energy was not directly absorbed by the perovskite layer because an as-prepared perovskite amorphous layer has a high optical transmission at the wavelength of 1064 nm, which therefore cannot induce the growth of large perovskite grains. More importantly, laser scanning can induce controllable growth of perovskite grains, which has not been used in the preparation of PSCs until now. In summary, laser scanning is a suitable approach for controlling the crystallization of large-area perovskite films. When the scanning speed of the laser spot can match the growth rate of the perovskite grains, large grains are expected to form in the perovskite films and consequently high-performance PSCs can be fabricated from the films.

In this chapter, we developed a new crystallization approach for perovskite films based on laser beam scanning. The laser-annealing process was optimized by

tuning the laser scanning conditions, including the laser wavelengths, laser scanning speeds and laser power. The obtained high-quality perovskite films with high crystallinity and large grain size contributed greatly to the improved efficiency and stability of devices.

5.2 Devices Fabrication and Characterization

Fabrication of perovskite solar cells (PSCs)

The PSCs were fabricated through a facile solution process with a standard configuration of glass/FTO/block-layer TiO_2 (bl-TiO_2)/mesoporous TiO_2 (mp-TiO_2)/perovskite/spiro-OMeTAD/Au.

Preparation of TiO_2 films. The patterned FTO glass (~14 Ω/□) was bought from the market. Before spin-coating of the bl-TiO_2 layer, the FTO substrates were firstly cleaned with soap water and distilled-water, ultrasonically cleaned sequentially in acetone, distilled-water, and IPA, dried with nitrogen gas flow, and kept in an oven (~80ºC) to remove the moisture on the substrate surface. The FTO substrates were treated with O_2 plasma for 5 min, and then a thin bl-TiO_2 film (20 ~ 30 nm) was then deposited onto the cleaned FTO substrates by spin-coating at 4000 rpm from a precursor solution of 0.15 M titanium isopropoxide in anhydrous ethanol (with addition of 1.5 mM HCl from 37 wt% hydrochloric acid). The as-deposited film was annealed at 80 ºC on hot plate for 10 min before sintering at 500 ºC for 60 min in air. After cooling down to room temperature, a mp-TiO_2 layer (~150 nm) was spin-coated on top of bl-TiO_2 at 4000 rpm by using TiO_2 nanoparticle paste (~30 nm, Dyesol 30 NR-D) diluted in butanol (weight ratio 1:7). After spin-coating, the substrates were dried on hotplate at 100 ºC for 10 min and then sintered again at 500 ºC for 60 min in air. After cooling down to room temperature, the substrates were

immersed in a 40-mM clear aqueous solution of $TiCl_4$ for 30 min at 70 ºC, washed with distilled-water and IPA sequentially after cooling down, and sintered again at 500 ºC for 60 min after drying with nitrogen gas flow. Finally, before cooling down to 150 ºC, the substrates were transferred into the glovebox (filled with high purity N_2) immediately to deposit perovskite films.

Preparation of perovskite precursor solution. The CH_3NH_3I (MAI) was bought from Dyesol, and the PbI_2 (99%) was bought from Sigma-Aldrich. The perovskite solution was prepared by dissolving 0.5763 g PbI_2 and 0.1986 g MAI in 1 ml mixed solvents of anhydrous DMF and DMSO (volume ratio, 8:1). It was noted that 5 mol% of CsI was added to the perovskite precursor solution to get a higher device efficiency.

Preparation of perovskite films. The perovskite precursor solution was spin-coated on the mp-TiO_2 films at 4000 rpm for 30 s in glovebox. During the spin-coating process, about 100 µl of chlorobenzene was poured onto the spinning substrate at 10 s after start. For thermal-annealing, the substrates were then annealed on hotplate at 65 ºC for 2 min followed by 100 ºC for 60 min on hotplate in glovebox. For laser-annealing, the as-deposited perovskite films were transferred to a homemade simple glovebox (humidity <10%), where a simple laser scanning system was built as shown in **Figure S1a**. A continuous-wave laser diode was attached on an X-Y moving system driven by 3 stepper motors. The laser beam was pointing at the vertical direction. The laser scanning track patterns were designed with Autodesk AutoCAD software. The CAD files were then transformed to G-code using open-source GRBL firmware and loaded to an open-source Arduino microcontroller. Therefore, the laser beam spot can move on top of the sample surface along the track as shown in **Figure S1b** (the step distance was kept at 0.1 mm)**.** The laser scan speeds can be customized through the software, while the laser output power can be

tuned through an external voltage source meter. All together 3 lasers (with wavelengths of 405 nm, 450 nm and 660 nm) were used in this work. The diameters of the laser beam spots were all set to 0.5 mm. And the laser output power was calibrated with a light intensity power meter every time before experiment. The distance between the laser diode and the sample surface was about 10 cm.

Deposition of hole transport layer and top electrode. After the thermal or laser annealing processes, a spiro-OMeTAD (Lumtec, 80 mg/ml in chlorobenzene) solution was spin-coated on the perovskite films at 4000 rpm for 30 s in glovebox. The spiro-OMeTAD solution (1 ml) was doped with 29 μl 4-tert-Butylpyridine (TBP, Sigma-Aldrich) and 17.5 μl bis(trifluoromethylsulphonyl)imide lithium salt (Li-TFSI, Sigma-Aldrich, 520 mg/ml, dissolved in acetonitrile). The samples were then taken out from the glovebox and kept in dry air (humidity<10%) for around 10 hours. Finally, gold electrode (~ 100 nm) was deposited on top through a shadow mask by thermal evaporation at a pressure of ~ 1×10^{-6} Torr. The active area of each cell was about 8 mm^2. All the devices were then encapsulated with epoxy and glass in glovebox.

Characterization of Perovskite Films

X-ray diffraction (XRD) measurements of perovskite films. An X-ray diffraction system (Rigaku SmartLab) was used to check the crystal structure and crystallinity of the fabricated perovskite films.

UV-visible absorbance measurements of perovskite films. The UV-visible absorbance spectra of the perovskite films were measured with a UV-Vis spectrophotometer (UV-2550, Shimadzu).

Photoluminescence (PL) measurements of perovskite films. The perovskite films for PL measurements were prepared on glass substrates. Both the steady-state and

time-resolved PL measurements of the films were performed by using an Edinburgh FLSP920 fluorescence spectrophotometer. A 636.2-nm laser was used as an excitation light source here (illuminated from the perovskite film side).

Scanning electron microscopy (SEM) of perovskite films. Both plan-view and cross-sectional SEM images were obtained by a JEOL JSM-6335F field emission SEM. All the samples for SEM observations were coated with a ultra-thin layer of gold before put into the microscope.

Characterization of Perovskite Solar Cells

Current density-voltage (J-V) characteristics. The *J-V* curves of the PSCs were measured with a Keithley 2420 source meter under standard 1-sun light illumination of 100 mW/cm^2 (Newport 91160 solar simulator, 300 W, equipped with an AM 1.5 filter). The light intensity was frequently calibrated during the *J-V* test by using a standard reference silicon cell. For a standard sweeping cycle, the external applied bias swept from 1.2 V to 0 V (reverse scan) and then returned to 1.2 V (forward scan). Normally, the voltage scan rate was 30 mV/s. And no preconditioning (such as longtime forward bias or light soaking) was applied before all the measurements.

External quantum efficiency (EQE) measurements. The EQE spectra were obtained by using a standard EQE test system (Newport), consisting of a xenon lamp (Oriel 66902, 300 W), a monochrometor (Newport 66902), a Silicon detector (Oriel 76175_71580), and a dual channel power meter (Newport 2931_C). The measurements were performed in DC mode at room temperature. The light spot is smaller than the active area of the single cell, to make sure that all the light was illuminated on the active area of the cell. The EQE response from wavelength of 300 nm to 800 nm was recorded by a computer.

Stable power output measurements. The stable power output characteristics

were measured near the maximum power point of the PSCs under standard light illumination of 100 mW/cm^2. The steady-state current as a function of time was recorded by a Keithley 2400 source meter, and the stable output efficiency was calculated from the stable current and the bias voltage applied.

Electrochemical impedance spectroscopy (EIS) measurements. The EIS measurements of the devices were carried out under light illumination of 100 mW/cm^2 (white light), by using a Zahner Zennium 40630 electrochemical work station. The oscillating voltage was 50 mV and the applied DC bias voltages varied from 0.2 V to 1.0 V. The frequency of the sinusoidal signal changed from 2 MHz to 1 Hz.

Illumination-Voc and illumination-Jsc measurements. The relationship between V_{oc} (or J_{sc}) and light intensity was recorded by a photo-electrochemical system (the integrated system consisting of the above-mentioned Zahner Zennium 40630 electrochemical work station and a light intensity controlling accessory). The light intensity can be tuned continuously from 0 to 125 mW/cm^2.

Device stability measurements. For stability measurements, all the devices encapsulated with epoxy and glass were kept in air with humidity around 30%.

5.3 Results and Discussion

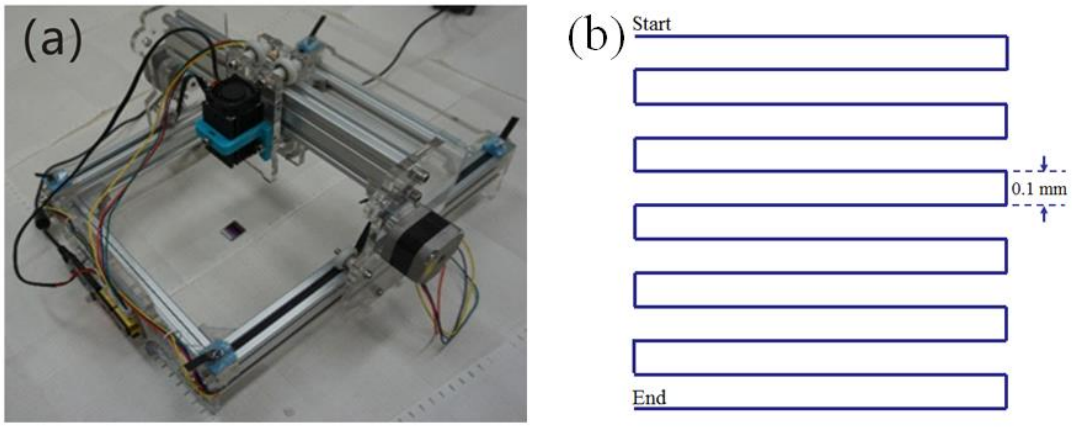

Figure 5.1 (a) Photo of the laser-annealing system controlled by computer software. (b) Illustration of the laser scanning track with a step distance of 0.1 mm.

A homemade robotic laser scanning system (as shown in **Figure 5.1a**) was used to anneal the as-deposited perovskite films by lasers, instead of the traditional thermal-annealing on hotplates. A continuous-wave laser diode with controllable output power was attached on an X-Y moving system driven by 3 stepper motors. The downward laser beam can scan along the designed tracks through the sample surface line by line (as shown in **Figure 5.1b**) under the control of a computer program. **Figure 5.2** shows the schematic illustration of the laser scanning process. The as-deposited perovskite film was light brown, as shown in **Figure 5.3**, indicating that it was partially crystalized. The coexistence of crystalline and amorphous phases in the original film was also confirmed by the (X-ray diffraction) XRD results shown in **Figure 5.4**. After completing the scanning process, the perovskite film turned black the same as the thermal-annealed film, as shown in **Figure 5.3**.

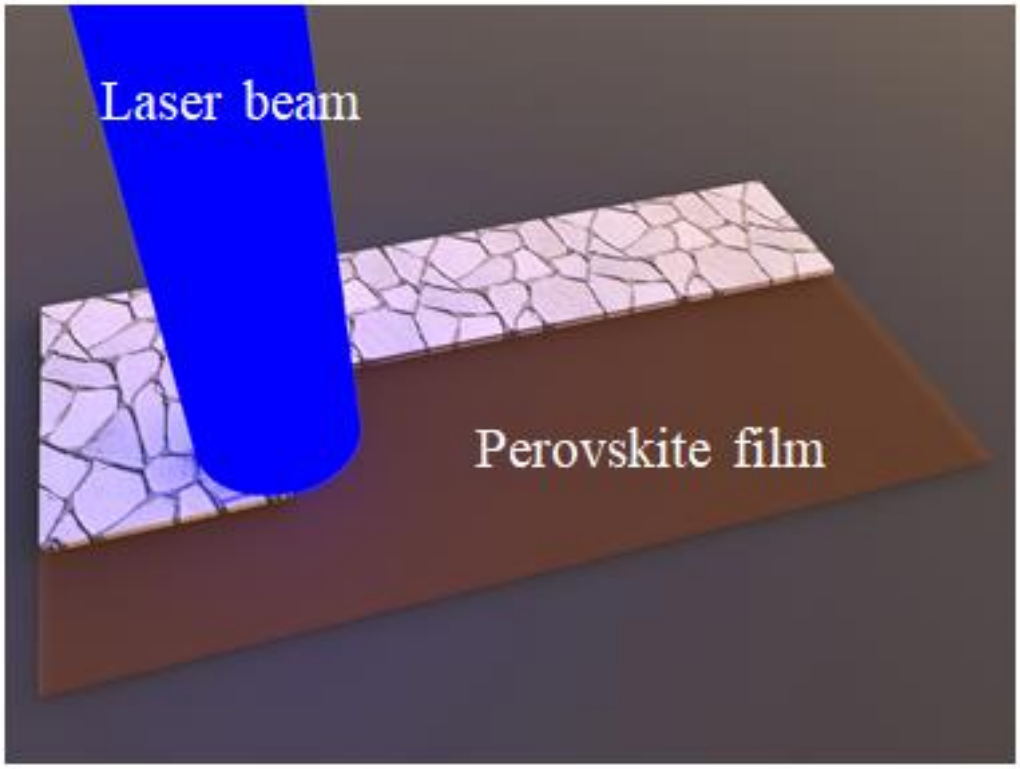

Figure 5.2 Schematic illustration of the laser scanning process.

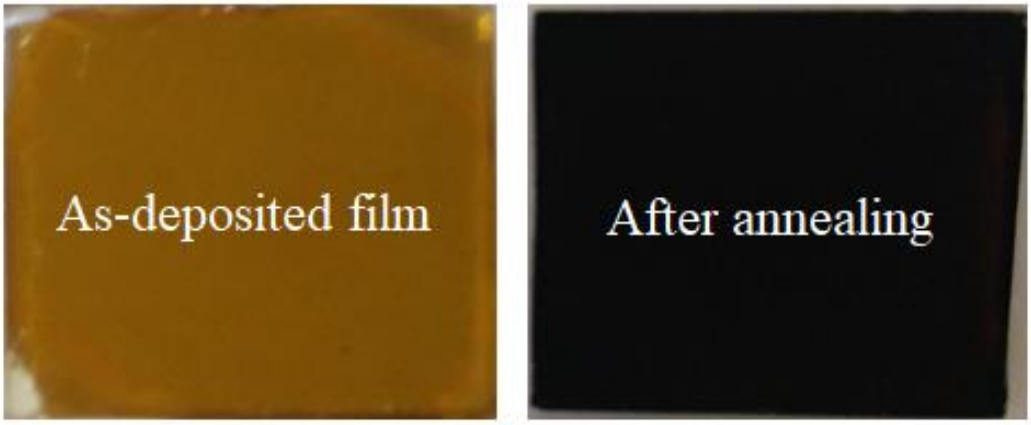

Figure 5.3 Photos of as-deposited (left) and laser-annealed (right) perovskite films.

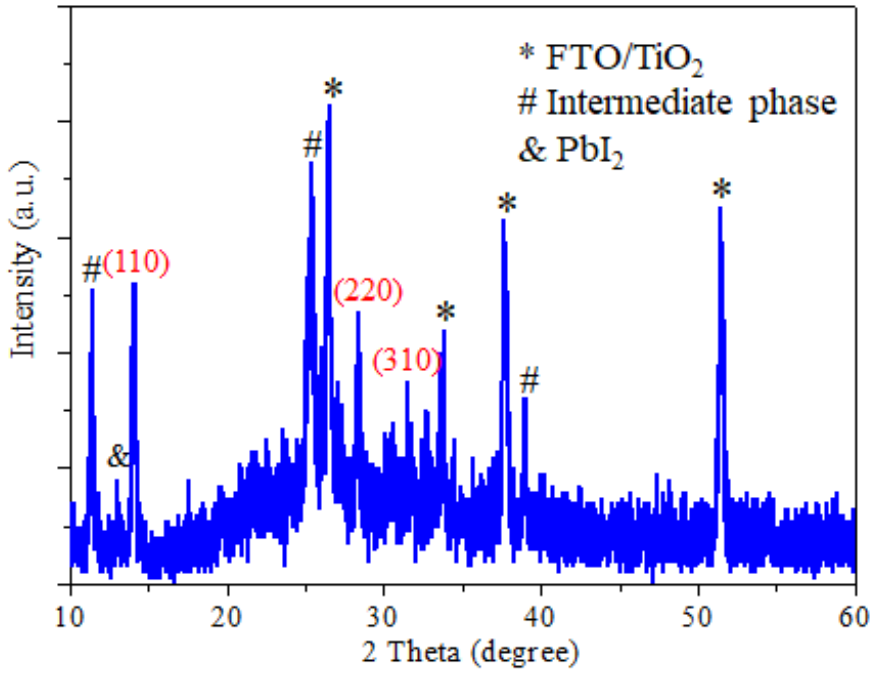

Figure 5.4 XRD spectrum of as-deposited perovskite film, showing the appearance of (110), (220) and (310) peaks of tetragonal $MAPbI_3$ perovskite phase.

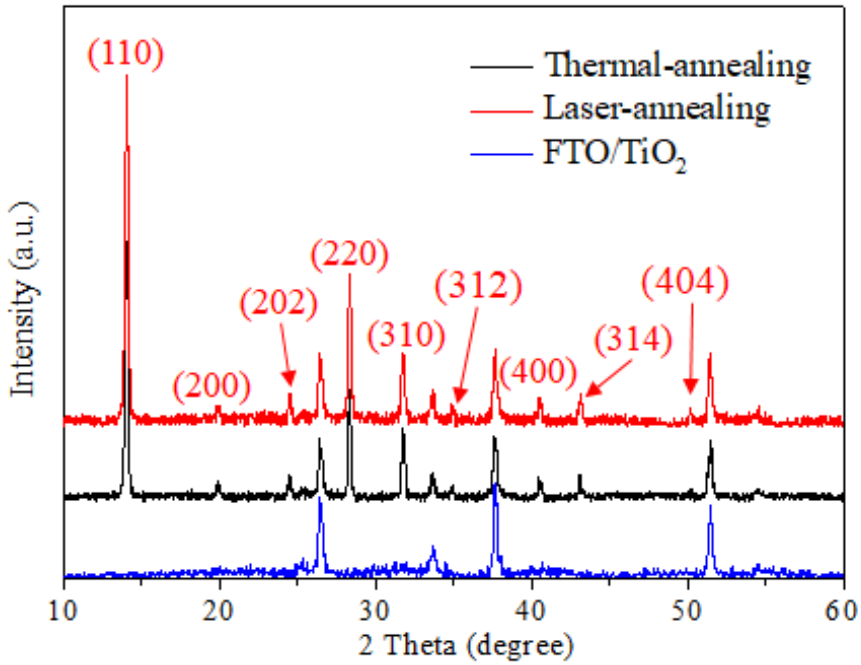

Figure 5.5 XRD spectra of perovskite and FTO/TiO_2 films.

Figure 5.5 compares the XRD spectra of the thermal-annealed and laser-annealed (450-nm laser was used here) films. All the diffraction peaks appear here (apart from those peaks from the FTO/TiO_2 substrate) are corresponding to the methylammonium lead iodide perovskite ($MAPbI_3$) phase with tetragonal crystal structure at room temperature. It was confirmed that both films were well crystalized after the annealing process. By comparing the main diffraction peaks ((110) peak located at around 14.05º) of those two patterns, as shown in **Figure 5.6**, it was found that the laser-annealed perovskite film has a smaller full width at half maximum (FWHM), which means the higher crystallinity of laser-annealed films than the thermal-annealed one. Moreover, we observed that the (110) main diffraction peak, which represents the [110]-oriented grains in the film, shows much higher peak intensity than the other peaks corresponding to the grains of other different orientations. The peak intensity ratios of (110) peak with some other diffraction peaks, as listed in **Table 5.1**, were superior higher for the laser-annealed film, indicating a preferred orientation along [110] direction. For example, the intensity ratio between (110) and (200) peaks was calculated as 12.4 for thermal-annealed film, while it increased to 18.6 for the laser-annealed one. It can be inferred that the high crystallinity and preferred crystallographic orientation of the laser-annealed perovskite film will likely influence the charge dissociation, transport and diffusion length considerably.[4]

Table 5.1 The peak intensity ratios of (110) peak with some other diffraction peaks in Figure 5.5.

Peak intensity ratio	Thermal-annealing	Laser-annealing
$I_{(110)} / I_{(200)}$	11.95	21.36
$I_{(110)} / I_{(202)}$	13.15	16.61
$I_{(110)} / I_{(310)}$	3.65	5.86
$I_{(110)} / I_{(314)}$	13.84	15.74

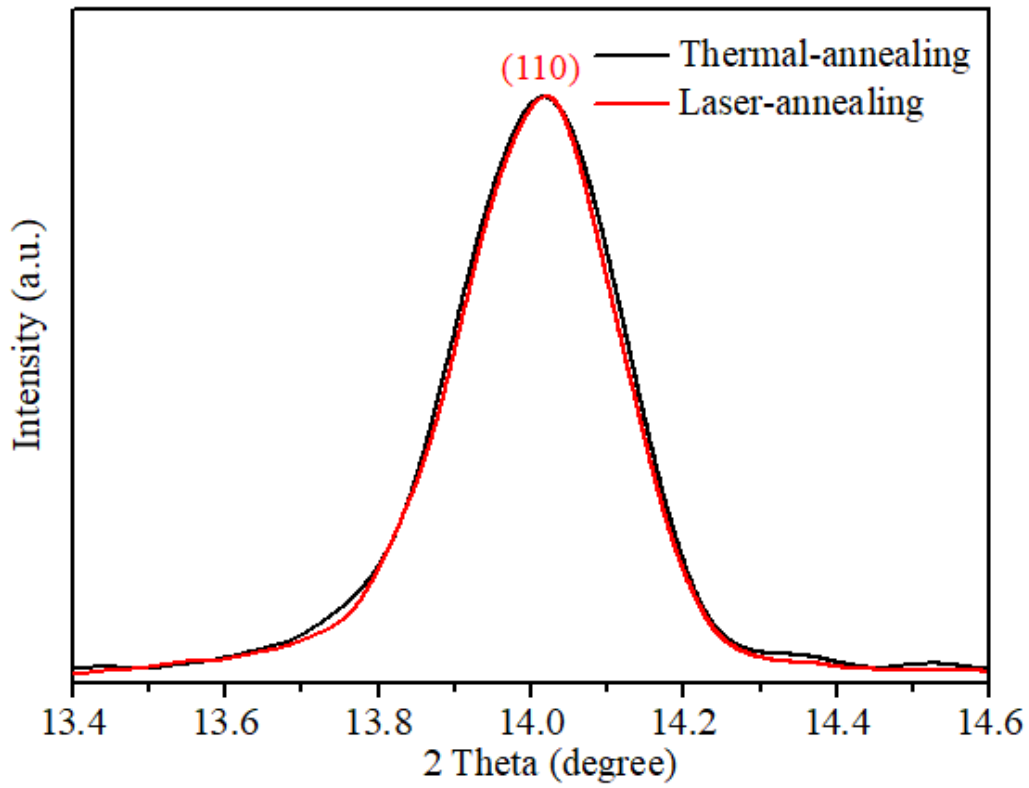

Figure 5.6 (110) diffraction peak of perovskite films. The smaller FWHM (full width at half maximum) of laser-annealed perovskite film means its higher crystallinity than that of thermal-annealed one.

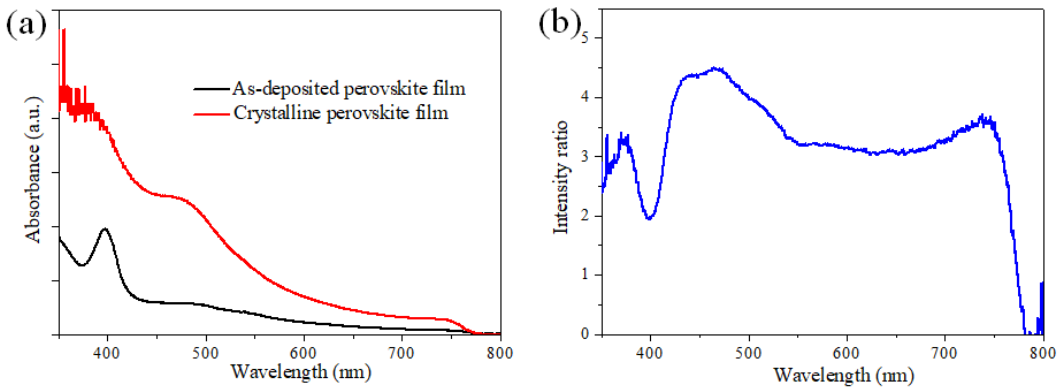

Figure 5.7 (a) UV-vis absorbance spectra for as-deposited and laser-annealed perovskite films. (b) The intensity ratio of the UV-vis absorbance between laser-annealed perovskite film and as-deposited film.

Figure 5.7a shows the UV-visible absorbance spectra of the as-deposited perovskite film as well as the crystalline film after laser-annealing. It was noted that the as-deposited perovskite films before annealing were light brown due to the coexistence of amorphous and crystalline perovskite phases. Because the optical transparency of the amorphous part in the film was quite high, most of the energy of the laser beam should be absorbed by the crystalline portion, which was composed of tiny nanocrystals working as perovskite seeds. That is, the light can be directly absorbed by the perovskite film, rather than by the fluorine-doped tin oxide (FTO) electrode or the TiO_2 film on the backside. Therefore, the existing perovskite seeds could have more energy needed to grow into larger grains, while the chance for more new nucleation become less. However, in terms of thermal-annealing, the heat transferred to the film can be absorbed by both the crystalline and amorphous part, and lots of more new grains may generate in the film upon annealing. Thus, we hypothesize that the laser-annealed perovskite films should be more uniform with larger grain size compared with that of the thermal-annealed ones. Besides, it was also noticed that the intensity ratio of light absorption for the laser-annealed and as-deposited perovskite films varied with the light wavelength, as shown in **Figure 5.6b**. Therefore, the crystallization and morphology of the laser-annealed perovskite films may have close relationship with the laser wavelength.

Through systematical study of the laser-annealed perovskite films by SEM and XRD, we found that the crystallization process and morphology of the perovskite films were greatly related to the laser-annealing parameters, such as the laser wavelengths, scanning speeds and laser output power. Perovskite films of larger grain size have been obtained by optimizing all these parameters systematically.

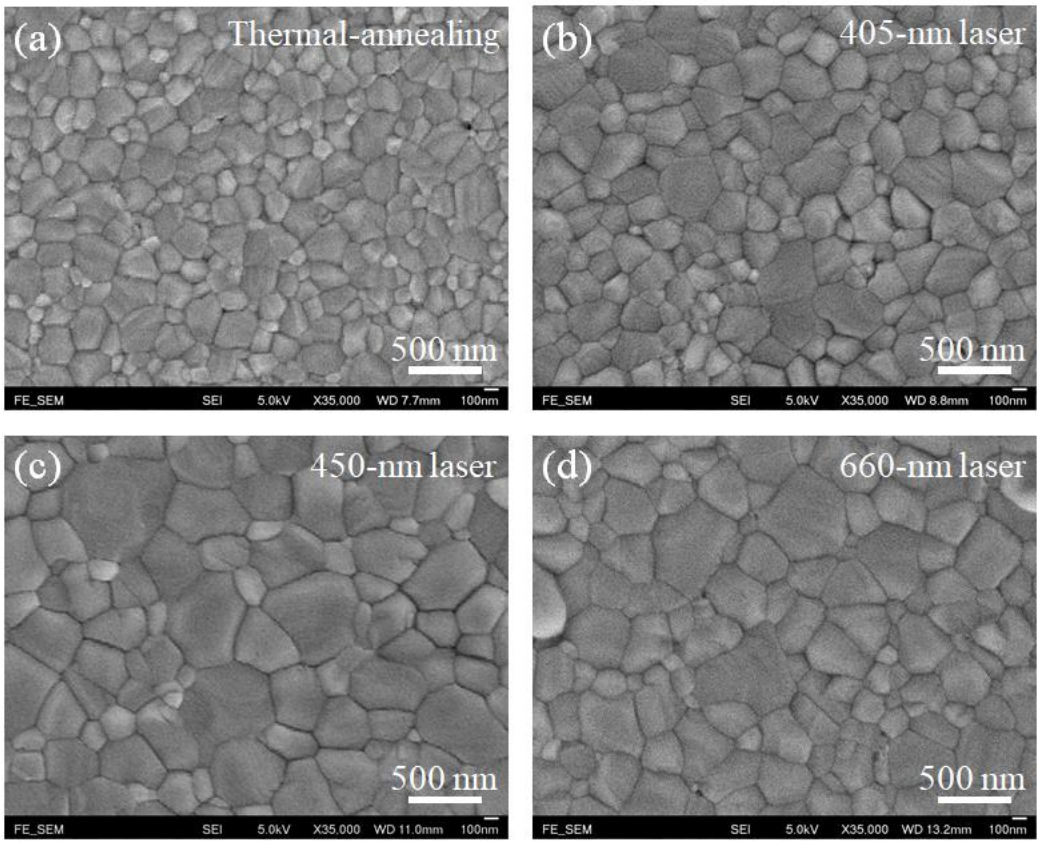

Figure 5.8 Plan-view SEM images of perovskite films fabricated by thermal-annealing (a) and laser-annealing (b-d) processes. 405-nm, 450-nm and 660-nm lasers were used here.

Figure 5.8 shows the plan-view SEM images of the perovskite films fabricated by thermal-annealing and laser-annealing, respectively. Lasers of different wavelengths (405 nm, 450 nm and 660 nm) were attached on the laser scanning system and were driven at the same scanning speeds (25 mm/min) and fixed laser output power (150 mW). The laser beam spots illuminated on perovskite films were always kept constant (0.5 mm). Obviously, the grain size of all the laser-annealed perovskite films was much larger and uniform than that of the thermal-annealed film. It was noteworthy that the morphology of the perovskite films was found to be closely related with the laser wavelengths. The perovskite film annealed with the 450-nm laser had the largest average grain size, followed by the 660-nm laser and the 405-nm laser annealed films. This result was in accordance with the intensity

ratio of light absorption for the laser-annealed and as-deposited perovskite films (see in **Figure 5.7b**), and thus confirmed the relationship between the laser wavelengths and the film morphology. The cross-sectional SEM image of perovskite films shown in **Figure 5.9** (450-nm laser) also demonstrate that most of the perovskite grains were penetrating through the perovskite capping layer, and most of the grain boundaries were perpendicular to the substrate, which were quite beneficial for the charge transport from the perovskite material to the charge collection layers. Moreover, this microstructure also resulted in a reduced surface area of the grain boundaries and a lower overall concentration of defects in the perovskite films, retarding nonradiative charge carrier recombination at the grain boundaries, which enhanced the V_{oc} of the cells, as shown below.[62, 142, 164]

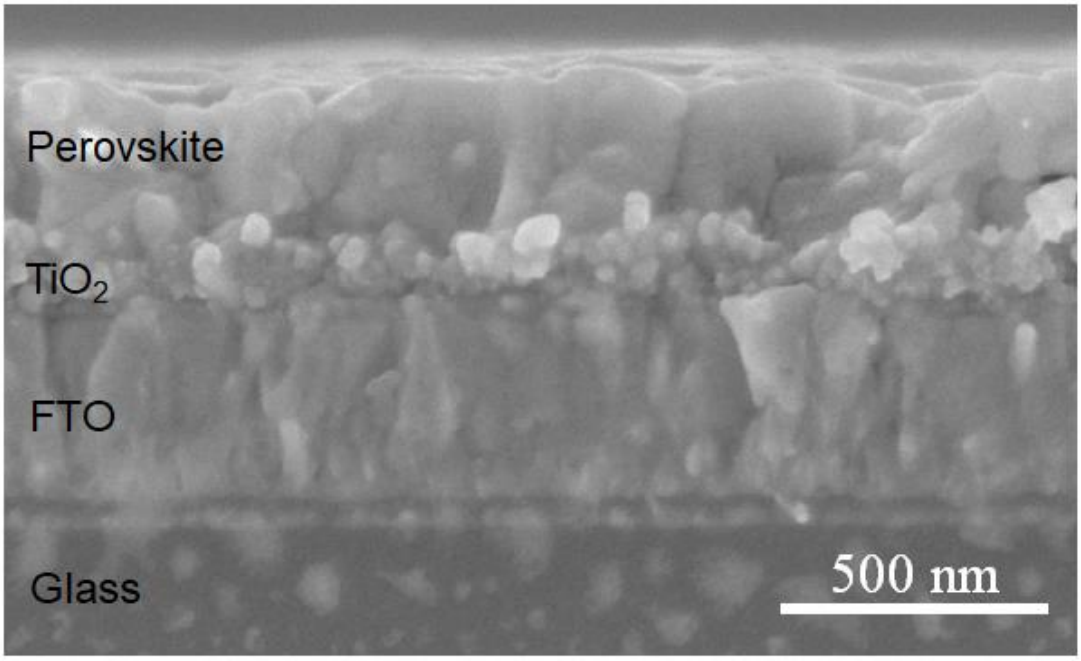

Figure 5.9 The cross-sectional SEM image of perovskite films fabricated by laser-annealing (450-nm laser).

In addition to the laser wavelengths, the laser scanning speeds and laser output power were also strongly associated with the crystallization process and film morphology of the perovskite films, as shown in **Figure 5.10-5.12**. **Figure 5.10**

shows the SEM images of perovskite film annealed by 450-nm laser at different scanning speeds. The laser output power was set at 150 mW as a constant. It was found that some amount of PbI_2 phase appeared on the perovskite surface when the scanning speed was very low (10 mm/min), which can be confirmed by the XRD spectra in **Figure 5.12a**. A clear diffraction peak of PbI_2 appeared at $2\theta=12.6^{o}$ in the 10 mm/min spectrum, indicating that the perovskite films will be partially damaged when the scanning speed is too low. The largest grain size was obtained at a laser scanning speed of 25 mm/min, while the grain size decreased with further increase of the scanning speeds. Moreover, the appearance of PbI_2 peak in the XRD spectrum of 100 mm/min sample also demonstrated that the perovskite film was not well crystallized when the laser scanned too fast. Thus, it was obviously to see that large grains with high crystallinity were expected to form in the perovskite films only when the scanning speed of the laser beam spot can match the growth rate of the perovskite grains. Similarly, the crystallization process of the perovskite films was very sensitive with the laser output power, as shown in **Figure 5.12** (450-nm laser, 25 mm/min). According to the SEM images in **Figure 5.11** and the XRD spectra in **Figure 5.12**, we found that the laser output power of 130 mW and 150 mW gave perovskite films with excellent morphology and crystallinity, while the films annealed at the output power of 110 mW and 170 mW were both found to have residual PbI_2 phase. There was supposed to have unreacted amorphous phase at the perovskite/TiO_2 interface at the laser power of 110 mW, while extra PbI_2 particles were found on the perovskite surface at the high laser power of 170 mW. Therefore, too high laser power will degrade the perovskite films, and too low power cannot completely convert the precursor films to crystalline ones.

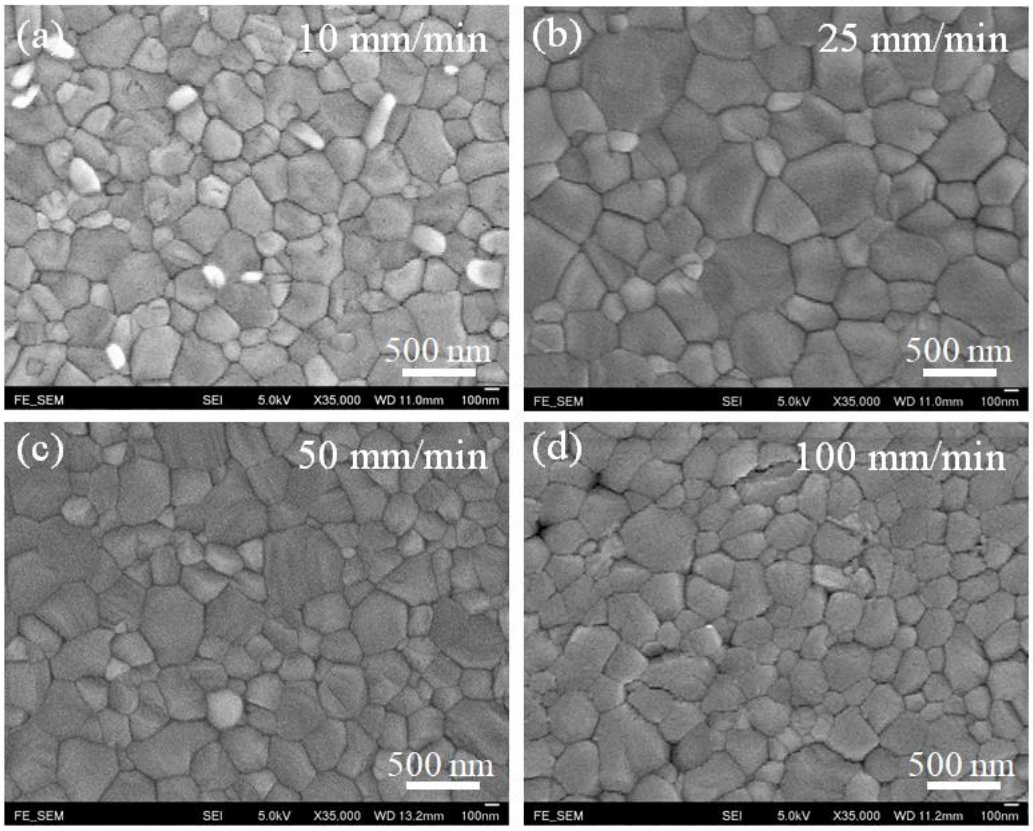

Figure 5.10 SEM images of perovskite films fabricated at different laser scanning speeds.

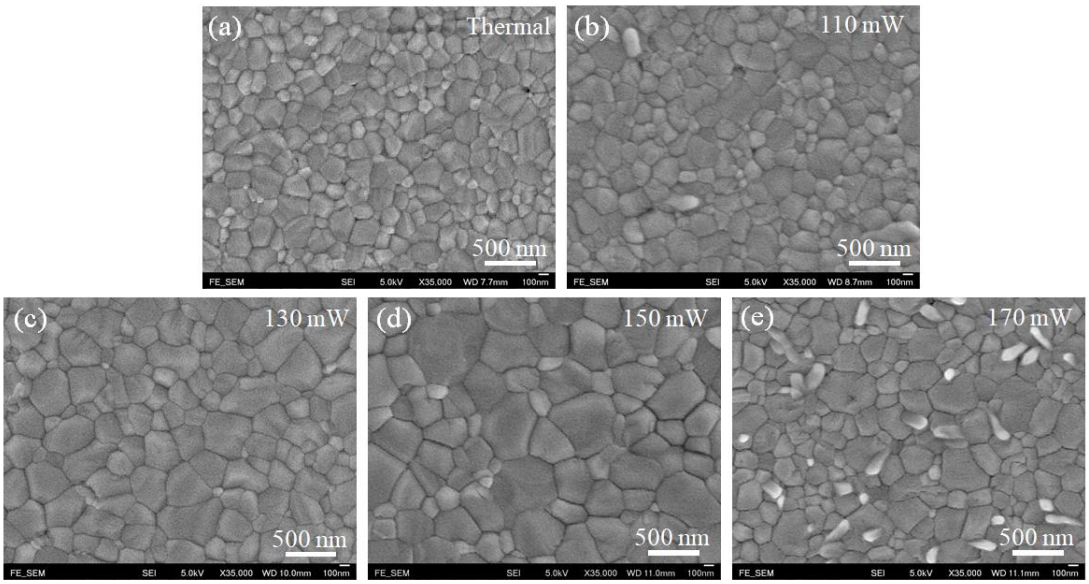

Figure 5.11 SEM images of perovskite films fabricated at different laser output power.

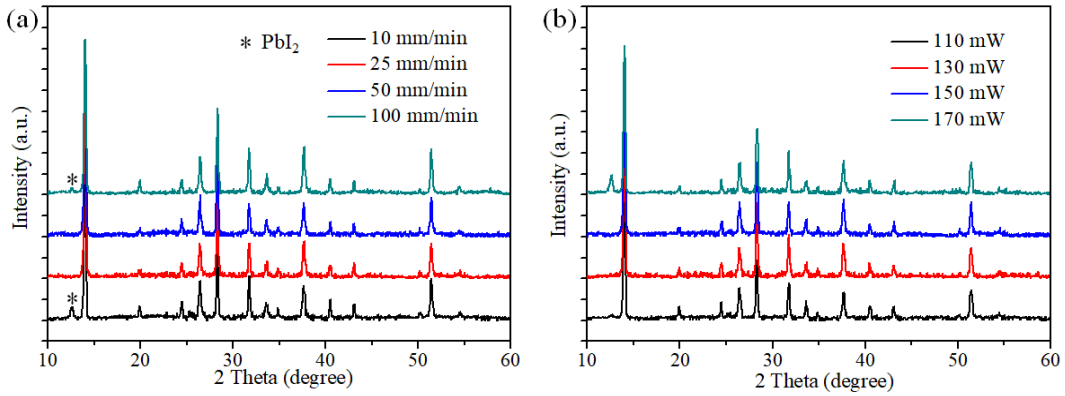

Figure 5.12 XRD spectra of laser-annealed perovskite films at different laser scanning speeds (a) and laser power (b).

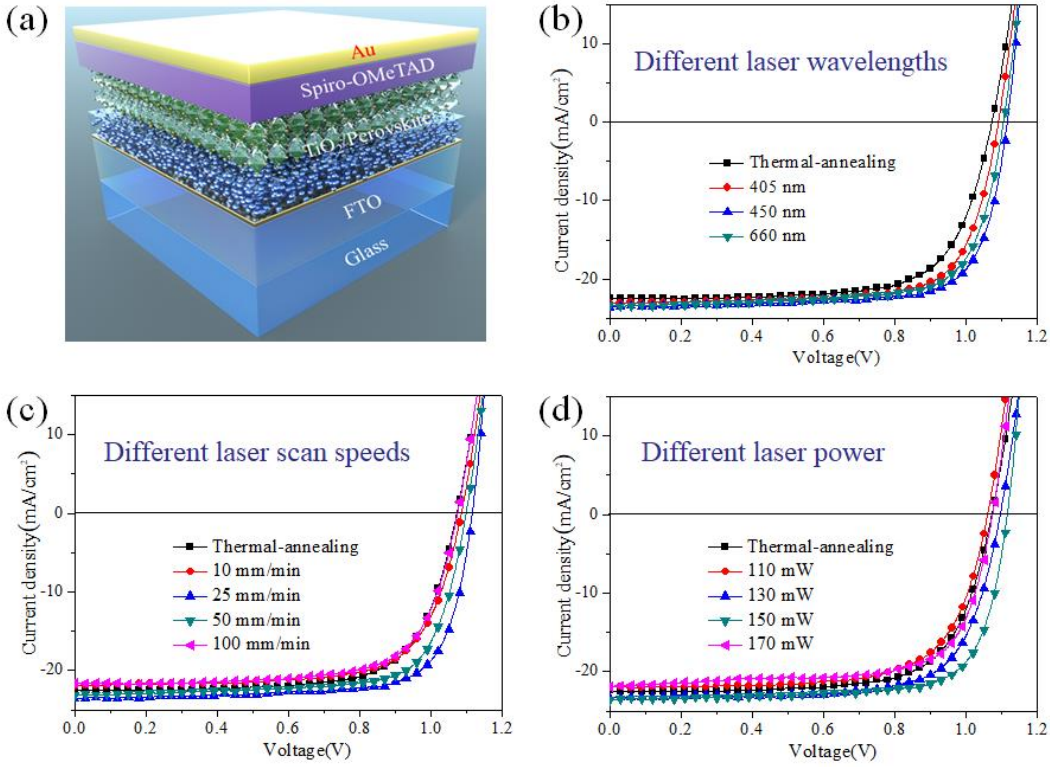

Figure 5.13 (a) Schematic diagram of the device structure of perovskite solar cell, (b-d) *J-V* characteristics of perovskite solar cells fabricated by thermal-annealing and laser-annealing processes. The photovoltaic performance was closely related to the laser scanning parameters, including laser wavelengths, laser scanning speeds and laser power.

We then prepared PSCs with a device configuration of glass/FTO/block layer TiO_2 (bl-TiO_2)/mesoporous TiO_2 (mp-TiO_2)/perovskite/spiro-OMeTAD/Au (as shown in **Figure 5.13a**). **Figure 5.13b~d** shows the standard current density-voltage (*J-V*) characteristics of PSCs based on the perovskite films fabricated by thermal-annealing and laser-annealing processes. The detailed statistical photovoltaics metrics were summarized in **Table 5.2~5.4** (average of no less than 20 cells for each condition). As shown in **Figure 5.13b** and **Table 5.2**, all the photovoltaic parameters were considerably improved for the PSCs fabricated by laser-annealing process (including lasers with wavelengths of 405 nm, 450 nm and 660 nm) compared with that of the control devices. The control devices fabricated by thermal-annealing showed an average PCE of 16.88% with a V_{oc} of 1.07 V, a J_{sc} of 22.38 mA/cm^2, and a FF of 70.6%. In contrast, the 405-nm laser showed an enhanced average PCE of 18.43% with a V_{oc} of 1.09 V, a J_{sc} of 23.16 mA/cm^2, and a FF of 73.0%, exhibiting an 9.2% increase in efficiency. Furthermore, the average efficiency was increased to 19.01% with a V_{oc} of 1.105 V, a J_{sc} of 23.36 mA/cm^2, and a FF of 73.5%, when the 660-nm laser was used. The device performance was maximized when 450-nm laser was adopted, demonstrating an average PCE of 19.29%, a V_{oc} of 1.107 V, a J_{sc} of 23.43 mA/cm^2, and a FF of 74.3%. The greatly improved device performances in all the photovoltaic metrics were attributed to the improved structural and optoelectronic properties (higher crystallinity, larger grain size, lower bulk defects and better charge dissociation and transport property) of laser-annealed perovskite films in comparison with that of the thermal-annealed ones. The increased current density here was well matched with the external quantum efficiency (EQE) spectra shown in **Figure 5.14a**. It was interesting to find that the devices by laser-annealing show higher EQE values than the control devices across almost all the wavelengths range (300 nm ~ 800 nm), although they show small difference in the absorbance curves. This indicate that the laser-annealing approach

can also help improve the charge collection process. Besides, the close relationships between cell performance with the laser wavelengths, as seen clearly, were in consistent with the above-mentioned absorption and SEM data in **Figure 5.7** and **Figure 5.8**.

Table 5.2 Photovoltaic parameters of perovskite solar cells fabricated by thermal and laser annealing (different laser wavelengths) processes.

	Laser wavelengths	**V_{OC} (V)**	**J_{SC} (mA/cm^2)**	**FF (%)**	**PCE (%)**	**Champion PCE (%)**
Thermal-annealing	--	1.067±0.012	22.38±0.47	70.8±1.5	16.93±0.55	18.10
Laser-annealing	**405 nm**	1.090±0.010	23.16±0.39	73.0±1.0	18.43±0.32	19.03
	450 nm	1.107±0.014	23.43±0.41	74.3±1.0	19.29±0.39	20.08
	660 nm	1.105±0.011	23.36±0.36	73.5±1.3	19.01±0.39	19.67

Table 5.3 Photovoltaic parameters of perovskite solar cells fabricated by thermal and laser annealing (different laser scan rates) processes.

	Laser scan rates (mm/min)	**V_{OC} (V)**	**J_{SC} (mA/cm^2)**	**FF (%)**	**PCE (%)**	**Champion PCE (%)**
Thermal-annealing	--	1.067±0.012	22.38±0.47	70.8±1.5	16.93±0.55	18.10
Laser-annealing	10	1.078±0.012	21.98±0.59	70.2±1.6	16.65±0.63	17.57
	25	1.107±0.014	23.43±0.41	74.3±1.0	19.29±0.39	20.08
	50	1.095±0.010	23.17±0.56	73.1±1.3	18.55±0.42	19.35
	100	1.06±0.01	21.86±0.48	71.1±1.4	16.48±0.62	17.61

Table 5.4 Photovoltaic parameters of perovskite solar cells fabricated by thermal and laser annealing (different laser power) processes.

	Laser power (mW)	**V_{OC} (V)**	**J_{SC} (mA/cm^2)**	**FF (%)**	**PCE (%)**	**Champion PCE (%)**
Thermal-annealing	--	1.067±0.012	22.38±0.47	70.8±1.5	16.93±0.55	18.10
Laser-annealing	110	1.065±0.020	22.03±0.37	68.5±1.37	16.11±0.66	16.80
	130	1.095±0.018	23.23±0.51	71.9±1.1	18.28±0.54	19.34
	150	1.107±0.014	23.43±0.41	74.3±1.0	19.29±0.39	20.08
	170	1.082±0.012	21.86±0.45	71.3±1.1	16.87±0.47	17.74

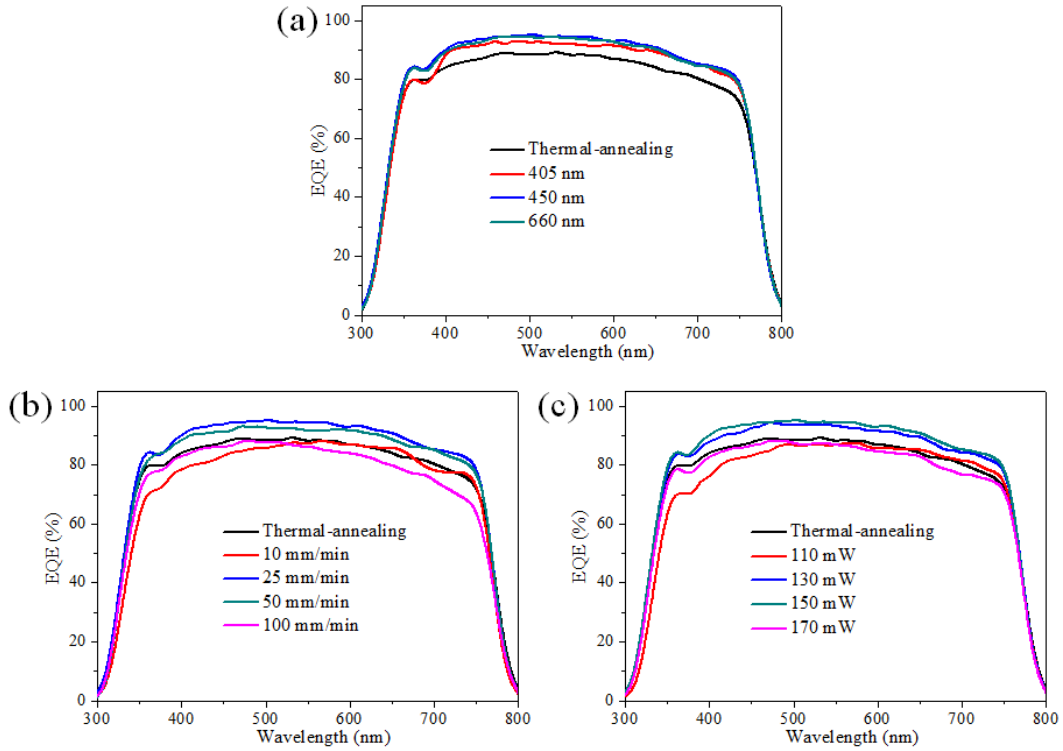

Figure 5.14 EQE spectra of PSCs prepared by thermal-annealing and laser-annealing approaches.

We further investigated the influences of the laser scanning speeds and laser output power on the device performance (450-nm laser, 150 mW), as shown in **Figure 5.13c, 5.13d** and **Table 5.3** and **5.4**. The effects of laser scanning speeds and laser power on the device performance were quite similar. Upon increasing the laser scanning speeds from 10 mm/min to 100 mm/min (or increasing the laser output power from 110 mW to 170 mW), the average PCEs firstly augmented and subsequently decreased with a maximum value of 19.29% at the scanning speed of 25 mm/min and laser power of 150 mW. The average V_{oc}, J_{sc} and FF all demonstrated a similar tendency. This can be explained based on the above-discussed XRD and SEM results. For the low scanning speed of 10 mm/min (or the high laser power of 170 mW), the perovskite surface was partially degraded into insulating lead iodide phase because of the over-irradiation by the laser beam,

which severely affected the crystallinity of the perovskite films and the charge transport at the interface between perovskite and HTL. On the other hand, the high scanning speed of 100 mm/min (or the low laser power of 110 mW) led to an incomplete crystallization of the perovskite film, thus the J_{sc} and PCE of the corresponding devices were all inferior to that of the control devices. **Figure 5.14b and 5.14c** compared the effect of the laser scanning speeds and power on the EQE spectra, which also match well with the *J-V* curves. These results suggest that proper laser scanning speed and laser power are necessary to prepare high quality perovskite films.

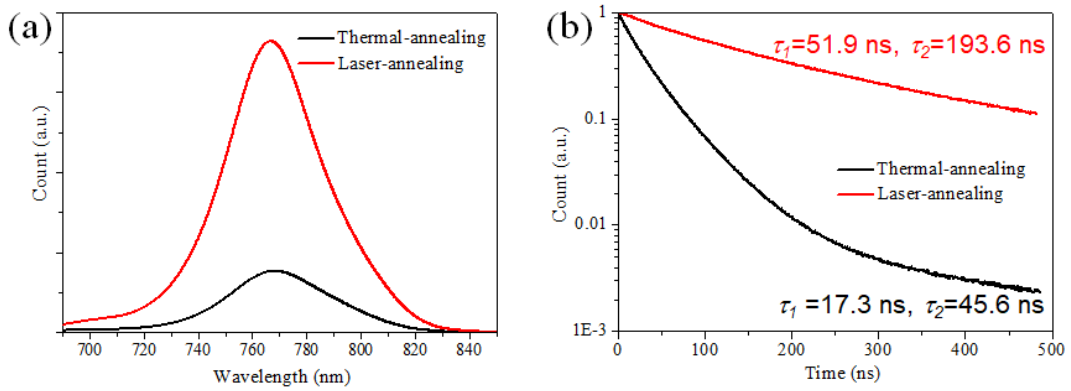

Figure 5.15 Steady-state photoluminescence (PL) spectra (a) and time-resolved PL spectra (b) of perovskite films prepared by thermal-annealing and laser-annealing approaches.

To explore the nature of the outstanding photovoltaic performance of the PSCs prepared by laser-annealing approach, we carried out steady-state and time-resolved PL measurements, as shown in **Figure 5.15**. The perovskite films for PL measurements were fabricated on glass substrates. It was noted in **Figure 5.15a** that the optimized laser-annealed perovskite film exhibited more than three-fold increase in PL intensity relative to that of the thermal-annealed film. Meanwhile, the PL peak demonstrated a slight blue-shift from 768 nm (thermal-annealing) to 766 nm (laser-annealing). The enhanced PL intensity and the blue-shifted PL peak may stem

from the decreased bulk defects in the perovskite absorber, showing reduced charge recombination.[4, 79, 165] To analyze the dynamics of the charge recombination in the perovskite films, time-resolved PL decay measurements were also performed. The PL decays for thermal-annealed and laser-annealed perovskite films were shown in **Figure 5.15b**, indicating a much faster PL decay for the thermal-annealed film. The decay curves were fitted to a biexponential equation: $Y = A_1\exp(-t/\tau_1) + A_2\exp(-t/\tau_2) + y_0$.[4] The fast decay lifetime (τ_1) was attributed to the defect-induced nonradiative recombination, while the slow decay lifetime (τ_2) was ascribed to the radiative recombination.[4, 166] The laser-annealed perovskite film displayed fast and slow decay lifetimes of $\tau_1 = 51.9\,ns$ and $\tau_2 = 193.6\,ns$, respectively. In contrast, the thermal-annealed film exhibited $\tau_1 = 17.3\,ns$ and $\tau_2 = 45.6\,ns$, respectively. The longer PL lifetimes of the laser-annealed perovskite film can be attributed to the decreased concentration defects and traps, and the improved crystallinity, resulting in the dramatic increase in J_{sc} and V_{oc}.[4, 142, 164]

To further elucidate the charge recombination behavior of the full cells, we performed the transient photocurrent and photovoltage measurements. The J_{sc} and V_{oc} as a function of light intensity was shown in **Figure 5.16**. It was noteworthy that the cells fabricated by the optimized laser-annealing process (target devices) exhibited higher J_{sc} and V_{oc} values under any light intensity than that of the cells prepared by thermal-annealing process (control devices), which is in accordance with the higher J_{sc} and V_{oc} values obtained from the above *J-V* curves. For the control device, the V_{oc} value drops rapidly with light intensity in the low intensity region, indicating a predominant trap-assisted recombination process caused by deep-level trap states. In contrast, the target device exhibits almost a constant light intensity-V_{oc} slope across all light intensity tested, suggesting that the laser-annealing approach can effectively reduce the trap-assisted recombination.[120]

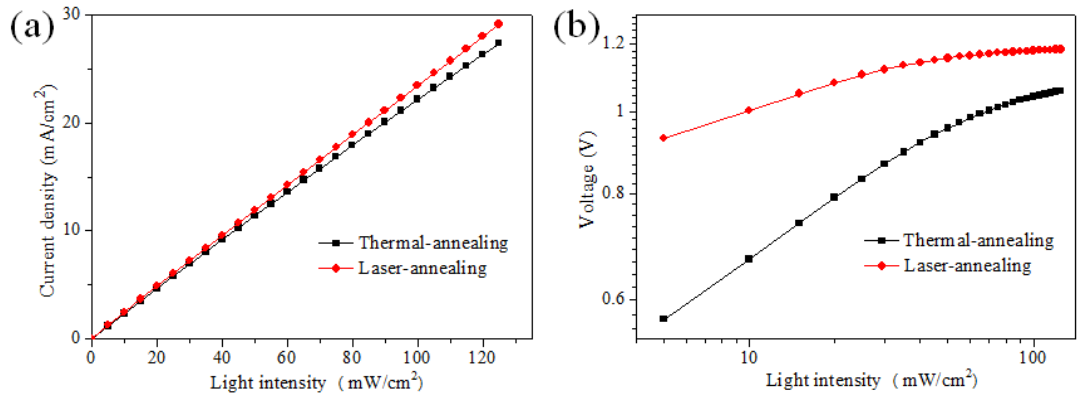

Figure 5.16 J_{sc} and V_{oc} of the perovskite solar cells as a function of light intensity.

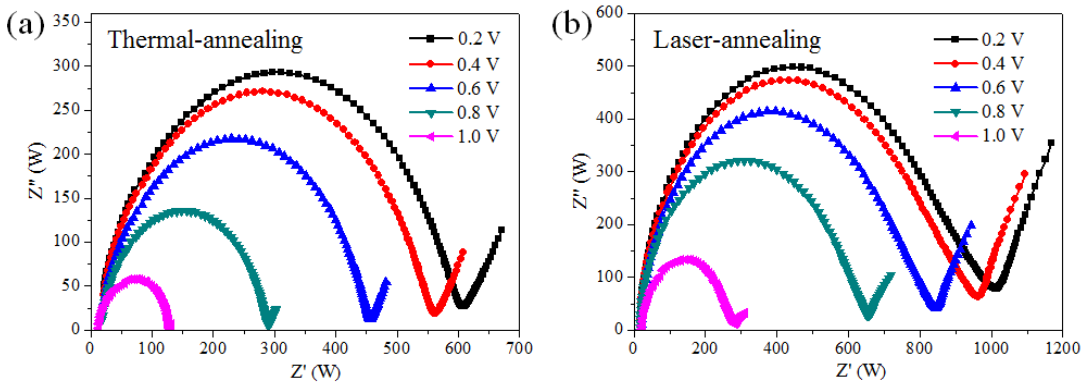

Figure 5.17 Impedance spectra of perovskite solar cells measured at various bias voltages under light illumination of 100 mW/cm^2.

EIS measurements were also carried out on the PSCs under light illumination of 100 mW/cm^2. **Figure 5.17** shows the EIS spectra of the devices at different bias voltages under constant light illumination. Two distinct regimes can be observed in the Nyquist plots shown in **Figure 5.17**: a high frequency regime correlated with the charge recombination process (big half circle), and low frequency regime correlated with slow dielectric and ionic relaxation in perovskite films (small half circle). When a 0.8 V bias voltage was applied, the target device exhibited a much larger R_{rec} (~639.6 Ω) than that of the control device (~271.3 Ω), indicating reduced charge recombination in perovskite films or at the interfaces between perovskite and charge transport layers. **Figure 5.18** shows the recombination resistance (R_{rec}) values at

different applied voltages under light illumination of 100 mW/cm^2 (derived from the impedance spectra in **Figure 5.17**). It was noted that the R_{rec} was larger for the target device at any bias voltage than the control device, indicating a slower recombination rate in the target device, which can be attributed to the lower density of trap states in the laser-annealed perovskite film as evidenced by the above measurements. Furthermore, the increased R_{rec} will contribute to the shunt resistance of the solar cells, which is the main reason for the increased FF of the target devices.

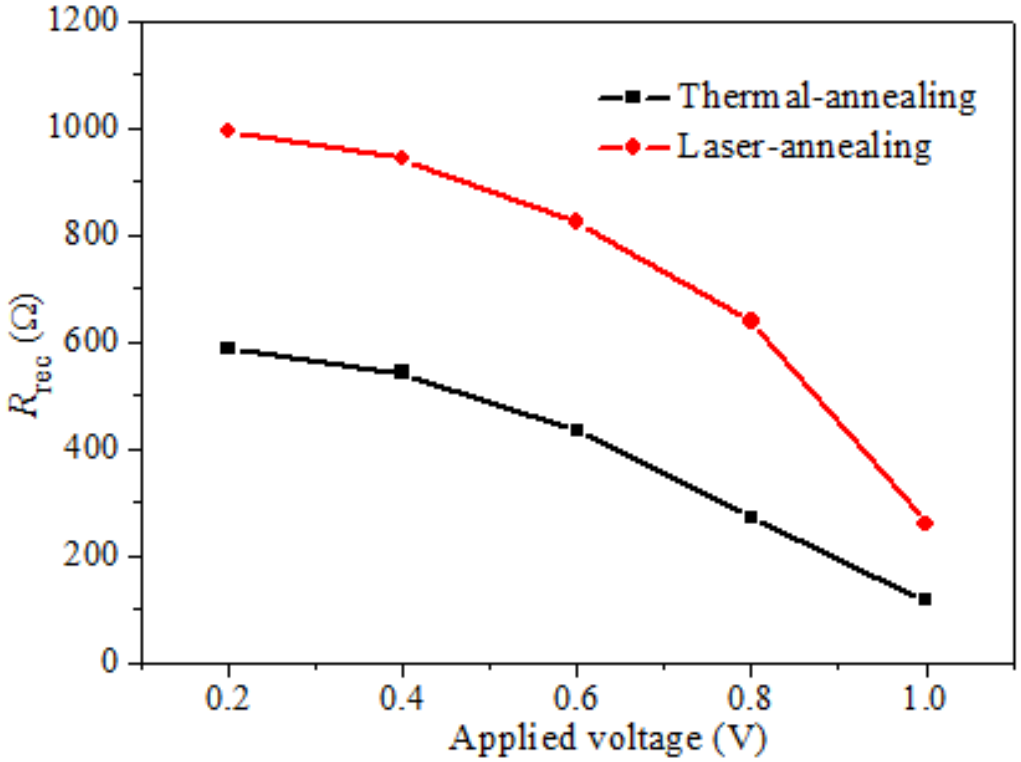

Figure 5.18 The recombination resistance of perovskite solar cells derived from impedance spectra under different bias voltages under light illumination of 100 mW/cm^2.

On the basis of the above results, we optimized the fabrication procedure to further enhance the device performance of the PSCs using the optimized laser-annealing parameters. **Figure 5.19a** shows the *J-V* curves of the champion devices by thermal and laser annealing, respectively. The champion control device, with thermal-annealing method, has a PCE of 18.10%, V_{oc}=1.09 V, J_{sc}=22.62

mA/cm^2 and FF=73.4% obtained from the reverse *J-V* scan (see **Table 5.5**). However, the efficiency is much lower (14.99%) when measured from the forward *J-V* scan, showing large *J-V* hysteresis. In contrast, the champion device by laser-annealing shows much smaller *J-V* hysteresis, achieving a PCE of 20.08%, V_{oc}=1.14 V, J_{sc}=23.42 mA/cm^2 and FF=75.2% obtained from the reverse scan, and a PCE of 18.90%, V_{oc}=1.15 V, J_{sc}=23.42 mA/cm^2 and FF=70.2% obtained from the forward scan, demonstrating much higher photovoltaic performance and smaller hysteresis, which should be attributed to the much more uniform perovskite film with larger grain size and fewer defects. It is noteworthy that the open-circuit voltage of 1.15 V is already quite high for PSCs based on the methylammonium lead iodide ($MAPbI_3$) perovskites. **Figure 5.19b** shows the corresponding EQE spectra, demonstrating an improved quantum efficiency at almost the whole wavelength range for the target device. The integrated circuit from the EQE spectra, as shown in **Figure 5.20**, is in good agreement with the J_{sc} from the *J-V* curves in **Figure 5.19a**. For the target champion device, a steady-state efficiency of 19.52% was achieved measured at the maximum power point of 0.96 V, as provided in **Figure 5.19c**. Besides, we also collected the statistical data of devices prepared by using the optimized laser-annealing and thermal-annealing approaches, respectively (as shown in **Figure 5.19d,** 40 control devices and 40 target devices were fabricated and tested.). The target devices have an average efficiency of 19.29%, which is much higher than that of the control devices (16.93%). It was also noticed that the PCEs of the target devices distributed in a narrow range from 18.38% to 20.08%, showing better reproducibility.

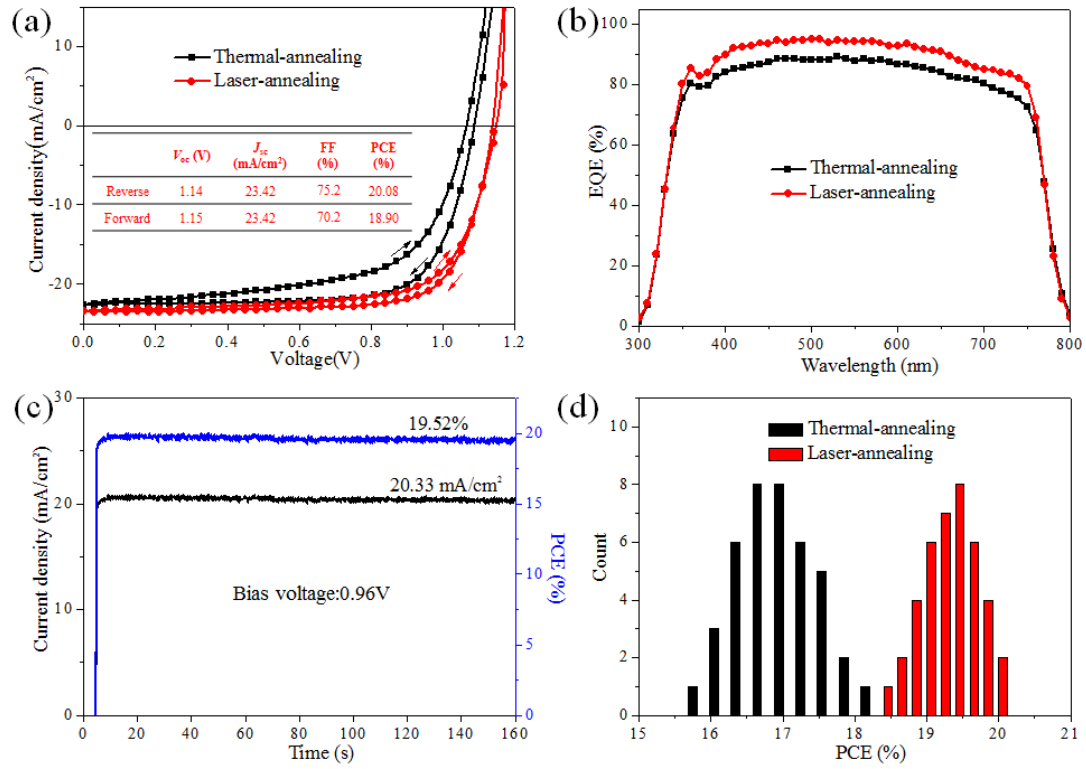

Figure 5.19 The *J-V* curves (a) and EQE spectra (b) of the champion perovskite solar cells fabricated by thermal-annealing and laser-annealing approaches. (c) Steady-state photocurrent and efficiency measured at a bias voltage near the maximum power point (0.93 V). (f) Histogram of PCEs derived from the Reverse scans of 40 devices fabricated at the optimized conditions.

Table 5.5 Photovoltaic parameters of champion perovskite solar cells fabricated by thermal and laser annealing processes.

Annealing methods	**Scan directions**	**Voc (V)**	**Jsc (mA/cm²)**	**FF (%)**	**PCE (%)**
Thermal annealing	Reverse	1.09	22.62	73.4	18.10
	Forward	1.065	22.62	62.2	14.99
Laser annealing	Reverse	1.14	23.42	75.2	20.08
	Forward	1.15	23.42	70.2	18.90

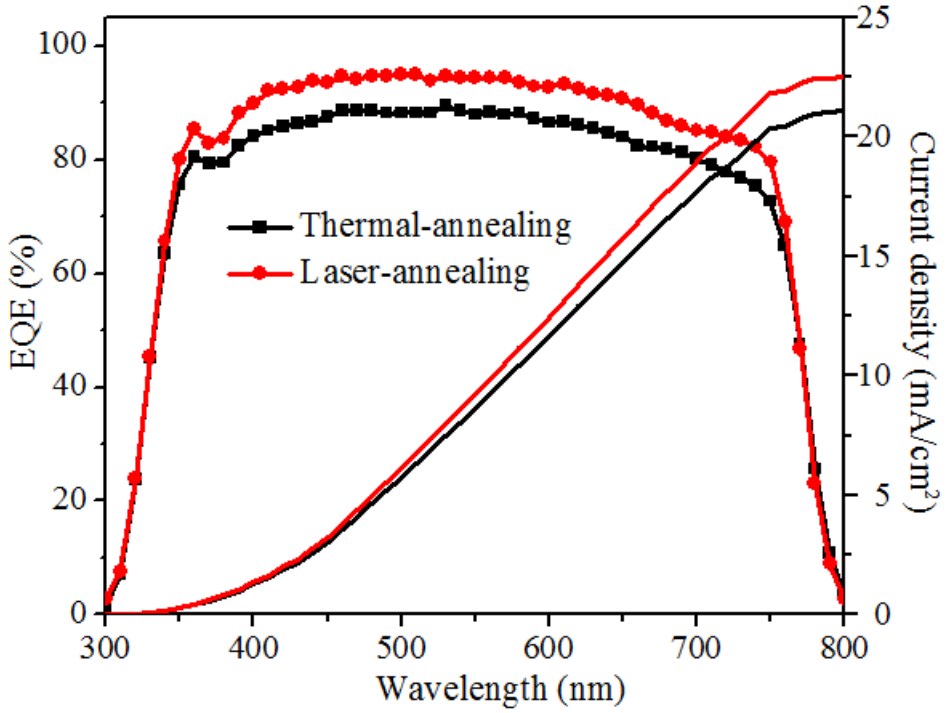

Figure 5.20 EQE spectra of the champion devices and the corresponding integrated current density over the wavelength range from 300 nm to 800 nm.

Furthermore, we also investigated the long-term stability of the PSCs fabricated by laser-annealing and thermal-annealing processes. Both the control and target devices with relatively high performance (10 devices for each condition, with a simple encapsulation) were kept in dry air with humidity ~ 30% for stability study. *J-V* curves of the devices were obtained every 10 days. The statistical data of the PCEs after 50 days' degradation was plotted in **Figure 5.21**. Apparently, the devices fabricated by laser-annealing were much more stable than the control devices. It was noteworthy that the target devices retained about 90% of its initial average PCE after 50-days' storage, while the reference devices remained only 78% of the original PCE. All the photovoltaic parameters of the devices decreased in some extent after 50-days' storage, however, the ~12% decrease in J_{sc} for the control devices contributed greatly to the degradation in performance. Furthermore, the deviation values (including PCE, J_{sc}, V_{oc} and FF) of the control devices increased greatly

during the degradation process while the target devices showed little change in deviation. The improved stability of the target devices should be mainly attributed to the improved crystallinity and larger grain size of the laser-annealed perovskite films.

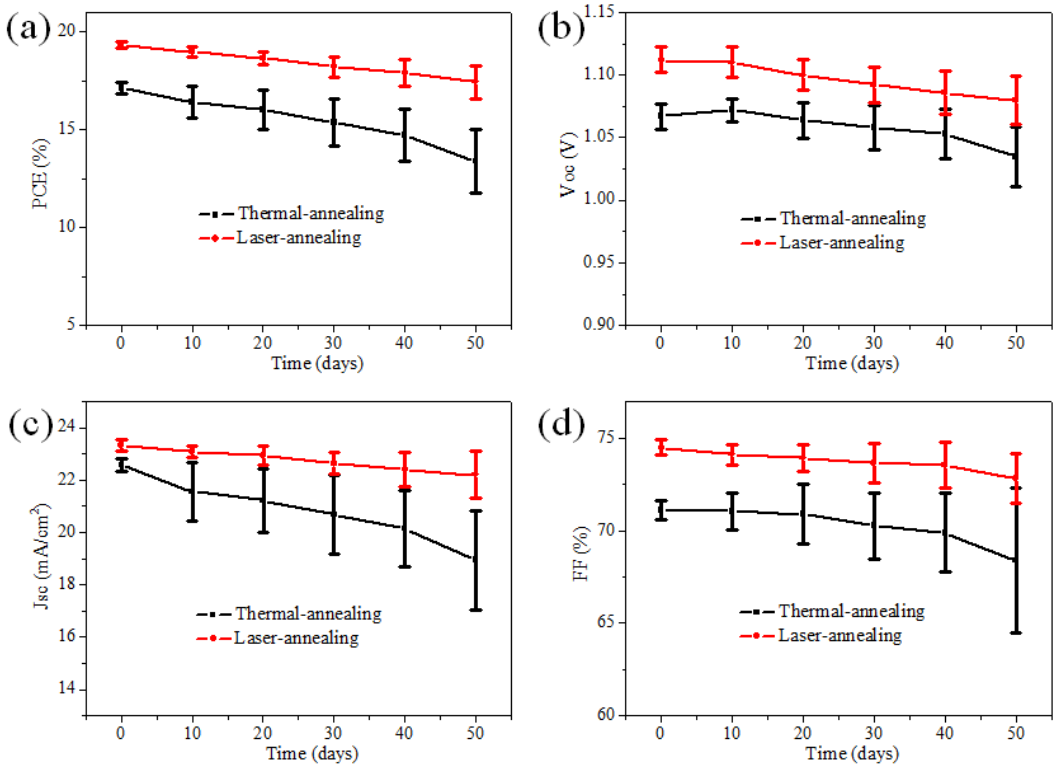

Figure 5.21 Evolution of photovoltaic parameters during stability test (average of 10 devices for each condition). All the devices were encapsulated and kept in air with humidity around 30%.

5.4 Summary

In summary, the utilization of laser-annealing as an alternative approach for the traditional thermal-annealing process was introduced. The crystallization of perovskite films can be well controlled by this facile laser-annealing approach. It was noteworthy that the laser scanning parameters, such as the laser wavelengths, laser scanning speeds and laser output power, were closely related with the

crystallization and morphology of the perovskite films. After systematical optimization, high-quality perovskite films with better crystallinity, preferred orientation, larger grain size and lower density of defects were successfully fabricated. As a result, we achieved a high open circuit voltage of 1.15 V and a champion efficiency of 20.08% with small *J*-*V* hysteresis and good stability. Thus, laser-annealing are promising as a novel technology for fabricating high-performance and large-area devices at room temperature, and it may also be suitable for the mass production of perovskite solar cells. It is also applicable to the fabrication of high-performance solar cells on curved surfaces, leading to some novel applications such as wearable electronics and photovoltaic vehicles. This preliminary work paves a way to prepare high-quality perovskite films with controllable morphology.

Chapter 6 Conclusions and Future Outlook

6.1 Conclusions

Semitransparent PSCs were fabricated by laminating stacked CVD graphene as top transparent electrodes on perovskite layers for the first time. The device performance was optimized by improving the conductivity of the graphene electrodes and the contact between the top graphene electrodes and the HTL (spiro-OMeTAD) on the perovskite films. The devices with double-layer graphene electrodes show the maximum PCEs of 12.02±0.32% and 11.65±0.35% from FTO and graphene side, respectively, which are relatively high compared with the reported semitransparent perovskite solar cells. This work indicates that CVD graphene is an ideal candidate for transparent electrodes of perovskite solar cells. Considering its excellent mechanical flexibility and convenient preparation, graphene electrodes are expected to be used in flexible perovskite solar cells by printing or roll to roll process, which may find applications to complement the rigid inorganic solar cells currently dominated in the market.

Then, we introduced the utilization of few-layer BP flakes with high carrier mobilities as an effective interfacial buffer layer at the perovskite/HTL interface in normal-structure PSCs. The ultrathin BP nano-flakes, prepared by liquid phase exfoliation and dispersed in anhydrous IPA, were deposited on top of perovskite films by dripping deposition. The photovoltaic performances were greatly enhanced after BP modification, due to the better band alignment, improved charge transport and reduced recombination loss at the perovskite/HTL interface. Besides, the device stability was also significantly improved due to the passivation effect of the BP flakes.

Our results pave the way towards the implementation of BP thin flakes as an effective perovskite interfacial layer to boost the device performance.

Finally, the utilization of laser-annealing as an alternative approach for the traditional thermal-annealing process was introduced. The crystallization of perovskite films can be well controlled by this facile laser-annealing approach. It was noteworthy that the laser scanning parameters, such as the laser wavelengths, laser scanning speeds and laser output power, were closely related with the crystallization and morphology of the perovskite films. After systematical optimization, high-quality perovskite films with better crystallinity, preferred orientation, larger grain size and lower density of defects were successfully fabricated. As a result, we achieved a high open circuit voltage of 1.15 V and a champion efficiency of 20.08% with small *J*-*V* hysteresis and good stability. Thus, laser-annealing are promising as a novel technology for fabricating high-performance and large-area devices at room temperature, and it may also be suitable for the mass production of perovskite solar cells. It is also applicable to the fabrication of high-performance solar cells on curved surfaces, leading to some novel applications such as wearable electronics and photovoltaic vehicles. This preliminary work paves a way to prepare high-quality perovskite films with controllable morphology.

6.2 Future Outlook

As discussed in the thesis, the CVD graphene films with high transparency and conductivity, were incorporated in PSCs as top electrodes by a simple lamination process. After optimization, the maximum PCE of around 12% was obtained from both FTO and graphene sides. The graphene electrodes are flexible and can be transferred on various conformal surfaces, being compatible with roll-to-roll process.

Therefore, graphene is an ideal transparent-electrode material for PV devices. In the next step, we will try to fabricate semi-transparent PSCs with all graphene electrodes to abandon the conventional ITO or FTO conductive electrodes completely. Since this laminated graphene electrodes tend to affect the long-term stability of the devices, it is necessary to further optimize this process. The PEDOT:PSS together with the D-sorbitol materials used as electronic glue are intrinsically unstable in air, thus alternatives of these materials are expected.

Secondly, we demonstrated solution exfoliated BP flakes can be used as an excerlent interfacial material at the perovskite/HTL interface and led to great enhancement of PCEs and device stability. This structure offers excellent band alignment, improves the hole transport property and reduces the recombination loss at the interface, thus the PCEs were greatly enhanced and are more reproducible. This study shows a universal method to use solution exfoliated 2D materials for interfacial engineering of PV devices. Thus, the introduction of new interfacial materials and the control of the distribution of the interfacial materials at the interface are urgently needed for the further enhancement of the PSCs. Not only the high mobility 2D materials, but also some suitable polymer, small molecules with high mobility can also be adopted as interfacial modification materials.

Also, we introduced the utilization of laser beam scanning on perovskite surfaces as an alternative approach to the traditional thermal annealing process. The laser scanning parameters were found to be closely related with the crystallization and morphology of the perovskite films. After systematical optimization, high-quality perovskite films with better crystallinity, larger grain size and lower density of defects were successfully fabricated. As a result, we achieved a high efficiency of over 20% with small hysteresis and good stability. This preliminary work introduced a novel approach to control the crystallization and morphology of

the perovskite films. In the next step, the effect of this laser-annealing process on the mixed perovskite will be studied. Flexible PSCs can be fabricated at room temperature by using laser-annealing technique. Besides, hopefully, large area PSCs (no less than 1 cm^2) with high efficiency can also be prepared with this technique.

Our work demonstrated that a lot of techniques can be applied to enhance the device performances, and there is still a large room for the improvement the efficiencies and stabilities of the PSCs. For the future work, we plan to combine more effective techniques together to improve the device performance more effectively. Considering that the approaches are convenient and cost effective, hopefully our research will pave the ways to realize high-efficiency PV devices for practice applications in the future.

References

1. Best Research-Cell Efficiencies: p. (NREL, 2018); https://www.nrel.gov/pv/assets/images/efficiency-chart.png.
2. Kojima, A., et al., *Organometal halid perovskites as visible-light sensitizers for photovoltaic cells.* J. Am. Chem. Soc., 2009. **131**: p. 6050-6051.
3. Kim, H.-S., et al., *Lead iodide perovskite sensitized all-solid-state submicron thin film mesoscopic solar cell with efficiency exceeding 9%.* Sci. Rep., 2012. **2**: p. 591.
4. Yang, W.S., et al., *Iodide management in formamidinium-lead-halide-based perovskite layers for efficient solar cells.* Science, 2017. **356**(6345): p. 1376-1379.
5. Kim, H.S., S.H. Im, and N.G. Park, *Organolead Halide Perovskite: New Horizons in Solar Cell Research.* Journal of Physical Chemistry C, 2014. **118**(11): p. 5615-5625.
6. Kawamura, Y., H. Mashiyama, and K. Hasebe, *Structural study on cubic-tetragonal transition of $CH_3NH_3PbI_3$.* Journal of the Physical Society of Japan, 2002. **71**(7): p. 1694-1697.
7. Feng, J. and B. Xiao, *Crystal Structures, Optical Properties, and Effective Mass Tensors of $CH_3NH_3PbX_3$ (X = I and Br) Phases Predicted from HSE06.* Journal of Physical Chemistry Letters, 2014. **5**(10): p. 1719-1720.
8. Green, M.A., A. Ho-Baillie, and H.J. Snaith, *The emergence of perovskite solar cells.* Nature Photonics, 2014. **8**: p. 506-514.
9. Yakunin, S., et al., *Detection of X-ray photons by solution-processed lead halide perovskites.* Nature Photonics, 2015. **9**(7): p. 444-449.
10. Yin, W.J., T.T. Shi, and Y.F. Yan, *Unique Properties of Halide Perovskites as Possible Origins of the Superior Solar Cell Performance.* Advanced Materials, 2014. **26**(27): p. 4653-4658.
11. De Wolf, S., et al., *Organometallic Halide Perovskites: Sharp Optical Absorption Edge and Its Relation to Photovoltaic Performance.* Journal of Physical Chemistry Letters, 2014. **5**(6): p. 1035-1039.
12. Miyata, A., et al., *Direct measurement of the exciton binding energy and effective masses for charge carriers in organic–inorganic tri-halide perovskites.* Nature Physics, 2015. **11**(7): p. 582-587.
13. Noh, J.H., et al., *Chemical management for colorful, efficient, and stable inorganic-organic hybrid nanostructured solar cells.* Nano. Lett., 2013. **13**(4): p. 1764-1769.
14. Stoumpos, C.C., C.D. Malliakas, and M.G. Kanatzidis, *Semiconducting Tin and Lead Iodide Perovskites with Organic Cations: Phase Transitions, High Mobilities, and Near-Infrared Photoluminescent Properties.* Inorganic

Chemistry, 2013. **52**(15): p. 9019-9038.

15. Pellet, N., et al., *Mixed-Organic-Cation Perovskite Photovoltaics for Enhanced Solar-Light Harvesting.* Angewandte Chemie-International Edition, 2014. **53**(12): p. 3151-3157.
16. Noel, N.K., et al., *Lead-free organic-inorganic tin halide perovskites for photovoltaic applications.* Energy & Environmental Science, 2014. **7**(9): p. 3061-3068.
17. Sadhanala, A., et al., *Preparation of Single-Phase Films of $CH_3NH_3Pb(I_{1-x},Br_x)_3$ with Sharp Optical Band Edges.* Journal of Physical Chemistry Letters, 2014. **5**(15): p. 2501-2505.
18. Giorgi, G., et al., *Small Photocarrier Effective Masses Featuring Ambipolar Transport in Methylammonium Lead Iodide Perovskite: A Density Functional Analysis.* Journal of Physical Chemistry Letters, 2013. **4**(24): p. 4213-4216.
19. Shi, D., et al., *Low trap-state density and long carrier diffusion in organolead trihalide perovskite single crystals.* Science, 2015. **347**(6221): p. 519-522.
20. Stranks, S.D., et al., *Electron-hole diffusion lengths exceeding 1 micrometer in an organometal trihalide perovskite absorber.* Science, 2013. **342**: p. 341-344.
21. Xing, G.C., et al., *Long-Range Balanced Electron- and Hole-Transport Lengths in Organic-Inorganic $CH_3NH_3PbI_3$.* Science, 2013. **342**(6156): p. 344-347.
22. Dong, Q.F., et al., *Electron-hole diffusion lengths > 175 um in solution-grown $CH_3NH_3PbI_3$ single crystals.* Science, 2015. **347**(6225): p. 967-970.
23. Leijtens, T., et al., *Electronic Properties of Meso-Superstructured and Planar Organometal Halide Perovskite Films: Charge Trapping, Photodoping, and Carrier Mobility.* Acs Nano, 2014. **8**(7): p. 7147-7155.
24. Wehrenfennig, C., et al., *High Charge Carrier Mobilities and Lifetimes in Organolead Trihalide Perovskites.* Advanced Materials, 2014. **26**(10): p. 1584-1589.
25. Valverde-Chavez, D.A., et al., *Intrinsic femtosecond charge generation dynamics in single crystal $CH_3NH_3PbI_3$.* Energy & Environmental Science, 2015. **8**(12): p. 3700-3707.
26. Eperon, G.E., et al., *Formamidinium lead trihalide: a broadly tunable perovskite for efficient planar heterojunction solar cells.* Energy Environ. Sci., 2014. **7**(3): p. 982-988.
27. Jeon, N.J., et al., *Compositional engineering of perovskite materials for high-performance solar cells.* Nature, 2015. **517**(7535): p. 476-480.
28. Amat, A., et al., *Cation-induced band-gap tuning in organohalide perovskites: interplay of spin-orbit coupling and octahedra tilting.* Nano. Lett., 2014. **14**(6): p. 3608-3616.
29. Geng, W., et al., *First-Principles Study of Lead Iodide Perovskite Tetragonal and Orthorhombic Phases for Photovoltaics.* Journal of Physical Chemistry

C, 2014. **118**(34): p. 19565-19571.

30. Saliba, M., et al., *Cesium-containing triple cation perovskite solar cells: improved stability, reproducibility and high efficiency.* Energy Environ. Sci., 2016. **9**: p. 1989-1997.
31. Jacobsson, T.J., et al., *Exploration of the compositional space for mixed lead halogen perovskites for high efficiency solar cells.* Energy & Environmental Science, 2016. **9**(5): p. 1706-1724.
32. Hao, F., et al., *Anomalous Band Gap Behavior in Mixed Sn and Pb Perovskites Enables Broadening of Absorption Spectrum in Solar Cells.* Journal of the American Chemical Society, 2014. **136**(22): p. 8094-8099.
33. Saidaminov, M.I., et al., *High-quality bulk hybrid perovskite single crystals within minutes by inverse temperature crystallization.* Nature Communications, 2015. **6**.
34. Liu, Y.C., et al., *Two-Inch-Sized Perovskite $CH_3NH_3PbX_3$ (X = Cl, Br, I) Crystals: Growth and Characterization.* Advanced Materials, 2015. **27**(35): p. 5176-5183.
35. Dang, Y.Y., et al., *Formation of Hybrid Perovskite Tin Iodide Single Crystals by Top-Seeded Solution Growth.* Angewandte Chemie-International Edition, 2016. **55**(10): p. 3447-3450.
36. Im, J.H., et al., *6.5% efficient perovskite quantum-dot-sensitized solar cell.* Nanoscale, 2011. **3**(10): p. 4088-4093.
37. Kojima, A., et al., *Highly Luminescent Lead Bromide Perovskite Nanoparticles Synthesized with Porous Alumina Media.* Chemistry Letters, 2012. **41**(4): p. 397-399.
38. Fu, Y.P., et al., *Solution Growth of Single Crystal Methylammonium Lead Halide Perovskite Nanostructures for Optoelectronic and Photovoltaic Applications.* Journal of the American Chemical Society, 2015. **137**(17): p. 5810-5818.
39. Schmidt, L.C., et al., *Nontemplate Synthesis of $CH_3NH_3PbBr_3$ Perovskite Nanoparticles.* Journal of the American Chemical Society, 2014. **136**(3): p. 850-853.
40. Protesescu, L., et al., *Nanocrystals of Cesium Lead Halide Perovskites ($CsPbX_3$, X = Cl, Br, and I): Novel Optoelectronic Materials Showing Bright Emission with Wide Color Gamut.* Nano Letters, 2015. **15**(6): p. 3692-3696.
41. Liu, J.Y., et al., *Two-Dimensional $CH_3NH_3PbI_3$ Perovskite: Synthesis and Optoelectronic Application.* Acs Nano, 2016. **10**(3): p. 3536-3542.
42. Dou, L.T., et al., *Atomically thin two-dimensional organic-inorganic hybrid perovskites.* Science, 2015. **349**(6255): p. 1518-1521.
43. Im, J.H., H.S. Kim, and N.G. Park, *Morphology-photovoltaic property correlation in perovskite solar cells: One-step versus two-step deposition of $CH_3NH_3PbI_3$.* Apl Materials, 2014. **2**(8).
44. Liu, M., M.B. Johnston, and H.J. Snaith, *Efficient planar heterojunction perovskite solar cells by vapour deposition.* Nature, 2013. **501**(7467): p.

395-398.

45. Lee, M.M., et al., *Efficient hybrid solar cells based on meso-superstructured organometal halide perovskites.* Science, 2012. **338**: p. 643-647.
46. Zhou, H., et al., *Interface engineering of highly efficient perovskite solar cells.* Science, 2014. **345**(6196): p. 542-546.
47. You, J., et al., *Moisture assisted perovskite film growth for high performance solar cells.* Appl. Phys. Lett., 2014. **105**(18): p. 183902.
48. Heo, J.H., et al., *Hysteresis-less inverted $CH_3NH_3PbI_3$ planar perovskite hybrid solar cells with 18.1% power conversion efficiency.* Energy Environ. Sci., 2015. **8**: p. 1602-1608.
49. Zhao, Y.X. and K. Zhu, *Efficient Planar Perovskite Solar Cells Based on 1.8 eV Band Gap $CH_3NH_3PbI_2Br$ Nanosheets via Thermal Decomposition.* Journal of the American Chemical Society, 2014. **136**(35): p. 12241-12244.
50. Xiao, M.D., et al., *A Fast Deposition-Crystallization Procedure for Highly Efficient Lead Iodide Perovskite Thin-Film Solar Cells.* Angewandte Chemie-International Edition, 2014. **53**(37): p. 9898-9903.
51. Jeon, N.J., et al., *Solvent engineering for high-performance inorganic-organic hybrid perovskite solar cells.* Nature Materials, 2014. **13**(9): p. 897-903.
52. Saliba, M., et al., *A molecularly engineered hole-transporting material for efficient perovskite solar cells.* Nat. Energy, 2016. **1**: p. 1-7.
53. Burschka, J., et al., *Sequential deposition as a route to high-performance perovskite-sensitized solar cells.* Nature, 2013. **499**(7458): p. 316-319.
54. Xiao, Z.G., et al., *Efficient, high yield perovskite photovoltaic devices grown by interdiffusion of solution-processed precursor stacking layers.* Energy & Environmental Science, 2014. **7**(8): p. 2619-2623.
55. Yang, W.S., et al., *High-performance photovoltaic perovskite layers fabricated through intramolecular exchange.* Science, 2015. **348**: p. 1234-1237.
56. Bi, C., et al., *Non-wetting surface-driven high-aspect-ratio crystalline grain growth for efficient hybrid perovskite solar cells.* Nature Communications, 2015. **6**.
57. Wu, C.G., et al., *High efficiency stable inverted perovskite solar cells without current hysteresis.* Energy & Environmental Science, 2015. **8**(9): p. 2725-2733.
58. Dong, Q.F., et al., *Abnormal crystal growth in $CH_3NH_3PbI_{3-x}Cl_x$ using a multi-cycle solution coating process.* Energy & Environmental Science, 2015. **8**(8): p. 2464-2470.
59. Chen, Y.H., T. Chen, and L.M. Dai, *Layer-by-Layer Growth of $CH_3NH_3PbI_{3-x}Cl_x$ for Highly Efficient Planar Heterojunction Perovskite Solar Cells.* Advanced Materials, 2015. **27**(6): p. 1053-1059.
60. Heo, J.H., et al., *Efficient inorganic–organic hybrid heterojunction solar cells containing perovskite compound and polymeric hole conductors.* Nat.

Photonics, 2013. **7**: p. 486-491.

61. Choi, J.J., et al., *Structure of Methylammonium Lead Iodide Within Mesoporous Titanium Dioxide: Active Material in High-Performance Perovskite Solar Cells.* Nano Letters, 2014. **14**(1): p. 127-133.
62. Bi, D., et al., *Efficient luminescent solar cells based on tailored mixed-cation perovskites.* Sci. Adv., 2016. **2**: p. e1501170.
63. Ke, W.J., et al., *Employing Lead Thiocyanate Additive to Reduce the Hysteresis and Boost the Fill Factor of Planar Perovskite Solar Cells.* Advanced Materials, 2016. **28**(26): p. 5214.
64. Seo, J.-Y., et al., *Ionic Liquid Control Crystal Growth to Enhance Planar Perovskite Solar Cells Efficiency.* Advanced Energy Materials, 2016: p. 1600767.
65. Nie, W.Y., et al., *High-efficiency solution-processed perovskite solar cells with millimeter-scale grains.* Science, 2015. **347**(6221): p. 522-525.
66. Wang, Q., et al., *Thin Insulating Tunneling Contacts for Efficient and Water-Resistant Perovskite Solar Cells.* Adv Mater, 2016. **28**(31): p. 6734-9.
67. Leijtens, T., et al., *Overcoming ultraviolet light instability of sensitized TiO_2 with meso-superstructured organometal tri-halide perovskite solar cells.* Nat. Commun., 2013. **4**: p. 2885.
68. Kwon, Y.S., et al., *A diketopyrrolopyrrole-containing hole transporting conjugated polymer for use in efficient stable organic–inorganic hybrid solar cells based on a perovskite.* Energy Environ. Sci., 2014. **7**(4): p. 1454-1460.
69. Mei, A., et al., *A hole-conductor-free, fully printable mesoscopic perovskite solar cell with high stability.* Science, 2014. **345**: p. 295-298.
70. Chen, W., et al., *Efficient and stable large-area perovskite solar cells with inorganic charge extraction layers.* Science, 2015. **350**: p. 944-948.
71. You, J., et al., *Improved air stability of perovskite solar cells via solution-processed metal oxide transport layers.* Nat. Nanotechnol., 2016. **11**: p. 75-81.
72. Lee, J.W., et al., *Formamidinium and Cesium Hybridization for Photo- and Moisture-Stable Perovskite Solar Cell.* Advanced Energy Materials, 2015. **5**(20).
73. Snaith, H.J., et al., *Anomalous Hysteresis in Perovskite Solar Cells.* Journal of Physical Chemistry Letters, 2014. **5**(9): p. 1511-1515.
74. Tress, W., et al., *Understanding the rate-dependent J-V hysteresis, slow time component, and aging in $CH_3NH_3PbI_3$ perovskite solar cells: the role of a compensated electric field.* Energy & Environmental Science, 2015. **8**(3): p. 995-1004.
75. Wei, J., et al., *Hysteresis Analysis Based on the Ferroelectric Effect in Hybrid Perovskite Solar Cells.* Journal of Physical Chemistry Letters, 2014. **5**(21): p. 3937-3945.
76. Meloni, S., et al., *Ionic polarization-induced current-voltage hysteresis in $CH_3NH_3PbX_3$ perovskite solar cells.* Nature Communications, 2016. **7**.

77. van Reenen, S., M. Kemerink, and H.J. Snaith, *Modeling Anomalous Hysteresis in Perovskite Solar Cells.* Journal of Physical Chemistry Letters, 2015. **6**(19): p. 3808-3814.
78. Chen, H.W., et al., *Emergence of Hysteresis and Transient Ferroelectric Response in Organo-Lead Halide Perovskite Solar Cells (vol 6, pg 164, 2015).* Journal of Physical Chemistry Letters, 2015. **6**(6): p. 935-935.
79. Shao, Y.H., et al., *Origin and elimination of photocurrent hysteresis by fullerene passivation in $CH_3NH_3PbI_3$ planar heterojunction solar cells.* Nature Communications, 2014. **5**.
80. Fan, Z., et al., *Ferroelectricity of $CH_3NH_3PbI_3$ Perovskite.* Journal of Physical Chemistry Letters, 2015. **6**(7): p. 1155-1161.
81. Li, C., et al., *Iodine Migration and its Effect on Hysteresis in Perovskite Solar Cells.* Advanced Materials, 2016. **28**(12): p. 2446-2454.
82. Liao, W., et al., *Lead-Free Inverted Planar Formamidinium Tin Triiodide Perovskite Solar Cells Achieving Power Conversion Efficiencies up to 6.22.* Adv Mater, 2016. **28**(42): p. 9333-9340.
83. Hao, F., et al., *Lead-free solid-state organic-inorganic halide perovskite solar cells.* Nature Photonics, 2014. **8**(6): p. 489-494.
84. Jung, H.S. and N.G. Park, *Perovskite Solar Cells: From Materials to Devices.* Small, 2015. **11**(1): p. 10-25.
85. Eperon, G.E., et al., *Neutral Color Semitransparent Microstructured Perovskite Solar Cells.* Acs Nano, 2014. **8**(1): p. 591-598.
86. Eperon, G.E., et al., *Efficient, Semitransparent Neutral-Colored Solar Cells Based on Microstructured Formamidinium Lead Trihalide Perovskite.* Journal of Physical Chemistry Letters, 2015. **6**(1): p. 129-138.
87. Roldan-Carmona, C., et al., *High efficiency single-junction semitransparent perovskite solar cells.* Energy & Environmental Science, 2014. **7**(9): p. 2968-2973.
88. Guo, F., et al., *High-performance semitransparent perovskite solar cells with solution-processed silver nanowires as top electrodes.* Nanoscale, 2015. **7**(5): p. 1642-1649.
89. Bryant, D., et al., *A Transparent Conductive Adhesive Laminate Electrode for High-Efficiency Organic-Inorganic Lead Halide Perovskite Solar Cells.* Advanced Materials, 2014. **26**(44): p. 7499-7504.
90. Li, Z., et al., *Laminated Carbon Nanotube Networks for Metal Electrode-Free Efficient Perovskite Solar Cells.* Acs Nano, 2014. **8**(7): p. 6797-6804.
91. Bailie, C.D., et al., *Semi-transparent perovskite solar cells for tandems with silicon and CIGS.* Energy & Environmental Science, 2015. **8**(3): p. 956-963.
92. Hecht, D.S., L.B. Hu, and G. Irvin, *Emerging Transparent Electrodes Based on Thin Films of Carbon Nanotubes, Graphene, and Metallic Nanostructures.* Advanced Materials, 2011. **23**(13): p. 1482-1513.
93. Liu, Z.K., J.H. Li, and F. Yan, *Package-Free Flexible Organic Solar Cells*

with Graphene top Electrodes. Advanced Materials, 2013. **25**(31): p. 4296-4301.

94. Li, J.H., et al., *Photosensitive Graphene Transistors.* Advanced Materials, 2014. **26**(31): p. 5239-5273.
95. Liu, Z.K., et al., *The Application of Highly Doped Single-Layer Graphene as the Top Electrodes of Semitransparent Organic Solar Cells.* Acs Nano, 2012. **6**(1): p. 810-818.
96. Hellstrom, S.L., et al., *Strong and Stable Doping of Carbon Nanotubes and Graphene by MoO_x for Transparent Electrodes.* Nano Letters, 2012. **12**(7): p. 3574-3580.
97. Chen, T., et al., *Intertwined Aligned Carbon Nanotube Fiber Based Dye-Sensitized Solar Cells.* Nano Letters, 2012. **12**(5): p. 2568-2572.
98. Czolk, J., et al., *Inverted Semi-transparent Polymer Solar Cells with Transparency Color Rendering Indices approaching 100.* Advanced Energy Materials, 2013. **3**(3): p. 386-390.
99. Alemu, D., et al., *Highly conductive PEDOT:PSS electrode by simple film treatment with methanol for ITO-free polymer solar cells.* Energy & Environmental Science, 2012. **5**(11): p. 9662-9671.
100. Yu, Z.B., et al., *Silver Nanowire-Polymer Composite Electrodes for Efficient Polymer Solar Cells.* Advanced Materials, 2011. **23**(38): p. 4453-4457.
101. Chen, C.C., et al., *Visibly Transparent Polymer Solar Cells Produced by Solution Processing.* Acs Nano, 2012. **6**(8): p. 7185-7190.
102. Geim, A.K. and K.S. Novoselov, *The rise of graphene.* Nature Materials, 2007. **6**(3): p. 183-191.
103. Wang, J.T.-W., et al., *Low-temperature processed electron collection layers of graphene/TiO_2 nanocomposites in thin film perovskite solar cells.* Nano. Lett., 2014. **14**(2): p. 724-730.
104. Zhu, Z.L., et al., *Efficiency Enhancement of Perovskite Solar Cells through Fast Electron Extraction: The Role of Graphene Quantum Dots.* Journal of the American Chemical Society, 2014. **136**(10): p. 3760-3763.
105. Wang, Y., et al., *Interface Engineering of Layer-by-Layer Stacked Graphene Anodes for High-Performance Organic Solar Cells.* Advanced Materials, 2011. **23**(13): p. 1514-1518.
106. Sun, Z.H., et al., *Infrared Photodetectors Based on CVD-Grown Graphene and PbS Quantum Dots with Ultrahigh Responsivity.* Advanced Materials, 2012. **24**(43): p. 5878-5883.
107. Ouyang, H.Y. and Y. Yang, *Conducting polymer as transparent electric glue.* Advanced Materials, 2006. **18**(16): p. 2141-2144.
108. Tai, Q.D., et al., *In Situ Prepared Transparent Polyaniline Electrode and Its Application in Bifacial Dye-Sensitized Solar Cells.* Acs Nano, 2011. **5**(5): p. 3795-3799.
109. Unger, E.L., et al., *Hysteresis and transient behavior in current–voltage measurements of hybrid-perovskite absorber solar cells.* Energy Environ. Sci.,

2014. **7**: p. 3690–3698.

110. Wen, X.R., et al., *Interfacial engineering with amino-functionalized graphene for efficient perovskite solar cells.* Journal of Materials Chemistry A, 2016. **4**(35): p. 13482-13487.
111. Peng, W.N., et al., *Influence of growth temperature on bulk and surface defects in hybrid lead halide perovskite films.* Nanoscale, 2016. **8**(3): p. 1627-1634.
112. Abate, A., et al., *Supramolecular Halogen Bond Passivation of Organic-Inorganic Halide Perovskite Solar Cells.* Nano Letters, 2014. **14**(6): p. 3247-3254.
113. Noel, N.K., et al., *Enhanced Photoluminescence and Solar Cell Performance via Lewis Base Passivation of Organic Inorganic Lead Halide Perovskites.* Acs Nano, 2014. **8**(10): p. 9815-9821.
114. Kim, H., K.G. Lim, and T.W. Lee, *Planar heterojunction organometal halide perovskite solar cells: roles of interfacial layers.* Energy & Environmental Science, 2016. **9**(1): p. 12-30.
115. Chueh, C.C., C.Z. Li, and A.K.Y. Jen, *Recent progress and perspective in solution-processed Interfacial materials for efficient and stable polymer and organometal perovskite solar cells.* Energy & Environmental Science, 2015. **8**(4): p. 1160-1189.
116. Li, Y.W., et al., *Multifunctional Fullerene Derivative for Interface Engineering in Perovskite Solar Cells.* Journal of the American Chemical Society, 2015. **137**(49): p. 15540-15547.
117. Dong, Y., et al., *Highly Efficient Planar Perovskite Solar Cells Via Interfacial Modification with Fullerene Derivatives.* Small, 2016. **12**(8): p. 1098-1104.
118. Wu, Y., et al., *Perovskite solar cells with 18.21% efficiency and area over 1 cm2*

fabricated by heterojunction engineering. Nature Energy, 2016. **1**(11): p. 16148.

119. Song, D.D., et al., *Dual function interfacial layer for highly efficient and stable lead halide perovskite solar cells.* Journal of Materials Chemistry A, 2016. **4**(16): p. 6091-6097.
120. Wang, F., et al., *Phenylalkylamine Passivation of Organolead Halide Perovskites Enabling High-Efficiency and Air-Stable Photovoltaic Cells.* Advanced Materials, 2016. **28**(45): p. 9986-9992.
121. Feng, S.L., et al., *High-Performance Perovskite Solar Cells Engineered by an Ammonia Modified Graphene Oxide Interfacial Layer.* Acs Applied Materials & Interfaces, 2016. **8**(23): p. 14503-14512.
122. Agresti, A., et al., *Graphene-Perovskite Solar Cells Exceed 18% Efficiency: A Stability Study.* Chemsuschem, 2016. **9**(18): p. 2609-2619.
123. Capasso, A., et al., *Few-Layer MoS_2 Flakes as Active Buffer Layer for Stable Perovskite Solar Cells.* Advanced Energy Materials, 2016. **6**(16).
124. Liu, H., et al., *Semiconducting black phosphorus: synthesis, transport properties and electronic applications.* Chemical Society Reviews, 2015.

44(9): p. 2732-2743.

125. Long, G., et al., *Achieving Ultrahigh Carrier Mobility in Two-Dimensional Hole Gas of Black Phosphorus.* Nano Letters, 2016. **16**(12): p. 7768-7773.
126. Li, L.K., et al., *Black phosphorus field-effect transistors.* Nature Nanotechnology, 2014. **9**(5): p. 372-377.
127. Hao, C.X., et al., *Flexible All-Solid-State Supercapacitors based on Liquid-Exfoliated Black-Phosphorus Nanoflakes.* Advanced Materials, 2016. **28**(16): p. 3194-3201.
128. Chen, L., et al., *Scalable Clean Exfoliation of High-Quality Few-Layer Black Phosphorus for a Flexible Lithium Ion Battery.* Advanced Materials, 2016. **28**(3): p. 510-517.
129. Youngblood, N., et al., *Waveguide-integrated black phosphorus photodetector with high responsivity and low dark current.* Nature Photonics, 2015. **9**(4): p. 247-252.
130. Huang, M.Q., et al., *Broadband Black-Phosphorus Photodetectors with High Responsivity.* Advanced Materials, 2016. **28**(18): p. 3481-3485.
131. Abbas, A.N., et al., *Black Phosphorus Gas Sensors.* Acs Nano, 2015. **9**(5): p. 5618-5624.
132. Chen, W., et al., *Black Phosphorus Quantum Dots for Hole Extraction of Typical Planar Hybrid Perovskite Solar Cells.* Journal of Physical Chemistry Letters, 2017. **8**(3): p. 591-598.
133. Guo, Z.N., et al., *From Black Phosphorus to Phosphorene: Basic Solvent Exfoliation, Evolution of Raman Scattering, and Applications to Ultrafast Photonics.* Advanced Functional Materials, 2015. **25**(45): p. 6996-7002.
134. Hanlon, D., et al., *Liquid exfoliation of solvent-stabilized few-layer black phosphorus for applications beyond electronics.* Nature Communications, 2015. **6**.
135. Liu, Z.K., et al., *Ultrathin and flexible perovskite solar cells with graphene transparent electrodes.* Nano Energy, 2016. **28**: p. 151-157.
136. Liu, Y.Y., et al., *Two-Dimensional Mono-Elemental Semiconductor with Electronically Inactive Defects: The Case of Phosphorus.* Nano Letters, 2014. **14**(12): p. 6782-6786.
137. Tai, Q.D., et al., *Efficient and stable perovskite solar cells prepared in ambient air irrespective of the humidity.* Nature Communications, 2016. **7**.
138. You, P., et al., *Efficient Semitransparent Perovskite Solar Cells with Graphene Electrodes.* Advanced Materials, 2015. **27**(24): p. 3632-3638.
139. Sha, W.E.I., et al., *The efficiency limit of $CH_3NH_3PbI_3$ perovskite solar cells.* Applied Physics Letters, 2015. **106**(22).
140. Xiao, Z.G., et al., *Solvent Annealing of Perovskite-Induced Crystal Growth for Photovoltaic-Device Efficiency Enhancement.* Advanced Materials, 2014. **26**(37): p. 6503-6509.
141. Zhang, W., et al., *Enhanced optoelectronic quality of perovskite thin films with hypophosphorous acid for planar heterojunction solar cells.* Nature

Communications, 2015. **6**.

142. Li, X., et al., *A vacuum flash-assisted solution process for high-efficiency large-area perovskite solar cells.* Science, 2016. **353**(6294): p. 58-62.
143. Xianyu, W.X., et al., *Excimer laser annealing of $PbZr_{0.4}Ti_{0.6}O_3$ thin film at low temperature.* Ieice Transactions on Electronics, 2006. **E89c**(10): p. 1460-1464.
144. Xianyu, W.X., et al., *Excimer (XeCl) laser annealing of $PbZr_{0.4}Ti_{0.6}O_3$ thin film at low temperature for TFT FeRAM application.* Materials and Processes for Nonvolatile Memories, 2005. **830**: p. 159-164.
145. Hosokawa, A., et al., *Low temperature polysilicon chemical vapor deposition system for thin film transistor liquid crystal diode.* Journal of Vacuum Science & Technology B, 2001. **19**(5): p. 1981-1984.
146. Murakami, Y., J.W. Li, and T. Shimoda, *Highly conductive ruthenium oxide thin films by a low-temperature solution process and green laser annealing.* Materials Letters, 2015. **152**: p. 121-124.
147. Ooms, M.D., Y. Jeyaram, and D. Sinton, *Disposable Plasmonics: Rapid and Inexpensive Large Area Patterning of Plasmonic Structures with CO_2 Laser Annealing.* Langmuir, 2015. **31**(18): p. 5252-5258.
148. Pan, H., et al., *Fiber laser annealing of indium-tin-oxide nanoparticles for large area transparent conductive layers and optical film characterization.* Applied Physics a-Materials Science & Processing, 2011. **104**(1): p. 29-38.
149. Eggleston, B., S. Varlamov, and M. Green, *Large-Area Diode Laser Defect Annealing of Polycrystalline Silicon Solar Cells.* Ieee Transactions on Electron Devices, 2012. **59**(10): p. 2838-2841.
150. Ohse, R.W., *Laser Application in High-Temperature Materials.* Pure and Applied Chemistry, 1988. **60**(3): p. 309-322.
151. Li, N., et al., *Towards large-scale production of solution-processed organic tandem modules based on ternary composites: Design of the intermediate layer, device optimization and laser based module processing.* Solar Energy Materials and Solar Cells, 2014. **120**: p. 701-708.
152. Yung, W.K.C., et al., *Eye-friendly reduced graphene oxide circuits with nonlinear optical transparency on flexible poly(ethylene terephthalate) substrates.* Journal of Materials Chemistry C, 2015. **3**(43): p. 11294-11299.
153. Jeon, J.H., et al., *New excimer laser crystallization in the lattice shape to improve the uniformity of electrical characteristics of poly-Si TFT.* Flat-Panel Display Materials-1998, 1998. **508**: p. 103-108.
154. Staudt, W., S. Borneis, and K.D. Pippert, *TFT annealing with excimer laser. Technology and market outlook.* Physica Status Solidi a-Applied Research, 1998. **166**(2): p. 743-750.
155. Crowder, M.A., et al., *Parametric investigation of SLS-processed poly-silicon thin films for TFT applications.* Thin Solid Films, 2003. **427**(1-2): p. 101-107.
156. Voutsas, A.T., A. Limanov, and J.S. Im, *Effect of process parameters on the*

structural characteristics of laterally grown, laser-annealed polycrystalline silicon films. Journal of Applied Physics, 2003. **94**(12): p. 7445-7452.

157. Lee, S., et al., *Application of Ge Quantum Wells Fabricated by Laser Annealing As Energy Selective Contacts for Hot-carrier Solar Cells.* 2012 38th Ieee Photovoltaic Specialists Conference (Pvsc), 2012: p. 801-805.
158. Pawar, S.M., et al., *Fabrication of Cu2ZnSnS4 Thin Film Solar Cell Using Single Step Electrodeposition Method.* Japanese Journal of Applied Physics, 2012. **51**(10).
159. Meadows, H.J., et al., *Single Second Laser Annealed $CuInSe_2$ Semiconductors from Electrodeposited Precursors as Absorber Layers for Solar Cells.* Journal of Physical Chemistry C, 2014. **118**(3): p. 1451-1460.
160. Varlamov, S., et al., *Diode laser processed crystalline silicon thin-film solar cells.* Laser-Based Micro- and Nanopackaging and Assembly Vii, 2013. **8608**.
161. Chang, C.M., et al., *Local electrical characterization of laser-recorded phase-change marks on amorphous $Ge_2Sb_2Te_5$ thin films.* Optics Express, 2011. **19**(10): p. 9492-9504.
162. Chu, C.H., et al., *Fabrication of phase-change Ge2Sb2Te5 nano-rings.* Optics Express, 2011. **19**(13): p. 12652-12657.
163. Jeon, T., et al., *Laser Crystallization of Organic-Inorganic Hybrid Perovskite Solar Cells.* Acs Nano, 2016. **10**(8): p. 7907-7914.
164. Bi, D.Q., et al., *Polymer-templated nucleation and crystal growth of perovskite films for solar cells with efficiency greater than 21%.* Nature Energy, 2016. **1**.
165. deQuilettes, D.W., et al., *Impact of microstructure on local carrier lifetime in perovskite solar cells.* Science, 2015. **348**(6235): p. 683-686.
166. Son, D.Y., et al., *Self-formed grain boundary healing layer for highly efficient $CH_3NH_3PbI_3$ perovskite solar cells.* Nature Energy, 2016. **1**.